Analysis of the GPCR-induced RhoA signaling in healthy and diseased adult cardiomyocytes

Doctoral Thesis

In partial fulfillment of the requirements for the degree
"Doctor rerum naturalium (Dr. rer. nat.)"
in the Molecular Medicine Study Program
at the Georg-August-University Göttingen

submitted by

Sebastian Pasch

born in Leipzig, Germany

Göttingen, 2018

Members of the Thesis Committee

Supervisor

Prof. Dr. Susanne Lutz

Institute of Pharmacology and Toxicology

University Medical Center Göttingen

Georg-August-University Göttingen

Second member of the thesis committee

Prof. Dr. Ralf Dressel

Institute for Cellular and Molecular Immunology

University Medical Center Göttingen

Georg-August-University Göttingen

Third member of the thesis committee

Prof. Dr. Dörthe M. Katschinski

Institute of Cardiovascular Physiology

University Medical Center Göttingen

Georg-August-University Göttingen

Date of Disputation: 24th July 2018

AFFIDAVIT

Here I declare that my doctoral thesis entitled "**Analysis of the GPCR-induced RhoA signaling in healthy and diseased adult cardiomyocytes**" has been written independently with no other sources and aids than quoted.

Sebastian Pasch

Göttingen, May 2018

Table of Contents

Table of Contents

Acknowledgment

Acknowledgment

My friends and running colleagues A big thank you to Henna, Andrea, Bene, Flo, Schmitzens, Julia, Ruwan, Jonas, Miriam, Daniel, Kathi and all the others who taught me that there is a life besides the lab and who make this life much funnier. Thanks to all the crazy running guys who helped me to clear my head after stressful days.

My family Mutti, Jörg, thank you so much for always being there and for your support through good and hard times. It is the best feeling to know that you will be so proud when you read this thesis. There is only one person who might even be prouder. Gilbert, it is great to have a brother like you!

Petra, Reinhart, I am so happy that we are one big family now. Thank you for all the time and support, which made it possible for me to finish this thesis.

Mika, Emil, Eva, the last year was full of ups and downs, full of hopes and fears and finally we became a family. You are healthy, you are there, and I could not be more grateful. Thank you for being there, for loving me and for giving me so much strength. Thank you for every "lalala eieiei mmmmhhhhh" in the morning and for giving me the most wonderful smiles every day.

Abstract

Background The aim of the presented thesis was to analyze the activation of the monomeric G protein RhoA in adult cardiomyocytes and further to unravel the role of the guanine nucleotide exchange factor p63RhoGEF in this context. Previous data demonstrated that RhoA is activated in neonatal cardiomyocytes by GPCR ligands like endothelin-1 (ET-1), phenylephrine (PE) and angiotensin II (AngII). So far, a contribution of the $G_{q/11}$ protein-regulated p63RhoGEF was demonstrated in the ET-1-mediated RhoA activation in neonatal cardiomyocytes. Moreover, RhoA was described to be permanently activated in pressure-overloaded hearts and p63RhoGEF to be higher expressed in the same system. This led to the hypothesis that p63RhoGEF is involved in the GPCR-dependent RhoA regulation in adult cardiomyocytes.

Methods The obtained data result from combined analysis of isolated wildtype (WT), healthy (sham) and diseased (transverse aortic constriction, TAC) adult mouse cardiomyocytes (AMCM) as well as of cholesterol-depleted AMCM (MβCD-AMCM) and of heterozygous (HET) and homozygous (KO) p63RhoGEF-knockout AMCM. p63RhoGEF-constructs were adenovirally overexpressed in WT-AMCM. The activity of RhoA was studied with the help of an antibody which specifically recognizes the conformation of active RhoA (RhoA-GTP) by immunofluorescence stainings and confocal imaging. Changes in RhoA activity were exemplarily confirmed by a biochemical binding assay. Protein distribution in AMCM was also analyzed by immunofluorescence stainings and confocal imaging, and protein expression was detected by immunoblot analysis. Quantitative analyses of protein co-localization and distribution were performed with ImageJ.

Results Independent of the investigated condition, active RhoA was predominately localized at the sarcolemma in AMCM. Application of ET-1, PE and AngII to WT- or sham-AMCM resulted in an increased level of active RhoA and a redistribution towards the costameric regions of the sarcolemma. Neither in TAC-, MβCD-, HET- nor in KO-AMCM an activation occurred in response to the GPCR ligands. In contrast, in all four types of AMCM, ET-1 and PE reduced the RhoA activity compared to control. Interestingly, in TAC-, MβCD- and KO-AMCM the basal RhoA activity was increased indicating that the tight regulation of RhoA in its signal context is disturbed when i) the sarcolemma is disorganized as after TAC, ii) cholesterol is depleted after MβCD treatment, or iii) p63RhoGEF is fully absent. This prompted the idea that p63RhoGEF is not only involved in the activation of RhoA in response to GPCRs, but also important for the membrane homeostasis in AMCM. By overexpression of p63RhoGEF, we could confirm its formerly described localization at the sarcolemma and found in addition a perinuclear

distribution. This led amongst others to an increase in the number of cis-Golgi apparatus particles similar as observed in TAC-AMCM. In contrast, the loss of p63RhoGEF reduced particle number arguing that p63RhoGEF is involved in Golgi apparatus regulation. Interestingly, p63RhoGEF also affected the size of the AMCM nuclei. Overexpression of a dominant negative p63RhoGEF construct (p63ΔN) reduced the area of the nuclei, comparable as seen in isolated AMCM and intact myocardium after p63RhoGEF depletion. Opposing to this, in TAC-AMCM the mean nucleus area was increased. This was in accordance with the observed changes in cell size. Although there were differences in the type and height of the affected parameters, p63RhoGEF-overexpression and TAC increased cell size, whereas p63RhoGEF depletion reduced it.

Summary The presented data show for the first time that RhoA is activated in healthy adult cardiomyocytes in response to important cardiovascular GPCR ligands. Disturbances of the sarcolemmal organization ultimately lead to uncoupling of RhoA from its physiological signaling context. p63RhoGEF, verified as a direct mediator of the $G_{q/11}$ protein-dependent RhoA activation, plays an additional role in the regulation of RhoA and of membranous compartments in adult cardiomyocytes. Most importantly, its depletion leads to an uncoupling of RhoA from its signaling context.

List of Abbreviations

2D	two-dimensional
3D	three-dimensional
ACE	angiotensin-converting enzyme
AngII	angiotensin II
ANP	atrial natriuretic peptide
AP	action potential
AT1R	angiotensin II type 1 receptor
β-AR	β-adrenergic receptors
Ca^{2+}	calcium
cAMP	cyclic adenosine monophosphate
CO_2	carbon dioxide
DAG	diacylglycerol
DAPI	4',6-Diamidin-2-phenylidol
Dbl	diffuse B-cell lymphoma
DH	Dbl homology
DOCK	dedicator of cytokinesis related proteins
DMEM	Dulbecco's Modified Eagle Medium
EGFP	enhanced green fluorescent protein
EHM	engineered heart muscle
ER	endoplasmic reticulum
ERK1/2	extracellular signal-regulated kinase 1 and 2
ESC	European Society of Cardiology
ET-1	endothelin-1
FAK	focal adhesion kinase
FAS	fractional area shortening
FRET	Förster resonance energy transfer
G protein	guanine nucleotide regulatory protein
GAP	GTPase activating protein
GDI	guanine nucleotide dissociation inhibitor
GDP	guanosine diphosphate
GEF	guanine nucleotide exchange factor
G_i proteins	inhibitory G proteins
GPCR	G protein-coupled receptor
G_s proteins	stimulatory G proteins
GTP	guanosine triphosphate

List of Abbreviations

GTPase	guanosine triphosphate hydrolase
HF	heart failure
I/R	ischemia/reperfusion
IP3	inositol 1,4,5-triphosphate
KO	knockout
LARG	leukemia-associated RhoGEF
LV	left ventricle
MβCD	methyl-β-cyclodextrin
NCX	Na^+/Ca^{2+} exchanger
NRCM	neonatal rat cardiomyocytes
PCR	polymerase chain reaction
PE	phenylephrine
PFA	Paraformaldehyde
PH	pleckstrin homology
PI3K	phosphatidylinositol-3-kinase
PIP2	phosphatidylinositol 4,5 biphosphate
PIP3	phosphatidylinositol 3,4,5 triphosphate
PKA	protein kinase A
PKC	protein kinase C
PLC	phospholipase C
PTEN	phosphatase and tensin homolog
RBD	RhoA-binding domain
rER	rough endoplasmic reticulum
RFU	relative fluorescence unit
RhoA	Ras homolog (gene)family member A
RNA	ribonucleic acid
SERCA	sarco-endoplasmic reticulum Ca^{2+} transporter
sh	short hairpin
SICM	scanning ion conductance microscopy
SR	sarcoplasmic reticulum
TAC	transverse aortic constriction
TBS	Tris-buffered saline
TEMED	Tetramethylethylenediamine
TT	transverse tubules
WHO	World Health Organization
WT	wildtype

List of Abbreviations

Symbols and units

α	alpha
β	beta
%	percent
°C	degree Celsius
Da	Dalton
g	gram
sec	seconds
h	hour
L	Liter
μ	micro (10^{-6})
m	milli (10^{-3})
min	Minute
M	molar concentration

List of Figures

List of Figures

List of Tables

1. Introduction

1.1 Heart failure and cardiac remodeling

According to the World Health Statistics 2017 of the World Health Organization (WHO), 17.7 million people died of cardiovascular diseases in 2015, representing 31% of all global deaths. 7.4 million of those patients suffered from coronary heart disease, which ultimately leads to heart failure (HF) and patients death [1].

In general, HF is defined as an abnormality of the cardiac structure or function leading to failure of the heart to deliver sufficient oxygen to the metabolizing tissues [2]. Clinically, HF has been defined by the European Society of Cardiology (ESC) in their *Guidelines for the diagnosis and treatment of acute and chronic heart failure* as "a clinical syndrome characterized by typical symptoms, e.g. breathlessness, ankle swelling and fatigue, that may be accompanied by signs like elevated jugular venous pressure, pulmonary crackles and peripheral oedema caused by a structural and/or functional cardiac abnormality, resulting in a reduced cardiac output" [3]. HF can be caused by various diseases and risk factors such as chronic cardiac stress, pressure or volume overload, or injury caused by myocardial infarction or ischemia and by inherited diseases [4].

Parameters to quantify the left ventricular (LV) remodeling which accompanies HF development include heart size, shape and mass, ejection fraction, end-diastolic and end-systolic volumes as well as peak force of contraction. However, HF is a disease of high complexity which cannot only be classified based on generalized values [5]. Nevertheless, reduced LV ejection fractions are usually associated with a poor prognosis in HF [6].

In 2000, a consensus paper in the Journal of the American College of Cardiology summarized the typical cardiac remodeling mechanisms occurring during the development of HF. According to this generalized overview, HF is characterized by genome expression, molecular, cellular and interstitial changes that result in changes of size, shape and function of the heart after cardiac injury [7].

On the organ level, the development of HF is accompanied by changes in geometry. After ischemic insults and due to volume overload, an eccentric hypertrophy can be observed. This means that the heart becomes less elliptical and more spherical with thinner walls [8]. On the other hand, pressure overload leads to a phenomenon known as concentric hypertrophy which

is characterized by an increased left ventricular wall thickness without or with less increase in chamber size [9].

At the cellular level, the main components of cardiac remodeling are: hypertrophy of cardiomyocytes [10], formation of fibrosis [11] characterized by an increased collagen content, proliferation of fibroblast [12] and apoptosis [13-15]. Upon an ischemic event, fibroblasts and endothelial cells are activated which leads to collagen synthesis and fibrosis [16]. In addition, collagenases are activated which might lead to an increase in ventricular chamber size and thereby to an impaired heart function [17, 18]. Furthermore, ongoing myocyte apoptosis also leads to a progressive left ventricular dysfunction [15]. The remodeling of cardiac myocytes will be discussed in detail in the next chapter.

1.2 Cardiomyocytes: Structure, function and remodeling in disease

The heart mainly consists of two different cell populations: the cardiomyocytes, represented with 30-35%, and non-cardiomyocytes [19]. Despite the relatively low percentage proportion, cardiomyocytes occupy 70% to 85% of the total volume of the heart [20]. These cells are required to generate the contractile force of the heart. Thus, they ensure blood perfusion of all organs and tissues and thereby their oxygen supply [21]. In the group of non-myocytes, endothelial cells with ~45% and fibroblasts with ~11% are the most abundantly represented cell types [22].

1.2.1 Cardiomyocyte membrane structures

Adult cardiomyocytes are rod shaped, often binucleated and highly specialized cells with a complex architecture that allows an efficient and synchronous contraction of the cell [23]. Their cytoarchitecture is maintained by the cytoskeleton. The highly organized sarcomeres are laterally aligned and transduce mechanical signals. Between strictly ordered rows of contractile proteins forming the myofibrils, the sarcoplasmic reticulum (SR) and mitochondria cover about 30% of the cell volume [24, 25].

The complex interplay between structures of the plasma membrane, which is called sarcolemma, the transverse tubules (TT), the SR and the sarcomere forms the basis for each contraction. TT are long membrane invaginations which provide the close proximity between the cell surface and the SR, the intracellular calcium store [26]. TT are 150 nm - 300 nm wide tube-like structures of the surface sarcolemma which are observed in myocytes from all mammalian species that have been studied so far. They form a network of transverse elements

penetrating the cell in regular intervals at the sarcomeric Z-lines and of longitudinal elements between the Z-lines [27, 28]. The TT membrane contains all major channel types that are important for heart function including L-type calcium channels, sodium channels, potassium channels and transporters like the Na^+/Ca^+ exchanger [29-33].

The cardiomyocyte surface membrane, sarcolemma as well as the TT are composed of proteins, cholesterol, glycero-, phospho-, and sphingolipids. Sphingolipids and cholesterol can laterally associate with each other and form so called lipid rafts [34, 35]. One class of lipid rafts, which play an important role in cardiac muscle, are caveolae. Caveolae are invaginations of the membrane with a flask-shaped structure and a diameter of 50 nm - 100 nm [36]. They are shaped and supported by caveolins [37]. Three different caveolin isoforms are currently known: caveolin-1, caveolin-2 and caveolin-3 [38]. Caveolin-3 has been shown to be essential for the formation of caveolae in myocytes [39]. Other studies also suggested the expression of caveolin-1 and caveolin-2 and their interaction with caveolin-3 in cardiomyocytes [40-43]. But there have also been opposing results indicating that caveolin-1 and -2 cannot be detected in ventricular myocytes [44, 45].

In contrast to the expression of caveolin-1 and -2 in cardiomyocytes, it is generally accepted that caveolae and caveolins participate in the organization of macromolecular complexes to ensure efficient signaling. Part of these complexes are, for example, G protein-coupled receptors, heterotrimeric G proteins, ion channels and a broad range of downstream signaling molecules [46, 47]. It has for example been shown that the localization of L-type calcium channels to a caveolar signaling complex is required for the β_2-adrenergic regulation of the calcium inward current [48]. Furthermore, the important role of caveolae and compartmentation for signaling was impressively demonstrated by the treatment of NRCM with methyl-β-cyclodextrin (MβCD) for cholesterol depletion. In this study, the caveolae- and stretch-dependent activation of RhoA, a member of the Rho GTPases (which will be introduced in Chapter 1.4.1), and the transduction of mechanical force into signaling was shown to fail after disruption of the caveolae [49].

Besides the membrane systems which are important for organizing cardiomyocyte signaling and electromechanical coupling, the cells possess endomembranes engaged in secretory processes. Lipids and membrane proteins which are synthesized at the rough endoplasmic reticulum (rER), are transported to the plasma membrane via the Golgi apparatus. In contrast to other cells, like cardiac fibroblasts, the rER seems to be less extended in cardiomyocytes and mainly localized at the perinuclear region (reviewed in: Doroudgar *et al.*) [50]. Similar, the Golgi apparatus in adult cardiomyocytes is less extended and does not show the typical polarity and stack organization. In cardiomyocytes, Golgi apparatus speckles were found at the nuclear

poles representing the cis-part of the Golgi apparatus. The trans-Golgi apparatus compartment in contrast was described to be localized close to mitochondria and dispersed all over the cell [51].

1.2.2 Cardiomyocyte function

In contrast to the other cell types in the heart, cardiomyocytes have the ability to translate electrical excitation into mechanical contraction; a process called excitation-contraction coupling [52].

With every single beat, the heart contracts (systole) and relaxes (diastole) to ensure the supply of the body with oxygen and nutrients. The repetitive contraction of the myocardium is initiated by the formation of an action potential (AP) in the sinoatrial node. The generated electrical impulse then spreads over the atrioventricular node, passing the bundles of His and the Purkinje fibers to propagate simultaneously over the ventricular myocardium and trigger the synchronous contraction [53].

The incoming cardiac AP initiates the excitation-contraction coupling. It activates and thus opens voltage-dependent L-type calcium channels. The cytosolic influx of calcium (Ca^{2+}) into the dyadic space triggers the release of large amounts of Ca^{2+} from the SR via the Ca^{2+} release ryanodine receptor channel (calcium-induced calcium release). The SR represents the intracellular Ca^{2+} storage. The dyadic space, which is formed by the close association (~15 nm) of L-type Ca^{2+} channels in the TT and ryanodine receptors in the SR, ensures a spatially and temporally synchronous and fast Ca^{2+} release [54]. The large amount of Ca^{2+} released into the cytosol from the SR binds to troponin C. This leads to a conformational change and thus to the release of the actin-inhibiting troponin I. As a result, cross-bridges are formed between actin and myosin under ATP hydrolysis [55]. For relaxation of the cardiomyocyte in diastole, the cytosolic Ca^{2+} is recycled via the sarco-endoplasmic reticulum Ca^{2+} transporter (SERCA) into the SR and a smaller amount is removed from the cytosol into the extracellular space via the Na^+/Ca^{2+} exchanger (NCX) [56].

1.2.3 Remodeling of cardiomyocytes in disease

In response to various pathological stimuli, cardiomyocytes often undergo hypertrophy. In early pathological stages this hypertrophic growth is usually protective because it allows the heart to generate sufficient contractile force. However, ongoing hypertrophic growth often leads to HF [21]. As previously mentioned, HF is a disease which is characterized by the reduced contractile capacity of the heart. This is in part due to a disturbed function of the

cardiomyocytes. Factors being involved in the reduced contractile capacity of the cell are for example remodeling of the sarcolemma and thereby defective cardiomyocyte Ca^{2+} handling. As previously described, an intact TT-system is necessary for functional Ca^{2+} handling since the close proximity of L-type Ca^{2+} channels and ryanodine receptors ensures a synchronous Ca^{2+} release. Therefore, TT remodeling can lead to changes in the dyadic space and thereby to an unregulated and asynchronous Ca^{2+} release which contributes to the contractile dysfunction in failing hearts. It has been shown that, as a consequence of TT-remodeling, a reduced Ca^{2+} release synchronicity results in increased time to reach the Ca^{2+} release peak, to lower intracellular Ca^{2+} concentrations and finally to decreased contraction force. [57-59]. Several other studies pointed out that remodeling of the cardiomyocyte membrane network and TT plays an important role during the development of HF and in terminally failing hearts [57, 60]. Additionally, the close connection between TT, signaling molecules and caveolin-3 in failing hearts was demonstrated by the overexpression of caveolin-3 in failing cardiomyocytes. As a result, the disordered localization of β_2-adrenergic receptors could be restored by overexpression of caveolin-3 [61].

On top of the broad field of changes in the cardiomyocyte membrane structures of failing hearts, also morphological changes of the Golgi apparatus were reported which had an influence on its central role in protein processing and secretion pathways. These changes included an increase in size and complexity together with the development of hypertrophy and hyperplasia of the Golgi apparatus [62-64]. Finally, in addition to the previously described severe changes, diseased cardiomyocytes showed strong remodeling of the highly organized sarcomere, characterized by increased viscosity and stiffness resulting in reduced contractility [65, 66].

1.3   G protein-coupled receptor signaling in cardiomyocytes

G protein-coupled receptors (GPCRs) are located in the plasma membrane of all cells. They represent direct targets of over a third of the currently approved cardiovascular drugs [67, 68]. This already indicates that GPCRs play a very important role in cardiac health and disease.

All GPCRs possess seven membrane-spanning α-helical segments separated by alternating intracellular and extracellular loop regions [69]. Upon binding of a ligand to the extracellular side of the GPCR, a conformational change leads to interaction and dissociation of the intracellularly coupled heterotrimeric guanine nucleotide regulatory proteins (G proteins) [70-74]. As indicated by their name, heterotrimeric G proteins consist of three subunits: α, β and γ. Upon activation of a GPCR by a specific ligand, GDP, which is bound by the inactive G

protein, is released from the α-subunit allowing GTP to enter the binding pocket. This induces a conformational change which results in the dissociation of the Gα and G$\beta\gamma$ subunits leading to the activation of specific downstream signal mediators [75, 76]. The major GPCR targets in the treatment of HF are the catecholamine-activated β-adrenoceptors and the angiotensin II type 1 receptor (AT1R) [77, 78].

1.3.1 β-adrenergic receptors in health and disease

Adrenergic receptors play an important role in the translation of signals from the sympathetic nervous system to the cardiovascular system. At present, β-adrenergic receptors (β-AR) of the subtypes β_1, β_2 and β_3 are distinguished. In the healthy heart, signaling by β_1- and β_2-AR is coupled primarily to stimulatory G proteins (G$_s$) which activate adenylyl cyclases and thereby increase the level of cyclic adenosine monophosphate (cAMP) to regulate heart rate and contractility [79, 80]. The identified coupling of β_2-AR to inhibitory G proteins (G$_i$) has been shown to have deleterious effects, potentially through the negative regulation of Ca^{2+} dynamics by the reduced phosphorylation of troponin I and phospholamban [81]. This unusual coupling results from phosphorylation of the β_2-AR by protein kinase A (PKA). During HF, chronic catecholamine stimulation leads to a change in the ratio between β_1-AR and β_2-AR from 80:20 in healthy hearts to 60:40 in failing hearts. In addition, and as a consequence of chronic stimulation, the heart develops hypertrophy and apoptosis of the myocytes accompanied by contractile dysfunction [82, 83]. β_3-AR can couple to both, G$_s$ and G$_i$ proteins [84]. In the human heart, β_3-AR-mediated G$_i$ signaling has a negative inotropic effect which could be involved in pathophysiological mechanism leading to HF [85]. Additionally, for transgenic mice with cardiac overexpression of human β_3-AR coupled to G$_s$ proteins, a positive inotropic effect has been shown [86].

In 2010, a study by Nikolaev *et al*. used a combination of live-cell scanning ion conductance microscopy (SICM) and a specifically designed cAMP FRET sensor to show that β-receptors are significantly redistributed in diseased cardiomyocytes. The authors found that in healthy myocytes, β_2-AR induced cAMP signals were localized exclusively to the TT while β_1 adrenergic receptors were distributed across the entire cell surface. In myocytes from rats with chronic HF, β_2-AR were redistributed from the TT to the sarcolemma, leading to diffuse cAMP signaling which could potentially contribute to the failing myocardial phenotype [87]. In addition, Gorelik and colleagues could show that caveolin-3 (which has been introduced in Chapter 1.2.1) plays a crucial role for the localization of β_2-AR and compartmentation of β_2-AR-cAMP signaling to the TT of isolated healthy adult rat ventricular myocytes [61].

1.3.2 Angiotensin II receptors in health and disease

Angiotensin II receptors are activated by angiotensin II (AngII) which for example regulates cardiac contractility and is involved in cardiac remodeling, growth and apoptosis [88]. Angiotensin receptor blockers and angiotensin-converting enzyme (ACE) inhibitors are commonly used to reduce cardiac hypertrophy, to slow the progression of HF and to improve survival in HF patients [84]. Angiotensin II signals are primarily transferred via the G_q-coupled angiotensin II type 1 receptor (AT1R) [89]. Receptor signaling via $G_{q/11}$ proteins leads to stimulation of phospholipase Cβ (PLCβ) which hydrolyzes phosphatidylinositol 4,5 biphosphate (PIP2) into diacylglycerol (DAG) and inositol 1,4,5-triphosphate (IP3). Subsequently, DAG for example activates protein kinase C (PKC) which is important for myocyte apoptosis, and for the activation of hypertrophic gene transcription [90, 91]

Both, up- and downregulation of AT1R have been reported in cardiovascular diseases. AT1R has been shown to be upregulated in hypertrophy and ischemia [92-94]. In human patients with end-stage HF, AT1R has been shown to be downregulated [95, 96].

1.4   RhoGTPases

The family of monomeric Rho guanosine triphosphate hydrolases (GTPases) belongs to the Ras superfamily of G proteins, which in humans is represented by more than 150 proteins. The GTPases with a molecular weight of 20 kDa to 40 kDa can be divided into 5 subfamilies whose other members besides Ras are Rho, Rab, Ran and ARF [97]. Common to all members of the family is the presence of a conserved N-terminally located G box, consisting of the regions G1 to G5. Those regions are important for the conformational change that is induced by the binding of GTP or the hydrolysis of GTP to GDP [98].

The Rho GTPase family consists of 20 members with a detailed classification into 8 subfamilies, of which five are typical GTPases and three are atypical GTPases. Atypical Rho GTPases differ from the typical ones in having a modification at the guanosine triphosphate/guanosine diphosphate (GTP/GDP) binding region [99]. In line with other GTPases, the typical Rho GTPases act as molecular switches cycling between an active GTP-bound and an inactive GDP-bound state [100]. The activation of Rho GTPases can be regulated by a variety of up-stream signal mediators, including GPCRs, adhesion receptors like integrins, cytokines and tyrosine kinase [101, 102].

Besides the activation through binding of GTP, Rho GTPase signaling is regulated by three additional types of proteins: Guanine nucleotide exchange factors (GEFs), GTPase activating proteins (GAPs), and guanine nucleotide dissociation inhibitors (GDIs). The relatively slow dissociation of GDP and the resulting activation by binding of GTP is accelerated by GEFs. The inactivation and associated GTP to GDP hydrolysis is accelerated by GAPs [103]. In addition to the switch between active and inactive Rho GTPases, it was shown that binding of GDIs leads to an inhibition of the release of GDP/GTP and an associated retention in the cytosol instead of a translocation to the membrane [104, 105].

1.4.1 RhoA activation

RhoA, a small GTPase, belongs to the previously described Ras superfamily and in detail to the subfamily of Rho GTPases. RhoA is one of the most extensively studied members of Rho GTPases besides Rac1 and Cdc42. Initially, RhoA was investigated in swiss 3T3 fibroblasts by Ridley and Hall in 1992. By extracellular stimulation with growth factors, this study showed an association of RhoA with the formation of actin stress fibers and focal adhesions [106].

As described earlier for Rho GTPases in general, RhoA cycles between an active GTP-bound and inactive GDP-bound state [103]. This activation is catalyzed by various GEFs. The catalytic DH domain (Dbl homologous domain) of the GEFs, specifically the segments $\alpha 1$, $\alpha 5$, and $\alpha 6$, forms a stable nucleotide free complex with the switch 1 and switch 2 region of RhoA. In this conformation the GDP/GTP exchange can take place and RhoA becomes active. Active RhoA is predominately located at the plasma membrane [107].

As mentioned before, the activity of GTPases is also regulated by RhoGDIs. In the case of RhoA it has been shown that C-terminal post-translational modifications such as isoprenylation and phosphorylation can alter both localization and activity. Upon isoprenylation of the C-terminus, RhoA localizes to the membrane and free diffusion through the cytoplasm is prevented, thereby also affecting its activity because the regulating RhoGEFs are also localized to the membrane [108]. On the other hand, lipid modifications also serve to regulate activity through RhoGDIs. Through interaction with lipid modifications, RhoA is released from the membrane and diffuses through the cytosol [109-111]. Phosphorylation of RhoA by the cAMP-dependent protein kinase A (PKA), has been shown to result in an enhanced interaction with RhoGDIs. As a consequence, phosphorylated RhoA complexes with the RhoGDIs which provides a further mechanism for regulation of activity besides GDP/GTP cycling [112, 113].

Of special importance for the heart is the activation of RhoA by GPCRs. Here, GPCRs which couple to the G protein subfamilies $G_{q/11}$ and $G_{12/13}$ are best investigated including the α-

adrenoceptors and endothelin-1 receptors. These G protein subfamilies had been demonstrated to interact with and to activate a subset of RhoGEFs directly leading to RhoA activation. For $G_{12/13}$ proteins, the three GEFs p115RhoGEF, PDZRhoGEF, leukemia-associated RhoGEF (LARG, RhoGEF12) are well described to activate RhoA in diverse cell types. In cardiomyocytes, a contribution of p115RhoGEF and LARG in GPCR-induced signaling has been demonstrated so far [114, 115]. $G_{q/11}$ protein-dependent RhoA activation is mediated by a different subset of RhoGEFs. This includes p63RhoGEF, kalirin and Trio [116]. Amongst these, p63RhoGEF is the best characterized in the context of GPCR signaling and is described below in more detail.

1.4.2 RhoA in diseased cardiomyocytes

Early studies in neonatal cardiomyocytes suggested that RhoA is involved in pro-hypertrophic processes. RhoA was found to regulate the expression of hypertrophy-associated genes like the atrial natriuretic peptide (ANP) and to control myofibrillogenesis [117, 118]. In accordance, RhoA was activated downstream of hypertrophy-inducing GPCRs including endothelin-1-, angiotensin II type I and α-adrenergic receptors [117-119]. Moreover, Del Re *et al*. demonstrated by adenoviral overexpression of active RhoA in neonatal rat cardiomyocytes (NRCM), on the one hand the induction, on the other hand the protection from apoptosis. As a result of the high level expression of active RhoA, hypertrophy was induced in cardiomyocytes which in further progression led to apoptosis. The reason was caspase-9 activation and nucleosomal DNA fragmentation. [120]. On the other hand, the authors showed that moderate chronic RhoA activation in cardiomyocytes could protect against the apoptotic effects induced by H_2O_2, glucose deprivation and stretch. [121].

This ambivalent role of RhoA in cardiomyocytes was further supported by genetic mouse models. Constitutive overexpression of wild type RhoA in cardiomyocytes increased ANP expression and let to atrial hypertrophy whereas the left ventricle was dilated and fibrotic. The contractile function was impaired, the heart rate reduced, and AV blocks occurred. The overall mortality was strongly increased. These effects were gene dose dependent [122]. By a conditional model, it could be shown that only when constitutively active RhoA is expressed during development, cardiac hypertrophy occurred in adulthood. In mice starting to overexpress active RhoA at 3 weeks of age, no hypertrophy and fibrosis were detectable. Instead, mice exposed to ischemia/reperfusion (I/R) injury with increased expression of active RhoA showed increased tolerance to I/R with reduced myocardial infarct sizes due to an unexpectedly increased activity of protein kinase D [123].

To investigate the opposite approach, the cardiomyocyte-specific deletion of RhoA in combination with transverse aortic constriction (TAC) or I/R injury was investigated. The absence of RhoA in cardiomyocytes had no effect on functional and structural properties. Also, a comparable development of hypertrophy induced by pressure overload was observed. After long term TAC, the influence of the absent RhoA changed impressively. The hearts showed more pronounced dilations with increased chamber sizes and limited contractile function (dilated cardiomyopathy, acceleration of HF). Also for I/R injury, the model showed less tolerance to the intervention, which was reflected by enlarged infarct sizes. The pathophysiological effects of the TAC intervention were reflected by impaired Ca^{2+} signaling and decreased activity of extracellular signal-regulated kinase 1 and 2 (ERK 1/2) and AKT. In contrast to those deleterious effects, hearts from mice with the cardiomyocyte-specific RhoA deficiency showed less fibrosis, indicating that RhoA mediates both, cardio-protective and cardio-deleterious effects [123, 124].

Various approaches investigated the impact of total RhoA in different disease models, such as TAC and I/R, over a period of eight to ten weeks. Deviating from this, Takefuji *et al.* investigated the changes in the ratio of active RhoA to total RhoA for short term (24 to 72 hours), middle term (4 weeks) and long term (1 year) periods after the TAC intervention. In that study, a rapidly increased and preserved activation of RhoA together with a constant amount of total RhoA was shown for short term and middle term. One year after the TAC intervention, there was still a significant increased ratio of active RhoA to total RhoA [114]. Likewise, in human hearts from patients with congestive heart failure, RhoA activity was shown to be up-regulated [125].

Taken together, previous studies imply a beneficial role for low levels of active RhoA during the onset of cardiovascular diseases, but a detrimental role of high amounts of RhoA under basal conditions. Moreover, the loss of RhoA in diseased cardiomyocytes was found to be protective and deleterious at the same time.

1.5   Rho guanine nucleotide exchange factors (RhoGEFs)

The human genome encodes for 82 RhoGEFs divided into two families. The smaller family of DOCK (dedicator of cytokinesis related proteins) consists of 11 members [126] whereas the larger family with 71 protein members is represented by the Dbl (diffuse B-cell lymphoma)-like family [127].

In 1985, eponymous for the Dbl-like family, the first mammalian GEF Dbl was isolated. Dbl is a human oncogenic protein that has been isolated from diffuse B-cell lymphoma and was

subsequently shown to have a sequence homology of approximately 180 amino acids with the Rho family guanine nucleotide exchange factor CDC24 in yeast [128]. Furthermore, the catalytic activity of this domain for GDP dissociation and nucleotide exchange on human Cdc42 was shown [129]. This led to the identification of the conserved Dbl homology (DH) domain, which can be found in all RhoGEFs other than DOCK proteins [130].

By binding of the DH domain to the GDP bound Rho GTPase, a conformational change occurs and GDP is released. Due to the stabilization of the high affinity intermediate and the cellular favorable ratio of GTP to GDP (~10:1), GTP can rapidly bind to the RhoGTPase [131]. The specificity of individual GEFs for the Rho GTPases in signaling is determined by their sequence as well as by spatial and temporal locations in combination with membrane compartmentalization in the cell [132, 133].

Common to all RhoGEFs of the Dbl-like subfamily is the pleckstrin homology (PH) domain which directly follows the DH domain. Both together form an invariant tandem which serves as a minimal unit. The PH domain consists of 100 to 120 amino acids, often being found in proteins involved in signaling with localization close to the membrane [134]. The PH domain can influence the activity and localization of the GEF in the cell. RhoGEFs with a missing PH domain can show a lower or higher nucleotide exchange activity compared to RhoGEFs with the complete DH-PH tandem motif [135, 136]. The increase in activity might result from the relieve of an autoinhibitory constraint [137]. Furthermore, with the help of the PH domain, RhoGEFs of the Dbl family bind to phosphoinositide, thus supporting their localization to the membrane, but without an effect on the catalytic activity [138].

1.5.1 p63RhoGEF structure and signaling

p63RhoGEF was first investigated in 2001 by Souchet and colleagues in human heart and brain tissue [139]. The nucleotide exchange factor has a size of 63 kDa with 580 amino acids and is encoded by the gene ARHGEF25. Due to its main structural feature, the DH-PH tandem motif, p63RhoGEF is a member of the Dbl-like family. In contrast to other multi-domain GEFs, p63RhoGEF does not possess any other domains than the minimal unit. The N- and C-terminal sequences are largely unstructured [116]. The ability of p63RhoGEF to activate RhoA is without doubt and has been demonstrated by different groups [139-141]. However, there is still a debate whether p63RhoGEF or its N-terminally truncated splice variant GEFT, missing the first 106 amino acids, can activate Rac1 and CDC42 [140, 142]. In addition to p63RhoGEF and GEFT, an additional longer variant with 618 (mouse) or 619 (human) amino acids and a different N-terminus was identified. For this variant either only Rac1 and CDC42, but no RhoA activation [142] or RhoA and Cdc42, but no Rac1 activation was demonstrated [143]. Whether

or not p63RhoGEF and its variants context-wise activate different RhoGTPases needs to be investigated further. However, based on genome analysis it is clear that there is only one ARHGEF25 gene which gives rise to several splice variants [141, 143, 144].

Consistent with other GEFs, the DH domain of p63RhoGEF exerts the catalytic activity for the exchange of GDP to GTP for RhoGTPases, whereas the PH domain is responsible for the regulation of its activity. The PH domain acts on the one hand as an inhibitor for the DH domain and serves on the other hand as binding site for active $G\alpha_{q/11}$ subunits of heterotrimeric G proteins. Thus, by interaction of the $G\alpha_{q/11}$ subunits with a conserved amphipathic helical extension of the PH domain and by the resulting conformational change, the autoinhibition is abolished [116, 137, 145]. As p63RhoGEF shows no other domains apart from the tandem motif, all variants of p63RhoGEF are likely to represent a direct link between GPCRs, the subsequent heterotrimeric G proteins, and RhoA. In line with this hypothesis, an N-terminally truncated version of p63RhoGEF, representing the sequence of GEFT, was sufficient to augment GPCR-driven RhoA and SRF activation [116]. In contrast to other RhoGEFs whose localization is altered by modifications of the PH domain, p63RhoGEF was found to be palmitoylated at a cysteine stretch in the N-terminus, which confines its permanent localization at the plasma membrane. In contrast, the long human 619 amino acid p63RhoGEF as well as GEFT cannot be palmitoylated due to the differences in the N-termini and are localized in the cytosol under basal conditions. However, in response to activation both variants were translocated to the plasma membrane and transported back into the cytosol when the signal ended [136, 143, 146].

Although, p63RhoGEF was primarily detected by Northern blot analysis in human heart and brain tissue, its expression seems to be less restrictive as initially supposed [139, 144]. Since then, the protein has been detected in different other cell types including cancer cells [147], osteoblasts [148], vascular smooth muscle cells [149, 150] and cardiac fibroblasts [151]. However, so far no extensive localization studies of the endogenous protein are available, likely due to the lack of appropriate antibodies. Interestingly, with two different non-commercially available antibodies two independent groups demonstrated its localization in adult heart tissue. Souchet and colleagues suggested that p63RhoGEF mainly resides in the I-band of the sarcomere, whereas Smith and colleagues found a strong sarcolemmal and a minimal sarcomeric localization [139, 142].

The role of p63RhoGEF in the cardiovascular system has been mainly unraveled for vascular smooth muscle cells so far. In rat aortic smooth muscle cells, it was shown that p63RhoGEF is an important mediator of the angiotensin-II dependent RhoA activation and that it triggered cellular processes, such as proliferation and contraction [150]. In portal veins, p63RhoGEF

was demonstrated to be involved in the endothelin-1 and phenylephrine induced contraction [149]. These data suggest that p63RhoGEF is involved in the regulation of vascular contractility. However, p63RhoGEF levels were in addition found to be increased in mononuclear cells of hypertensive patients and reduced after treatment with the AT1R antagonist Olmesartan indicating that this GEF could play a more general role in cardiovascular diseases like hypertension [152, 153].

Our group investigated p63RhoGEF signaling in cardiac fibroblasts. We could show that p63RhoGEF is upregulated in hearts from mice that had been subjected to a TAC intervention. In 2D cell culture experiments with neonatal rat cardiac fibroblasts we found a prominent AngII-dependent RhoA activation through p63RhoGEF. In addition, 3D engineered heart muscle (EHM) was used to investigate the effects of fibroblasts overexpressing p63RhoGEF or expressing a dominant negative p63RhoGEF version (p63ΔN). While p63RhoGEF expression in cardiac fibroblasts increased EHM resting and twitch tensions, fibroblasts expressing the dominant negative version decreased both, resting and twitch tension. Confocal microscopy experiments revealed the localization of full length p63RhoGEF in the vicinity of WGA-positive membranes and to the trans-Golgi membrane network of cardiac fibroblasts. In contrast, p63ΔN was mainly located in the cytosol of cardiac fibroblasts [151].

2.   Previous results and aims of the project

The nucleotide exchange factor p63RhoGEF was identified by Souchet *et al.* in 2001, being expressed in human heart and brain tissue [139]. Further studies demonstrated its function as a direct mediator of the $G_{q/11}$ protein-dependent RhoA activation in different cell types [116, 149, 150, 154]. However, until now its role for the function of the most important cell type in the heart, the cardiomyocyte, is still not understood. Early investigations of our group (Dr. Christiane Vettel, Medical Faculty Mannheim, Institute for Experimental and Clinical Pharmacology and Toxicology) verified its potential function within this signaling context in neonatal rat cardiomyocytes (NRCM). Out of the three GPCR ligands endothelin-1 (ET-1), phenylephrine (PE) and angiotensin II (AngII), ET-1 was most effective in RhoA activation and was thus used for further examinations (Fig. 1 A). The influence of p63RhoGEF on the ET-1-dependent RhoA activation was then studied by gain- and loss-of-function experiments. As shown in figure 1 B, adenoviral overexpression of p63RhoGEF basally increased RhoA activity and further augmented ET-1-induced RhoA activity. *Vice versa*, the adenovirally mediated knockdown of p63RhoGEF reduced the ET-1-induced RhoA activation by about 50%. Interestingly, the PE-induced RhoA activation was independent of p63RhoGEF in NRCM (Fig. 1 C).
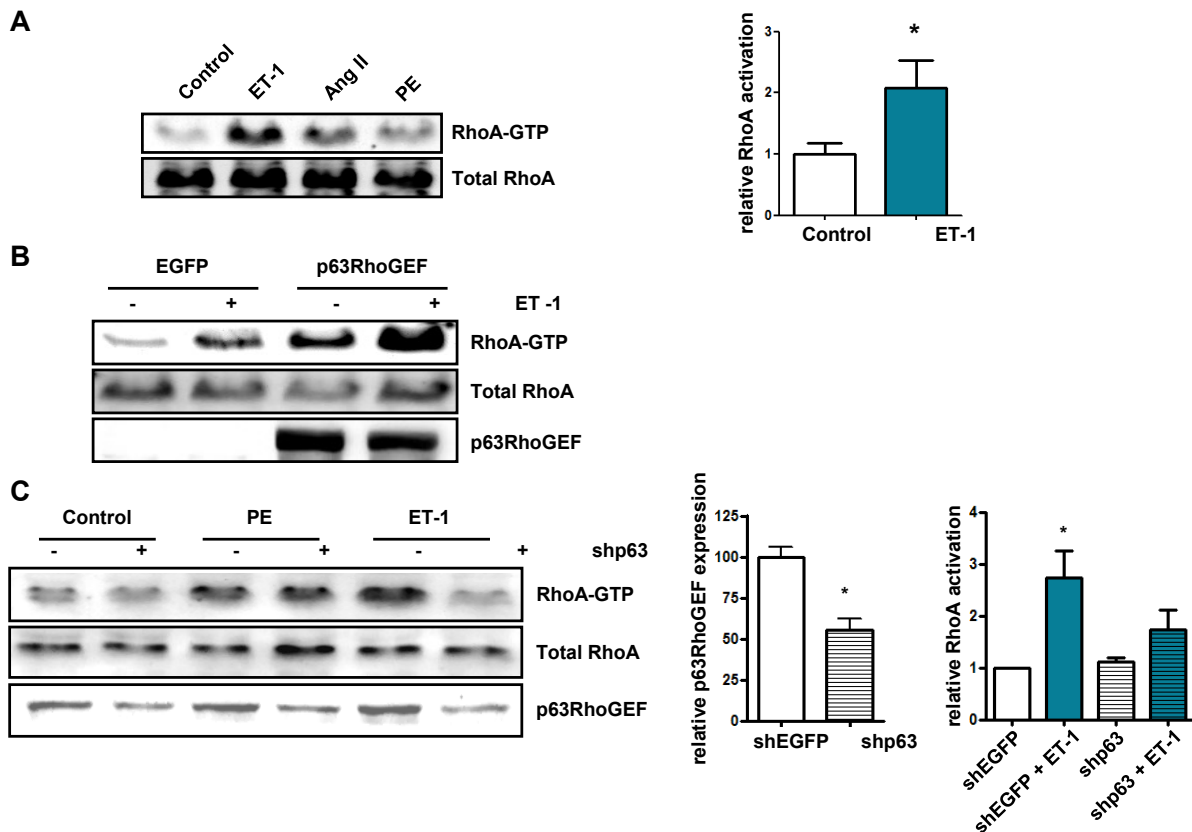
Fig. 1: Impact of p63RhoGEF on the ET-1-, PE- and AngII-dependent RhoA activation in NRCM.
A) Serum-starved NRCM were treated with 100 nM ET-1, 1 µM AngII or 100 µM PE for 30 s and RhoA activation was determined by a pulldown assay. The protein content for RhoA-GTP and total RhoA was determined by immunoblotting. ET-1 induced activation of RhoA is given by the ratio of the stimulated condition to the unstimulated control as mean ± SEM, n=26, *p<0.03 vs. control. **B)** Serum-starved NRCM were transduced for 48 h with recombinant adenoviruses encoding for EGFP only or for full length p63RhoGEF and treated with 100 nM ET-1 for 30 s. For the determination of RhoA activation, a pulldown assay and immunoblot was performed. For the determination of p63RhoGEF expression, an anti-c-myc antibody was used. Representative immunoblots are shown. **C)** Serum-starved NRCM were transduced for 48 h with recombinant adenoviruses encoding for shEGFP or for shp63 and treated with 100 nM ET-1 or 100 µM PE for 30 s. A pulldown assay and subsequent immunoblot was performed for the determination of RhoA activation. In addition, an immunoblot for total RhoA and p63RhoGEF was performed. Changes of p63RhoGEF expression and RhoA activation after treatment with 100 nM ET-1 for shp63 relative to shEGFP are given as mean ± SEM, p63RhoGEF expression n=8, *p<0.05, RhoA activation n=3-4, *p<0.05 vs. control. *Experiments were performed by Christiane Vettel, Medical Faculty Mannheim, Institute for Experimental and Clinical Pharmacology and Toxicology Mannheim; Vettel, C. Dissertation "Charakterisierung des Guaninnukleotid-Austauschfaktors p63RhoGEF als neuen Mediator der Gαq/11-induzierten RhoA-Aktivierung"2009*

These data indicated that p63RhoGEF could indeed play a role in the neurohumoral signaling in diseased cardiomyocytes. This idea was further substantiated by the finding that after transverse aortic constriction, which over time leads to heart failure, p63RhoGEF was up-regulated as shown by quantitative real-time PCR in Fig. 2 [151].
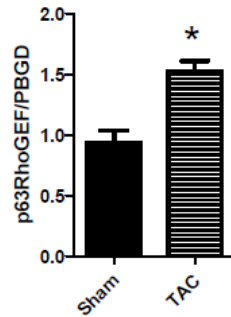
Fig. 2: Expression of p63RhoGEF after transverse aortic constriction (TAC) determined by qPCR.
Hearts of mice (male and female) which had been subjected to TAC were used for RNA isolation and qPCR analysis 7 days after the intervention. p63RhoGEF was normalized to the housekeeping gene PBGD. Values are given as mean ± SEM relative to sham, n=4 (sham), n=8 (TAC), *p<0.05.

Moreover, our group (Dr. Anita Ongherth, Institute of Pharmacology and Toxicology, University Medical Center Göttingen) demonstrated in a parallel study that in mice with a global heterozygous deletion of p63RhoGEF (HET), the cardiac function was impaired already under basal conditions but even more detrimental after transverse aortic constriction as shown in Fig. 3 A. Surprisingly, surviving mice with a homozygous deletion of p63RhoGEF (KO) showed only the same degree of impairment as the corresponding wildtype (WT) littermates (Fig. 3 A). However, the mortality after the TAC procedure was much higher in male p63RhoGEF-KO mice than in WT or HET mice (Fig. 3 B).
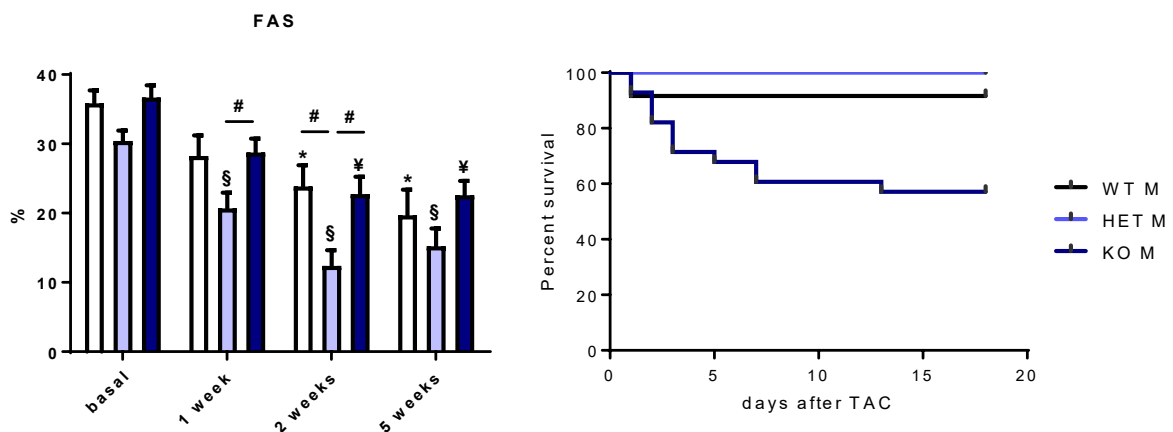
Fig. 3: Impact of genetic deletion of p63RhoGEF for male mice subjected to TAC.
A) Fractional area shortening (FAS) was determined by echocardiography under basal condition, 1 week, 2 weeks and 5 weeks after TAC for wildtype (WT), heterozygous (HET) and homozygous (KO) mice. Values are given as mean ± SEM, *p < 0.05 vs. WT basal group, §p < 0.05 vs. HET basal group, ¥p < 0.05 vs. KO basal group, #p <

0.05 vs. WT and/or KO group were compared by ANOVA or two conditions by an unpaired t-test. **B)** Survival rate of WT, HET and KO male mice in the first 21 days after the TAC intervention.

Based on data on p63RhoGEF in NRCM and the heart as described above, and based on the fact that RhoA activation has never been studied in adult cardiomyocytes, the following aims of this thesis had been defined:

- Characterization of the GPCR-induced RhoA activation and localization in isolated adult mouse cardiomyocytes

- Characterization and determination of the role of p63RhoGEF in adult mouse cardiomyocytes by adenoviral overexpression and a genetic deletion approach

- Investigation of the pathophysiological changes and the relevance of p63RhoGEF and RhoA signaling in diseased cardiomyocytes

3. Materials and Methods

3.1 Animals

All animal experiments were performed in accordance with international and governmental guidelines. All animal strains used in this thesis are listed below.

Tab. 1: Animals

Animals	Source
Wistar Kyoto rat	In house breading
C57BL/6J mice	Charles River
sv129/C57BL/6J	inGenious, NY, USA

3.2 Adenoviruses

Tab. 2: Adenovirus

Adenovirus	Source
Ad-EGFP (EGFP sequence)	Susanne Lutz, Mannheim
Ad-p63RhoGEF (c-myc tag, human p63RhoGEF sequence aa 1-580, EGFP)	Susanne Lutz, Mannheim
Ad-p63ΔN (c-myc tag, human p63RhoGEF sequence aa 295-580, EGFP)	Susanne Lutz, Mannheim

3.3 Chemicals and media

Tab. 3: Chemicals and media

Component	Company
4',6-Diamidin-2-phenylidol (DAPI)	Roche Applied Science, #10236276001
Acetic acid	Carl Roth, #KK62.1
Acrylamide solution rotiphorese gel 30	Carl Roth, #3029.1
Albumin Fraction V	Sigma-Aldrich, #A3311
Ammonium persulfate (APS)	AppliChem, #141138

Angiotensin II, human (AngII)	Sigma-Aldrich, #A9525
Ascorbic acid	AppliChem, #A1052
Bovine serum albumin	Sigma-Aldrich, #A2153
Bromophenol blue	Sigma-Aldrich, #B0126
Calcium chloride ($CaCl_2$)	AppliChem, #A1873
D(+)-Glucose	AppliChem, #A0883
di-Sodium hydrogen phosphate dihydrate	Carl Roth, #4984
Dulbecco's phosphate buffered saline (10 x)	Sigma-Aldrich, #D5652-10X1L
Endothelin-1 (ET-1)	Enzo, #ALX-155-001
Ethidium bromide	Sigma-Aldrich, #E1510
Fluoromount	Sigma-Aldrich, #F4680
Glycerol	AppliChem, #A0970
Glycine	AppliChem, #A3707
HEPES	Carl Roth, #HN77
Igepal CA-630	Sigma-Aldrich, #I8896
Magnesium sulfate heptahydrate $MgSO_4$ x $7H_2O$	Merck, #105886
Methanol	Carl Roth, # 0082
Methyl-β-cyclodextrin (MβCD)	Sigma-Aldrich
Monobasic potassium phosphate (KH_2PO_4)	Carl Roth, #P018
Paraformaldehyde (PFA)	Sigma-Aldrich, P6148
PBS powder	Sigma-Aldrich, #P3813
Phalloidin, FITC labeled	Sigma-Aldrich, #P5282
Phenol red	Sigma-Aldrich, #P0290
Phenylephrine (PE)	Sigma-Aldrich, #P1240000
Ponceau S	Sigma-Aldrich, #P3504
Potassium bicarbonate ($KHCO_3$)	Roth, #P748
Potassium chloride (KCl)	Roth, #HN77
Precision Plus Protein Kaleidoscope Prestained Protein Standards	Bio-Rad, # 1610375
ProLong® Gold Antifade Mountant	Molecular Probes, Life Tech., #P36934

Roti-Block	Carl Roth, #A151
Roti-Immunoblock	Carl Roth, #T144
Rotiphorese Gel 30	Roth, #3029.1
Sodium bicarbonate (NaHCO$_3$)	Carl Roth, #0965
Sodium chloride (NaCl)	Thermo Scientific, #AM9759
Sodium hydroxide (NaOH)	Carl Roth, #K021
SuperSignal™ West Femto Maximum Sensitvity Substrate	Thermo Scientific, #34095
Taurin	Carl Roth, #4721
Tetramethylethylenediamine (TEMED)	Merck, #110732
Tris (ultrapure)	AppliChem, #A1086
Triton-X-100	Carl Roth, #3051
Trypsin 2.5% (10 x)	Gibco, #15090-046
Tween-20	Carl Roth, #9127
β-Mercaptoethanol	AppliChem, #A1108

3.4   Cell culture

Tab. 4: Media

Media	Company
Dulbecco's Balanced Salt Solution DPBS (-Ca2+, -Mg2+)	Gibco, #14190094
Dulbecco's Modified Eagle Medium DMEM Glutamax (1g/L, pyruvic acid)	Gibco, #10567014
Dulbecco's Modified Eagle Medium DMEM (1g/L, NaHCO3)	Merck Millipore, #F0415
Fetal calf serum (FCS)	Gibco, #10270-106
Insulin-Transferrin-Selenium-Ethanolamine	Gibco, #515500056
Laminin (1mg/ml)	Sigma-Aldrich, #L2020
L-Glutamine (200 mM)	Gibco, #25030024
Minimal Essential Medium (MEM)	Gibco, #51200-046

Penicillin/ (1000 U/ml) / Streptomycin 10000 µg/ mL) (P/S)	Gibco, #15140-122
10 x Phosphate-buffered saline pH 7.4 (Ca2+, -Mg2+)	Gibco, 70011-036
10 x Phosphate-buffered saline (10xPBS), pH 7.4	Thermo Scientific, #70011044

3.5 Drugs

Tab. 5: Drugs

Agent	Company
Burpenophin (Temgestic)	Reckitt Benckiser Healthcare
Fentanyl	Rotexmedica
Isoflurane (*Forene)*	Abbvie, #N01AB06
Meatmizol (Novaminsulfon)	Ratiopharm
Medetomidine (Ceptor)	cp Pharma
Midazolam	Rotexmedica

3.6 Enzymes and inhibitors

Tab. 6: Enzymes and inhibitors

Product name	Company
(-)-Blebbistatin	Cayman, #Cay13013
cOmplete Protease Inhibitor cocktail tablets	Roche Applied Science, #04693159001
Liberase DH Research Grade (100 mg)	Roche Applied Science, #05401089001
Phosphatase Inhibitor Cocktail Tablets	Roche Applied Science, #04906837001
Trypsin 2.5% (10x)	Gibco, #15090-046

3.7 Kit

Tab. 7: Kit

Kit	Company
GoTaq G2 Green Master Mix	Promega, #M7822
RhoA G-Lisa activation assay	Cytoskeleton, #BK121
SuperSignal West femto maximum sensitivity substrate	Thermo Scientific, #34095

3.8 Consumables

Tab. 8: Consumables

Consumables	Company
Cell culture dish (100 x 20 mm)	Falcon, #353003
Cell culture dishes (6,10, 15 cm)	Sarstedt/ Graeiner
Cell scraper	Sarstaedt, #83.1830
Coverslips Ø18 mm	Thermo Scientific, Menzel, #CB00180RA1
Filter System 0.2 µm (1 L, 500 mL, 250 mL)	Corning Life Sciences #43051x
Microscope slide 25 x 75 x 1 mm	Thermo Scientific, Menzel #J1800AMNZ
Multi-well cell culture plates (6-, 12-well)	Greiner Bio One
Nail polish	DM drugstore
Nitrocellulose membrane, 0.2 µm	GE Healthcare, #10600001
Pipette tips filtered (10 µL, 100 µL, 200 µL, 500 µL)	Sarstedt
Reaction tube (15 mL, 50 mL)	Greiner Bio One
Reaction tube (0.5 mL, 1.5 mL, 2 mL)	Sarstedt
Serological pipette wide opening (10 mL)	Falcon, #357504
Serological pipettes (5 mL, 10 mL, 25 mL)	Sarstedt, #86.1253.001, #86.1254.001, #861685.001
Syringe filter 0.22µm	Sarstedt, #83.1826.001
Syringe, Omnifix® 40 Solo	Braun, #9161309V

Transfer pipette	Sarstedt, #68.1171

3.9 Devices

3.9.1 General devices

Tab. 9: Devices

Device	Company
BioSafety Cabinet	Prettl, Telstar Bio-II-A
Cell counter	Roche, CASY Counter
Electronic scale	Sartorius, #pt600
Electronical microscale	Sartorius, #AX224
Electrophoresis chamber	Bio-Rad, Mini Protean Tetra Cell
Heating block	Eppendorf, Multimixer compact
Chemiluminescence imaging system	Bio-Rad, #ChemiDoc MP
Incubator	Labotect, C200
PCR	Eppendorf, #Mastercycler gradient
pH meter	Inolab
Power supply	Bio-Rad, Power PAC HD
Table centrifuge	Eppendorf, Centrifuge 5415D
Vibratom	Leica, VT1000S
Vortexer	W.Krannich, VF2
Western blotting system	Bio-Rad, Mini Trans-Blot Cell

3.9.2 Langendorff perfusion system

Tab. 10: Components of the Langendorff perfusion system

Device	Company
3-way Stopcock Connection Tubing	Braun, #Discofix® C 3-way
Heat exchanger coil	Rettberg
Peristaltic pump	Ismatec, #ISM831C

Silicon tubing peristaltic tubing	IDEX Health & Science ,#TYGON R3607)
Stopcock Connection Tubing	Braun, # Discofix® C
Water bath	Pharmacia LKB, #Multi TempII
Cold light source	Zeiss, #Schott KL200
Inverted microscope	Nikon, #TMS-F
Stereo microscope	Zeiss, #Stemi 2000

3.9.3 Microscope

Tab. 11: Microscope

Microscope	Company
Stereoscope	Zeiss, #Lumar.V12
Microscope objective 0.8x	Zeiss, #NeoLumar S 0.8xFL
Microscope camera	Zeiss, #AxioCam MRc
Halogen light source	Zeiss, #KL2500 LCD
Fluorescence lamp	Zeiss, #HXP120C
Confocal laser scanning microscope	Zeiss, LSM 710
Microscope objective 10x	Zeiss, EC Plan-Neofluar 10x/0.3 #440330-9902
Microscope objective 20x	Zeiss, EC Plan-Neofluar 20x/0.5 #440340-9904
Microscope objective 63x	Zeiss, Plan-Apochromat 63x/1.40 NA # 420780-9900-000

3.10 Software

Tab. 12 Software

Program	Provider
Amon32	FMI VitroDat
Endnote X7	Thomson Reuters
Fiji	http://fiji.sc/
ImageJ 1.51a	http://imagej.nih.gov/ij/

Image Lab 5.1	Bio-Rad Laboratories
MATLAB R2012b	MathWorks
Office 2016	Microsoft Inc.
Prism 5.0	GraphPad Software
Xcellence pro	Olympus
Zen 2009	Carl Zeiss
Zen 2012	Carl Zeiss

3.11   Cell Culture

3.11.1 Media and buffers
Tab. 13: Media and buffers

Media and buffers	Composition
Stock Perfusion buffer 10 x	1.13 M NaCL
(adjust pH 7.4, with 2N NaOH, sterile filtration, storage in a water boiled glass bottle)	47 mM KCl
	6 mM KH2PO4
	6 mM Na2HPO4 x 2 H2O
	12 mM MgSO4 x 7 H2O
	100 mM KHCO3
	100 mM HEPES
	in ddH2O
Perfusion buffer 1 x	23 mM NaHCO3
	30 mM Taurine
	5.5 mM Glucose
	9.9 mM BDM
	10% (v/v) Stock Perfusion buffer 10 x
	ad 500 mL ddH2O
CaCl2-solution 1	100 mM CaCl2

sterile filtrated (0.2µm pore size)

CaCl2-solution 2	10 mM CaCl2
	Sterile filtrated (0.2µm pore size)
Liberase solution	0.4% (w/v) Liberase DH
	(bottle contains 50 mg)
	ddH2O.(12 mL)
Digestion buffer	29.6 mL Perfusion buffer 1 x
	3.75 µL Calcium solution 1
	450 µL Liberase solution
	200 µL Trypsin 2.5%
Stopping buffer stock	1% (w/v) BSA
	10 mL Perfusion buffer 1 x
Stopping buffer 1	2.25 mL Stopping buffer
	1.25 µL Calcium solution 1
Stopping buffer 2	4.75 mL Stopping buffer
	1.9 µL Calcium solution 1
Culture medium adult mouse cardiomyocytes (AMCM) incubation for 1 hour in 37°C, 5% CO2	MEM (prewarmed, 37°C,5% CO2)
	0.25% (v/v) (-)-Blebbistatin (0.5 mM)
	1% (w/v) BSA
	1% (v/v) P/S
	1% (v/v) L-Glutamine (200mM)
	1% (v/v) ITS-X

| Laminin solution | 0.01% (w/v) |
| | in AMCM-medium |

3.12   Antibodies

3.12.1 Primary antibodies

Tab. 14: Primary antibodies

Antibody	Company	Application	Dilution
Mouse anti-Active RhoA (RhoA-GTP	NewEast Biosciences, #26007	IF	1:500
Rabbit anti-Caveolin-3	Abcam	IF	1:500
Mouse anti-Caveolin-3	BD Biosciences	IF	1:500
		WB	1:500
Rabbit anti-Myomesin-1	Proteintech	IF	1:500
Rabbit anti-Connexin-43	Sigma-Aldrich	IF	1:500
		WB	1:1000
Rabbit ant-c-myc	Santa Cruz	IF	1:150
Mouse anti-c-myc	Sigma-Aldrich	IF	1:2500
Rabbit anti-KDEL	Abcam, #ab176333	IF	1:100
Mouse anti-GM-130	BD Biosciences, #610822	IF	1:500
Mouse anti-RhoA	Santa Cruz, #sc-418	WB	1:200
Mouse anti- α-actinin	Sigma-Aldrich, #A7811	IF	1:800
		WB	1:2000
Mouse anti- α-tubulin	Sigma-Aldrich	WB	1:2000
Mouse anti-β-actin	Sigma-Aldrich, A2228	WB	1:5000
Rabbit anti-Calsequestrin	Thermo-Fisher, PA1-913	WB	1:2000
Rabbit anti-p63RhoGEF	Proteintech, #51006	WB	1:200
Rabbit anti-GEFT	Proteintech, #14839		
Rabbit anti-Dysbindin	Sigma-Aldrich, #SAB4200409	IF	1:500
Rabbit anti-ERM (Ezrin/Radixin/Moesin)			1:1000

Rabbit anti-P-ERM

(Ezrin/Radixin/Moesin)

3.12.2 Secondary antibodies

Antibody	Company,	Application	Dilution
Anti-mouse IgG linked peroxidase-produced in rabbit	Sigma-Aldrich, #A9044	WB	1:10000
Anti-rabbit IgG linked peroxidase produced in goat	Sigma-Aldrich, #9169	WB	1:40000
AlexFluor®568 goat anti mouse	Life Technologies, # A11004	IF	1:1000
AlexFluor®633 goat anti-rabbit	Life Technologies, # A21070	IF	1:1000

3.13   Solutions for immunostaining

Tab. 15: Solutions for immunostaining

Solution	Composition
4% PFA in PBS (pH 7.4)	4% (w/v) paraformaldehyde 0.01% (v/v) 10 N NaOH 10% (v/v) 10x PBS in ddH$_2$O, pH 7.4, HCl
Permeabilization buffer	0.2% (v/v) Triton-X-100 in 1 x DPBS (-Ca^{2+}, -Mg^{2+})
Blocking buffer (adult mouse ventricular cardiomyocytes)	0.2% Triton-X-100 10% FCS in 1 x DPBS (-Ca^{2+}, -Mg^{2+})

3.14   Solution for immunoblotting

Tab. 16: Solution for immunoblotting

Solution	Components
10% Ammonium persulfate (APS)	10% (w/v) Ammonium persulfate in ddH2O
10% Sodium dodecyl sulfate (SDS)	10% (w/v) Sodium dodecyl sulfate in ddH2O
10x Tris buffered saline buffer (10 x TBS)	1.2% (w/v) Tris 8.8% (w/v) NaCl in ddH2O
4x loading buffer 1 (Laemmli buffer) without glycerol	0.2% (w/v) bromophenol blue 3.6% (w/v) Tris 5.7% (w/v) SDS 10% (v/v) β-mercaptoethanol in ddH2O
4x loading buffer 2 (+ glycerol)	0.2% (w/v) bromophenol blue 3.6% (w/v) Tris 5.7% (w/v) SDS 50% (v/v) glycerol 10% (v/v) β-mercaptoethanol in ddH2O
5x SDS electrophoresis buffer	0.5% SDS 1.5% (w/v) Tris 9.4% (w/v) glycine

	in ddH2O, pH 8.3 HCl
Blocking buffer	10% (v/v) Roti-Block
	in ddH2O
Blotting buffer	0.3% (w/v) Tris
	1.44% (w/v) glycine
	20% (v/v) methanol
	in ddH2O
cOmplete Protease Inhibitor cocktail (7x)	1 tablet in 1.5 mL in DdH2O
Lysis buffer (GST-Fish buffer)	50 mM Tris
	150 mM NaCl
	4 mM MgCl$_2$
	10% (v/v) glycerol
	1% (v/v) IGEPAL CA-630
	in ddH2O
PhosStop Phosphatase Inhibitor cocktail (10x)	1 tablet in 1 mL in ddH2O
Ponceaus S	0.2% (w/v) Ponceau S
	3% acetic acid
	in ddH2O
Tris buffered saline buffer with tween 20 (TBS-T)	0.1%(v/v) tween 20
	10% (v/v) 10 x TBS
	in ddH2O

3.15 Methods

3.15.1 Mouse disease models

All animal procedures were reviewed and approved by international animal care and use committee at University Center Göttingen and by the veterinarian state authority LAVES (Niedersächsisches Landesamt für Verbraucherschutz und Lebensmittelsicherheit) in compliance with the human care use of laboratory animals. During this study, two different mouse models were investigated. To understand signaling processes during pressure overload and the corresponding development of hypertrophy, the transverse aortic constriction model was chosen. To specifically investigate the role of the p63RhoGEF, global hetero- and homozygous knockout mice were used as model organisms.

3.15.2 Transverse aortic constriction (TAC)

TAC surgery was performed by the CRC 1002 service unit, particularly by Sarah Zafar (technical assistant). In brief, 9 weeks old male mice (C57BL/6J, Charles River) were used for the surgery. As pre-operative pain medication, mice were treated with metamizole (1.33 mg/ml) in sugar supplemented drinking water three days before the intervention. Additionally, the animals were subcutaneously injected with buprenorphine 1 h before and 24 h after the intervention. Mice were anesthetized with an intraperitoneal injection of a mixture containing medetomidine (0.5 mg/kg body weight), midazolam (5 mg/kg body weight) and fentanyl (0.05 mg/kg body weight) diluted in 0.9 % physiological salt solution. This combination was injected in a volume of 0.01 mL/g body weight. To antagonize the anesthesia, atipamezole (2.5 mg/kg body weight) and flumazenil (0.5mg/kg body weight) were injected subcutaneously after the surgery.

After fixation of the animal with tape, body temperature was kept at 37°C on a heating plate, the coat on the chest was removed and the dermis was cleaned. After opening the chest upstream to the sternum by a minimal invasive incision the aortic arch was accessible for stricture. Therefore, a 27-gauge spacer was placed close to the aorta between the left and the right carotid artery and the constriction was performed with a suture (6-0). After proper placement of the knot, the spacer was removed, the chest and the skin were closed properly with suture (5-0). During recovery phase, the mice were closely monitored. Daily observation, documentation of the body weight, and metamizole medication were continued for 7 days. Additionally, as control the same number of animals underwent the same intervention with exception for the aortic constriction (sham group). The resulting pressure gradient in the transverse aorta was confirmed by Doppler echocardiography three days after surgery (refer

to chapter 3.15.3). Four weeks after the intervention, cardiomyocytes were isolated from TAC and sham mice by Langendorff perfusion (refer to chapter 3.16.1).

3.15.3 Doppler echocardiography

To determine the pressure gradient in the transverse aorta after TAC, t pulse wave Doppler echocardiography was applied. For that purpose, a 20 Hz transducer (MS250 MicroScan™ transducer) was placed close to the constriction and the blood flow velocity (m/s) was measured three times per mouse. The measured velocity was converted to a pressure gradient (mmHg) using the following calculation:

$$\text{Gradient (mmHg)} = (\text{mean maximal velocity (m/s)})^2 \cdot 4$$

3.15.4 Echocardiography

One week before and 4 weeks after the TAC or sham intervention, mice were characterized by echocardiography. For the measurements, mice were anesthetized with 1-2% (v/v) isoflurane in oxygen (1L/min) and the body temperature was kept to 37°C with a heating plate.

Left ventricular dimensions and wall thicknesses were determined by parasternal long and short axis views. The ejection fraction (EF) was calculated as $EF = (Vol_d - Vol_s) / Vol_d \times 100$ with Vol_d = heart volume in diastole and Vol_s = heart volume in systole. Heart volumes were calculated as $Vol_d = 5/6 \times Area_d \times L_d$ and $Vol_s = 5/6 \times Area_s \times L_s$ with Area denoting the area of the endocardium and L denoting the long heart axis in diastole and systole, respectively.

3.15.5 Transgenic mouse model: p63RhoGEF-knockout

The founder animals for the p63RhoGEF mouse line in Göttingen were purchase from the company Ingenious Targeting Laboratory, Inc. (New York, USA). This mouse line was generated with the Cre/loxP system, by adding two flox elements on chromosome 10 encompassing exon 1 and 2 of the p63RhoGEF gene (Fig. 4).
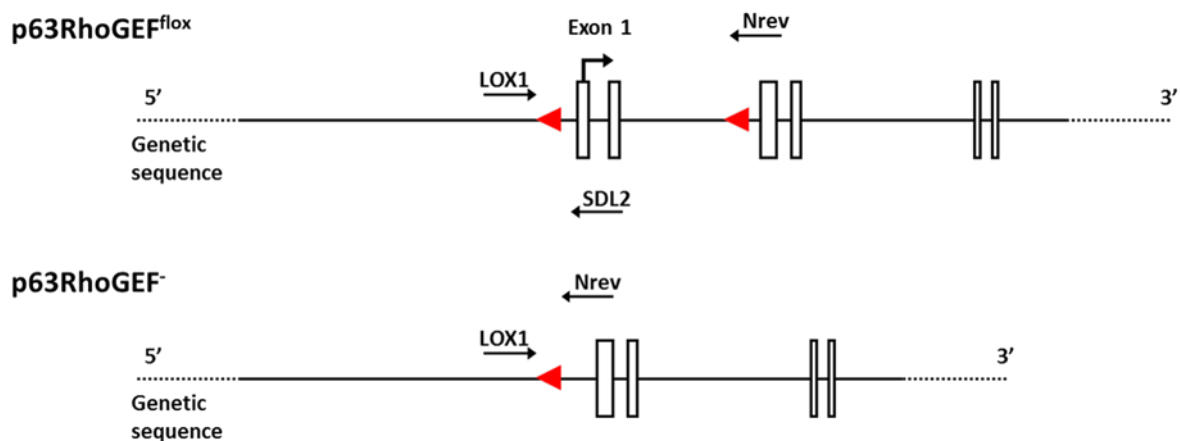
Fig. 4 : Schematic view of the loxP-sites at p63RhoGEF^{flox} and p63RhoGEF⁻ allele

The scheme visualizes the location of the loxP-sites (red arrows) in the sequence of p63RhoGEF on chromosome 10.

In previous work, heterozygous (p63RhoGEF$^{wt/ko}$) were generated and backcrossed with wild type mice (C57BL/6J, Charles River). Male littermate from the second generation (N2) were used for the experiments.

To investigate the influence of p63RhoGEF in cardiomyocyte signaling, cardiomyocytes were isolated from wild type, homozygous and heterozygous knockout male animals at an age between 12 and-20 weeks. To study the role of p63RhoGEF during the development of hypertrophy, transgenic were compared with wild type mice subjected to transverse aortic constriction/intervention (refer to chapter 3.15.2).

3.15.6 Isolation of the DNA for genotyping

For genotyping ear or tail biopsies were used. In brief the biopsies were incubated in 50 µL alkaline lysis buffer for 1 h at 95°C. Then 50 µL neutralization buffer was added. The obtained samples were directly used for PCR reaction. The sequences of the used oligonucleotides, the composition of the PCR samples and the design of the PCR program are listed in the tables below (Tab. 17, Tab. 18,Tab. 19).

Tab. 17: Primer for genotyping

Primer	Sequence (5' to 3')
Lox1 (forward)	CTG GAA TTG CTG CCA GAC TGT AGC
Nrev (reverse)	ATC CTG AGC ATA GCA CAG ATC TGC GG
SDL2 (reverse)	CCA CCG CAG CCA AAC TTC TC

Tab. 18: Master mix for PCR

Components	Volume [µL]
Forward primer (10 pmo)	1
Reverse primer (10 pmol)	1
GoTag Green master mix	10
H_2O	20
Template DNA	1

Tab. 19: PCR cycle program

Step	Time	Cycle
1.Initialization (94°C)	3 min	1x
2. Denaturation (94°C)	30 sec	
3.Annealing (56°C)	30 sec	30x
4.Elongation (72°C)	2 min	
5.Elongation (72°C)	5 min	1x
6.End (4°C)	∞	

The obtained PCR products were separated by gel electrophorese using 1.5% agarose gels in 1x TAE solution, at 120 V for 45 min. The gels were documented with the GelDoc XR device and analyzed with the Quantity One software. The obtained pattern of PCR products of the different genotypes is given in the following table (Tab. 20)

Tab. 20: Genotype specific PCR products

Genotype	Lox1 / SDL2	Lox1 / Nrev
Wildtype (p63RhoGEFflox)	345 bp	no fragment
Heterozygous (p63RhoGEFflox/-)	345 bp	591 bp
Knockout (p63RhoGEF-/-)	no fragment	591 bp

3.16   Cell culture

3.16.1 Isolation of adult mouse ventricular cardiomyocytes

Ventricular myocytes of adult mice were isolated by retrograde Langendorff perfusion using an enzyme composition of collagenase type I and II, dispase (Liberase DH, Roche) and trypsin. Before each isolation, the Langendorff perfusion system was flushed with 50 mL water and 20 mL perfusion buffer while preheating the water bath and the tubing system. A petri dish with rounded black silicon (self-made) was filled with perfusion buffer on ice in a Styrofoam tray. The protocol for the isolation of adult ventricular cardiomyocytes was modified from Borner *et al.* [155].The mice (age of 10 to 20 weeks) were anesthetized with 2% isoflurane in oxygen and sacrificed by cervical dislocation. After fixation on a Styrofoam plate and disinfection with 70% ethanol, the thorax was opened. The heart was isolated by cutting distal from the heart, close to the aortic arch and was directly transferred into ice-cold perfusion buffer. For perfusion, the aorta was cannulated with a buffer-filled modified 20G cannula. The heart was connected to the pre-heated (37°C) perfusion system with a flow of 3.5 mL per min and washed for 30 sec. Afterwards, 29.6 mL digestion buffer was added to the system. During the digestion of the heart, 2.5 mL of digestion buffer was collected in a beaker. After perfusion with 29.6 mL of digestion buffer, the ventricles were separated from the atria, placed into the beaker and further dissected into 1-2 mm^3 pieces. To stop the digestion, 2.5 mL stopping buffer 1 was added and the cardiomyocytes were further homogenized with a wide opening syringe (Braun Omnifix). Undigested tissue was sedimented and removed, while the digested cell suspension was transferred to a 15 mL reaction tube. After sedimentation of the cell suspension (8 min), the supernatant was discarded and the pellet was resuspended in 4.75 mL stopping buffer 2. The recalcification was performed by adding the listed volumes of calcium solutions and resuspension with a wide opening serological pipette allowing 4 min adaptation time between every single step.

Tab. 21: Recalcification steps

Volume	Calcium stock	Final concentration
25 µL CaCl$_2$	10 mM	62 µM CaCl$_2$
25 µL CaCl$_2$	10 mM	114 µM CaCl$_2$
50 µL CaCl$_2$	10 mM	191 µM CaCl$_2$
20 µL CaCl$_2$	100 mM	498 µM CaCl$_2$
30 µL CaCl$_2$	100 mM	960 µM CaCl$_2$

After recalcification, the cell suspension was allowed to sediment by gravity until the distinct formation of a cell pellet occurred, which was then resuspended in fresh pre-warmed adult mouse cardiomyocyte (AMCM) medium. Afterwards, the cardiomyocytes were plated as droplets on laminin-coated glass cover slips (Ø 18mm) in a 12-well plate or seeded in uncoated 6-well plates. The cells were incubated for 30 min at 37°C and 5% CO_2. Unattached cells were removed, and AMCM medium was added. The attached cardiomyocytes were cultured for 24 to 48 h at 37°C and 5% CO_2.

3.16.2 Depletion of cholesterol from the membrane of cardiomyocytes

Cholesterol was depleted by adding methyl-β-cyclodextrin (MβCD) to the culture medium of adult cardiomyocytes. For treatment, the culture medium was discarded and methyl-β-cyclodextrin containing medium with the concentrations listed in the table below (Tab. 22: Concentration methyl- β -cyclodextrin) was added to the cells.

Tab. 22: Concentration methyl- β -cyclodextrin

Cell type	Concentration
Adult mouse cardiomyocytes	0.3 mM

Adult mouse cardiomyocytes were treated directly after isolation and attachment by adding MβCD to the culture medium. The cardiomyocytes were cultured for 24 h in MβCD containing medium before they were used for further analyses.

3.16.3 Adenovirus transduction

Adult mouse cardiomyocytes were seeded as described before (refer to 3.16.1) and during the exchange of the culture medium after plating, adenovirus containing AMCM medium was added to the cells. The AMCMs were incubated for 36 - 48 h with a MOI of around 100-500. During the transduction, the culture was screened for GFP-positive cells via fluorescence microscopy. In addition, morphology, contractile behavior and viability of the cells were observed.

3.16.4 GPCR stimulation of adult mouse cardiomyocytes

In order to compare RhoA activation through stimulation of various G protein-coupled receptors, freshly isolated adult mouse ventricular cardiomyocytes were isolated from the three genotypes p63RhoGEF[wt/wt], p63RhoGEF[ko/ko] and p63RhoGEF[wt/ko] as described in chapter 3.16.1 at the same day. Alternatively, AMCM were isolated from untreated C57BL/6J mice or

after sham and TAC intervention. To reduce the influence of isolation-dependent effects on the RhoA activation, the cells were cultured for 24 h in AMCM medium at 37°C, 5% CO_2.

After 24 h of culture, the medium was discarded and 500 µL pre-warmed AMCM medium with the diluted receptor agonists, which are listed below, were added for 90 sec. Afterwards the cells were immediately fixed with 4% PFA as described in chapter 3.17.

Tab. 23: Stimulants and the corresponding concentrations for treatment of AMCM

Stimulant	Final concentration
Endotheline-1	50 nM
Angiotensin-II	100 nM
Phenylephrine	100 µM

3.17   Fixation and staining of cardiomyocytes for immunofluorescence

Adult mouse cardiomyocytes were fixed in 4% PFA in 1x DPBS either directly after seeding, after 24 h when treated or after 48 h when adenovirally transduced. For fixation, the respective medium was discarded and 500 µL 4% PFA in PBS (pH 7.4) were added for 6 min. After washing the cells twice with 1x DPBS, the cells were permeabilized and blocked with 500 µL blocking buffer 2 for 1 h. Adult cardiomyocytes all antibodies were diluted in blocking buffer 2, which contained FCS instead of Immunoblock. The incubation time with DAPI and FITC-phalloidin was reduced to 30 min. All further steps were performed as described above. Finally, cells were washed 3 times for 10 min with 1x DPBS at RT and mounted with a droplet of ProLong gold antifade mountant and stored light protected for 48 h. To stabilize the mounted samples, the cover slips were sealed with transparent nail polish.

3.18   Confocal microscopy

Confocal microscopy was used to image immunostained and fixed adult mouse cardiomyocytes. Imaging was performed with a confocal laser scanning microscope (LSM 710, Carl Zeiss, Jena). The objectives used for imaging are listed below.

Tab. 24: Objectives

Objective	Magnification
EC Plan-Neofluar	10x / 0.3 NA
EC Plan-Neofluar	20x / 0.5 NA
Plan-Apochromat	63x / 1.4 NA oil

To ensure the reproducibility of the imaging process, the proposed stepwise start of the system, including holding time, was strictly adhered to. Images were recorded using the software ZEN2009 provided by Zeiss and saved as ".lsm" files. For further analysis, images were processed using the ".tiff" file converted from the original ".lsm" file with the open access image processing software "Fiji" [ImageJ].

3.18.1 Confocal imaging and quantification of RhoA-GTP in AMCM

For detection of RhoA-GTP a primary anti-RhoA-GTP antibody, a secondary antibody coupled to AlexaFluor 568 (please also refer to 2.12) and objectives with 63x and 10x magnification were used. The 63x Plan-Apochromat oil objective was used for single cell imaging, the 10x EC Plan-Neofluar objective for overviews. AlexaFluor 568 was excited at a wavelength of 561 nm at 2-3% laser intensity. The detection range was set to 572-629 nm. The pinhole opening of 1 Airy unit resulted in an optical slice thickness of 800 nm. The detection gain was set to 500-700. The pixel size for imaging was set to 100 nm x 100 nm. For overviews the dye was excited with 5% of the 561 nm laser. The pinhole opening was set to 1 Airy unit which resulted in an optical thickness of 30 µm. All cells from one isolation were measured in the same imaging session. For that purpose, the determination of imaging settings depended on the samples with the highest intensities.

To determine the RhoA-GTP signal intensities, the open access image analysis software "Fiji" [imageJ 1.59] was used. All confocal single cell images of one imaging session were combined in one image stack. The cross-sectional area of each cell was selected using the "wand tool" with tolerance of 75 with the "legacy" mode and added to the "region of interest (ROI)" manager. To exclude signals from the sarcolemma, the selected ROI was reduced by 10 pixel with "enlarge selection"-10 pixels and added to the ROI manager. All selections of one stack were saved as "date of experiment_genotype_treatment".zip file. Using the "measurement" tool, area and raw integrated density were measured for all ROIs. The resulting data file was saved as "date of experiment_genotype_treatment-results".txt-file. Additionally, the fluorescence changes of the overview images were measured as described above using the "wand tool" and tolerance of 50-75. For that purpose, the images were combined as a stack.

The selection was added to the ROI manager and the area and the raw integrated density was measured. The selection and measurements were saved for further methods as described above. Thereby the cross-sectional area and the intensities were measured.

The measured intensities saved in the txt format were imported into Excel and used for calculation of the differences in active RhoA intensities at the sarcolemma, the cytosol and the overall intensity. Therefore, the sum of the intensities in the selection was divided by the area of the selection. By this method the intensities of the whole cell, at the sarcolemma and in the cytosol, were quantified.

3.18.2 Confocal imaging and analysis of immunostained samples

The imaging settings for each staining were adjusted at the beginning of each imaging session and were saved as reusable settings. The different imaging parameters for each dye are listed in the table below. Multi-color immunostains were imaged using a combination of the corresponding parameters in a frame sequential setting. If not stated differently, immunostains were imaged with a 63x Plan-Apochromat oil objective and a pixel size of 100 nm x 100 nm.

Tab. 25: Microscope settings for different excitation wavelength

Dye	Excitation wavelength	Laser power	Detection range	Optical slice thickness
DAPI	405 nm	1% - 2%	410 nm - 482 nm	500 nm
AlexaFluor 488	488 nm	2%	494 nm - 572 nm	600 nm
EGFP	488 nm	2%	494 nm - 572 nm	600 nm
AlexaFluor 568	561 nm	2% - 4%	563 nm - 600 nm	800 nm
AlexaFluor 633	633 nm	2% - 4%	638 nm - 747 nm	900 nm

To analyze the striation patterns of the proteins of interest, the "line"- tool was used. For that purpose, the line width was set to 20 pixel and a length of 10-12 µm was chosen. The line was placed in a 90° angle to the striation pattern (sarcomere), measured and visualized with the "plot profile" tool. The plot values were listed and saved as txt-file and further analyzed with Excel. Alternatively, the TTorg plugin of ImageJ was used [156]. SSPD was set to 27, the minimum spacing to 0.7 µm and the maximum spacing to 2 µm.

The localization of proteins in the sarcolemma and in the perinuclear region were measured with ImageJ. If possible the cells and nuclei were encircled with the wand tool or otherwise by hand. For analysis of the density at the sarcolemma, the cell ROI was reduced by 2 µm and

the total cell fluorescence as well as the residual cell fluorescence determined. The difference between both values reflects the fluorescence in the sarcolemmal region. For the perinuclear region the nucleus ROI was enlarged by 2.5 µm. The difference between the enlarged ROI and the nucleus ROI reflects the fluorescence in the perinuclear region. In most cases is the distribution of a protein given relative to the total detected signal in percent, in order to normalize for signal variations between different cells.

Co-localization analysis of proteins were performed with the Coloc2 plugin of ImageJ. Threshold regression was done with the help of the Costes algorithm. Thresholded Manders' correlation coefficients and the Pearson correlation coefficient were used for analysis.

To analyze the Golgi apparatus in AMCM the following steps were processed for every set of isolation. All staining from the same set were imaged as one set to guarantee the same microscope and laser condition. First, the channel with the Golgi apparatus images were duplicated, all images were combined to a single stack and saved as "tiff" file. Next, the images were processed by "subtract background" with a rolling ball radius of 5.0 pixels. The option "adjust-threshold" with a value 15-25 was used and the images were analyzed with "analyze particles". The pixel size was set to 2-infinity and "Outlines" were shown. The obtained data including particle count, size of particles and cross-sectional area of the cells were saved as txt-file.

Further analysis was performed with Excel and Prism.

3.18.3 Cell lysate preparation

Proteins were either isolated from freshly isolated or cultured AMCM. The freshly isolated or in liquid nitrogen deep-frozen cardiomyocytes from transgenic, TAC and sham operated mice were lysed by adding an adequate volume (100-300 µL) of lysis buffer to the cell pellet. After homogenization by pipetting and vortexing, the cell lysates were centrifuged for 10 min at 12000 x g and 4°C. The soluble protein fraction was transferred into a cold reaction tube and 4x loading buffer 1 was added. The pellet containing the insoluble protein fraction was directly dissolved in 1x loading buffer 2. All samples were denatured at 95°C for 5 min and stored at -20°C. Protein samples from cultured neonatal cardiomyocytes were prepared on ice by adding 200-300 µL GST-Fish buffer in each well of a 6-well plate. The lysed cells were collected with the help of a cell scraper and transferred into a 1.5 mL reaction tube. Homogenization was carried out by repetitive pipetting on ice. For storage, the samples were snap-frozen in liquid nitrogen or 4x loading buffer was added and the samples were heated 5 min at 95°C. After

cooling, samples were centrifuged and stored until usage at -20°C for short time period or at -80°C for long term storage.

3.18.4 Immunoblot analysis

Proteins were separated by discontinuous sodium dodecyl sulfate (SDS) polyacrylamide gel electrophoresis using 5% collecting and 8% to 15% separating polyacrylamide gels. The gel compositions are listed in the table (Tab. 26: SDS polyacrylamide gel composition.

Tab. 26: SDS polyacrylamide gel composition

Gel	Composition
5% SDS-polyacrylamide gel	10 mL ddH$_2$O
	1.7 mL 30% acrylamide rotiphorese gel solution
	1.25 mL 1 M Tris (pH 6.8, HCL)
	0.1 mL 10% SDS
	0.1 mL 10%APS
	10 µL TEMED
8% SDS-polyacrylamide gel	11.5 mL ddH$_2$O
	6,75 mL 30% acrylamide rotiphorese gel solution
	6.25 mL 1.5 M Tris (pH 6.8, HCL)
	0.25 mL 10% SDS
	0.25 mL 10%APS
	15 µL TEMED
15% SDS-polyacrylamide gel	5.75 mL ddH$_2$O
	12.5 mL 30% acrylamide rotiphorese gel solution
	6.25 mL 1.5 M Tris (pH 6.8, HCL)
	0.25 mL 10% SDS
	0.25 mL 10%APS
	10 µL TEMED

3.19   Statistics

All data are presented as mean ± standard error of the mean (SEM). Statistical significance was analyzed by unpaired T-test for two group comparison and one-way or two-way ANOVA followed by Bonferroni's post-hoc comparison for comparison of three or more groups (GraphPad, Prism 7.0). P-values less than 0.05 were classified as statistically significant.

4.   Results

4.1   Analysis of RhoA activation and localization in adult mouse cardiomyocytes

RhoA expression and activation had been mainly investigated in neonatal rat cardiomyocytes. However, in adult cardiomyocytes its expression, activation and localization are unknown. Therefore, adult cardiomyocytes were isolated from mouse hearts and confocal imaging of immunostainings of inactive and active RhoA was carried out. Active RhoA was detected with an antibody recognizing the conformation of GTP-bound, but not GDP-bound RhoA. Confocal imaging was performed from central regions of cardiomyocytes and at their surfaces (imaging planes are illustrated in Fig. 5 A). Representative images of RhoA-GTP and total RhoA are shown in Fig. 5 B. Active RhoA localization appears as a strong signal mainly at the sarcolemma and in thin transversally striated lines extending into the cell but not crossing the complete cell width. For total RhoA, a transversally striated pattern crossing the complete cell width could be observed indicating a sarcomeric localization. However, the total RhoA staining did not show a signal at the sarcolemma as compared to the active RhoA staining. Furthermore, co-stainings of RhoA-GTP with actin support its localization at the sarcomeric Z-line because RhoA-GTP striations show an overlay with actin signals. Co-staining of RhoA-GTP with myomesin-1 showed no intracellular overlap in the M-line region (Fig. 5 C). In addition to these results, a shift of the imaging plane towards the cardiomyocyte surface and co-stainings with actin, myomesin-1, dystrophin and caveolin-3 supported the sarcolemmal and sarcomeric localization of RhoA-GTP. At the cardiomyocyte surface, active RhoA co-localizes with actin filaments but not with myomesin-1 and dystrophin (Fig. 5 D). Caveolin-3 and active RhoA showed different localization patterns but seemed to minimally overlap in the costameric region. Interestingly, a 3D reconstruction of a z-stack imaging experiment additionally indicates that active RhoA can be found at intercalated discs of AMCM (Fig. 5 E).
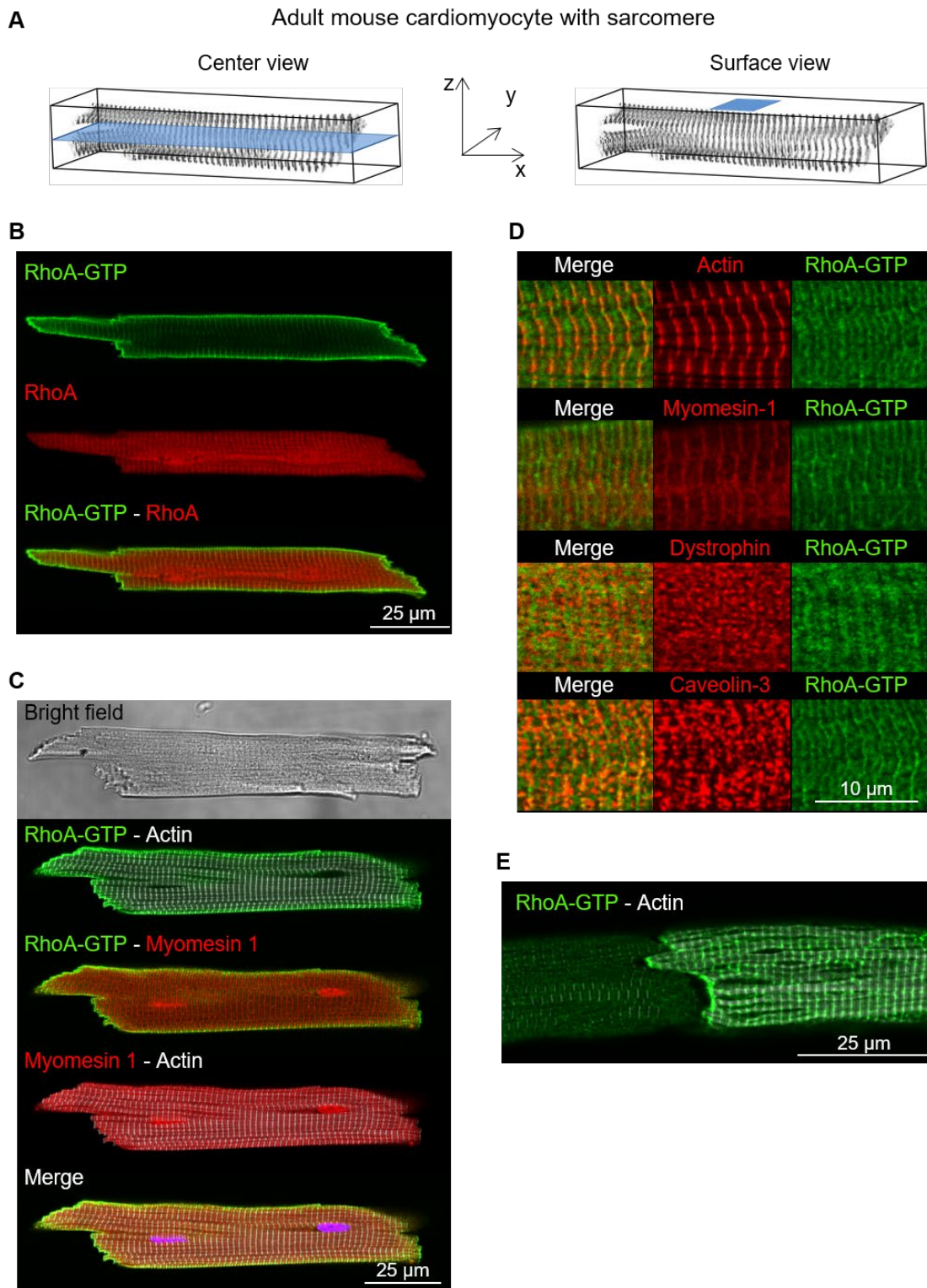
Fig. 5: Co-immunostaining of RhoA-GTP with sarcomeric and sarcolemma-associated proteins in WT-AMCM

Adult mouse cardiomyocytes (AMCM) were isolated by modified Langendorff perfusion and cultured on laminin-coated coverslips for 24 h at 37°C, 5% CO_2. **A)** Schematic illustration of the two different imaging planes center view (left) and surface view (right) is shown. **B)** Representative confocal center view images showing RhoA-GTP (green), total RhoA (red) and an overlay of both channels of WT-AMCM. Scale bar 25 µm. **C)** Representative confocal center

view images of co-immunostaining in a WT-AMCM are presented. Shown are the bright field image, RhoA-GTP (green), myomesin-1 (red), F-actin (grayscale) in different composites and as merge. Scale bar 25 µm. **D)** Magnification of confocal surface view images of Rho-GTP (green) with F-actin, myomesin-1, dystrophin or caveolin-3 (red) of WT-AMCM is shown. Scale bar 10 µm. **E)** 3D-reconstruction of confocal images (z-stack, 15 images, total depth 6.5 µm) was generated showing Rho-GTP (green) and F-actin (grayscale) co-staining of two WT-AMCM at the intercalated disc. Scale bar 25 µm.

To further investigate the co-localization of active RhoA and caveolin-3, a colocalization analysis was performed with the help of the ImageJ plugin Coloc2. The obtained Pearson's correlation coefficient suggested that the co-localization between active RhoA and caveolin-3 is in general low. However, the Manders' overlap coefficient M2, which reflects the correlation of caveolin-3 with active RhoA demonstrated that at least part of caveolin-3 possessed a similar localization as active RhoA, whereas only a minor proportion of active RhoA was found in close proximity to caveolin-3 demonstrated by the M1 coefficient (Fig. 6).
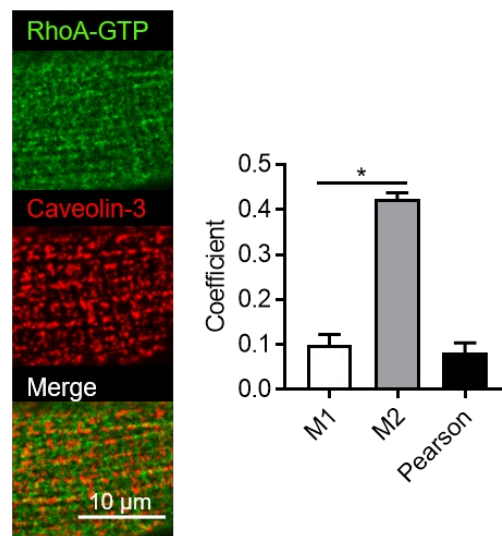
Fig. 6: Co-immunostaining of RhoA-GTP with caveolin-3

Adult mouse cardiomyocytes (AMCM) were isolated by modified Langendorff perfusion and cultured on laminin-coated coverslips for 24 h at 37°C, 5% CO_2. Immunofluorescence analysis of active RhoA and caveolin-3 was performed. Magnification of representative confocal surface view images of Rho-GTP (green) and caveolin-3 (red) of WT-AMCM are shown. Scale bar 10 µm. The colocalization of active RhoA and caveolin-3 was analyzed with the help of ImageJ's plugin Coloc2. M1 reflects the co-localization of active RhoA with caveolin-3 and M2 of caveolin-3 with active RhoA. Given are the means ± SEM, n=3, 14 cells, *$p < 0.05$.

Since most of the following experiments have been performed after cultivation of AMCM, it had to be excluded that cultivation influences the localization of RhoA and other proteins of interest. Therefore, the influence of 24 h compared to 1 h of cultivation on basal RhoA activity was analyzed next. By vertical line scans the amount of active RhoA was quantified (Fig. 7 A). Both, in freshly isolated AMCM and in AMCM cultured for 24 h, the strongest signal for active RhoA

was found at the sarcolemma as described above. Line scan analysis revealed that 24 h of cultivation led to a significant increase in active RhoA signal intensity and to a broadening of the signal at the sarcolemma indicating an increase of RhoA activity at the sarcolemma (Fig. 7 B). In summery the averaged signal intensity showed an increase of the signal width at the 50% peak RFU from 0.57 µm to 0.79 µm. This corresponds to a broadening of the RhoA signal intensity at the sarcolemma of 0.22 µm and an increased maximum signal intensity by 59% from averaged peak values of 82.44 RFU to 130.8 RFU.
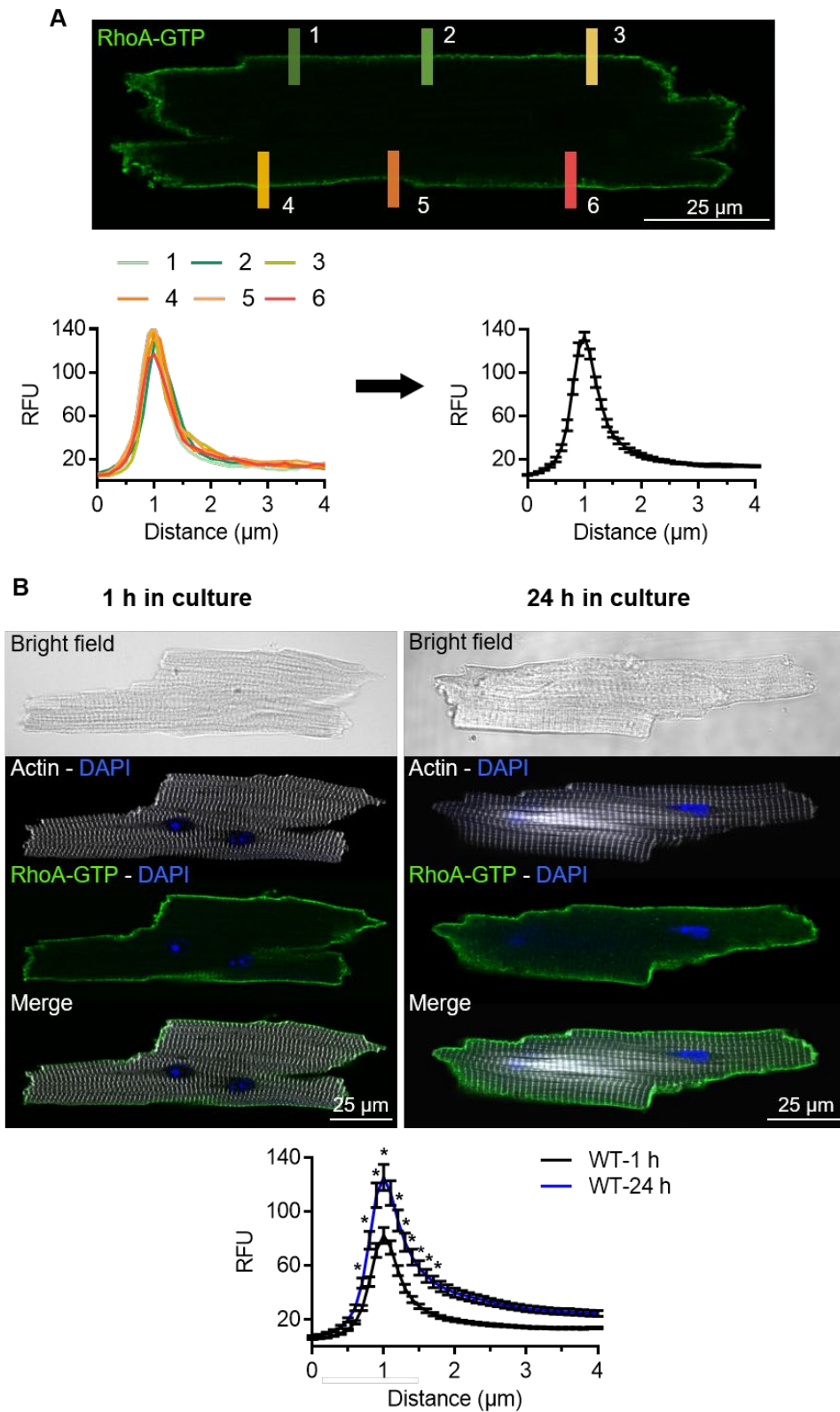
Fig. 7: Quantification of RhoA-GTP intensities at the sarcolemma in 1 h and 24 h cultured WT-AMCM.

A) Illustration of the vertical line scan measurement to quantify the relative fluorescence units (RFU) of RhoA-GTP at the sarcolemma in a confocal center view image. As depicted by the six bars, six independent regions were

measured per cell. Scale bar 25 µm. Graphical description of the measurement per cell. The left graph shows the six individual line scans obtained from one cell. Those individual line scans were averaged as shown on the right. Data are presented as means ± SEM of one cell. **B)** AMCM were isolated and cultured on laminin-coated coverslips for 1 h or 24 h at 37°C, 5% CO2. Comparison of representative center view confocal images showing bright field images, RhoA-GTP (green), F-actin (grayscale) and DAPI (blue) of WT-AMCM cultured for 1 h (left) or for 24 h (right) is presented together with the quantification of RhoA-GTP. Data are presented as mean RFU ± SEM, n=3 cell preparations, in total 15 cells cultured for 1 h, 20 cells cultured for 24 h; 6 line scans per cell, *p<0.05 tested by 2-way ANOVA. Scale bars 25 µm.

In neonatal rat cardiomyocytes it had been demonstrated that RhoA can be activated by G protein-coupled receptors belonging to the $G_{q/11}$ and $G_{12/13}$-coupled families. In order to study the activation of RhoA in AMCM, the cells were cultured for 24 h and then treated with 100 µM phenylephrine and 50 nM endothelin-1 (PE/ET-1) for 90 sec. For control, cells were treated with BSA after 24 h of cultivation. After fixation, confocal imaging of RhoA-GTP and actin was performed. Signals were imaged in different imaging planes, coming from the center to the surface, and line scans in parallel to the main cell axis were analyzed (Fig. 8 A).

For active RhoA, changes in signal intensities and frequencies were observed after stimulation with PE/ET-1. Those changes were most prominent at the cell surface (Fig. 8 B). Overlays of the line profiles of actin and RhoA-GTP showed especially increased signal intensities for RhoA in the costamere region at the sarcolemma. Overall, the striated pattern of the active RhoA distribution became more pronounced. Periodicity of RhoA-GTP signals was analyzed in the different treatment groups at the cell center and at its surface (Fig. 8 B, C). The regular extra RhoA-GTP peak at the cell surface led to a decrease of peak-to-peak distances from ~1.8 µm (center) to ~0.9 µm. To exclude cell contraction as a source for the observed changes after PE/ET-1-treatment, vertical line scan analyses of actin and myomesin-1 were performed. Both showed a regular pattern and the peak-to-peak distances of actin was ~1.8 µm under treated and control conditions (Fig. 8 D). This result indicates that the described changes in active RhoA intensity and distribution was not based on PE/ET-1-induced cell contraction.
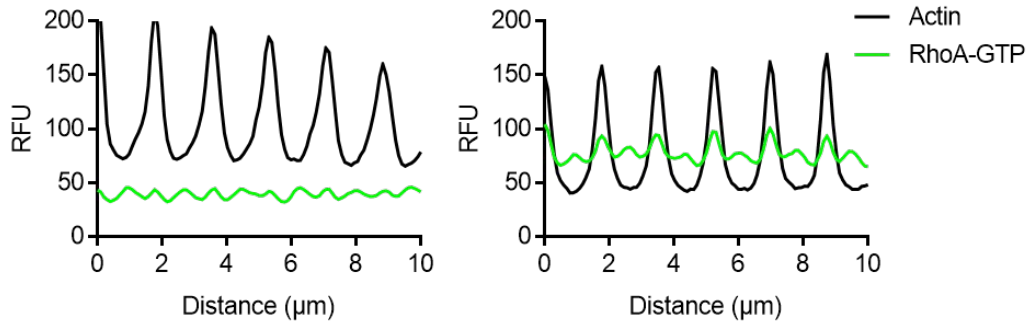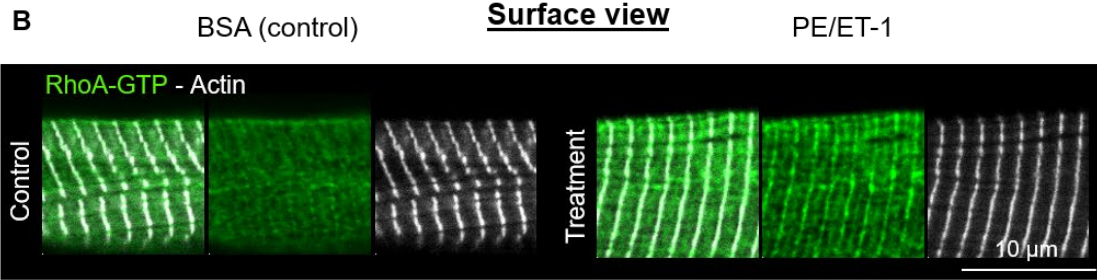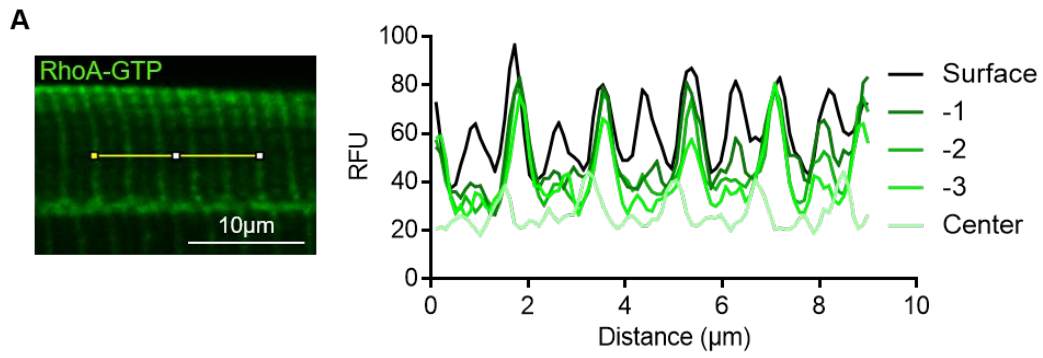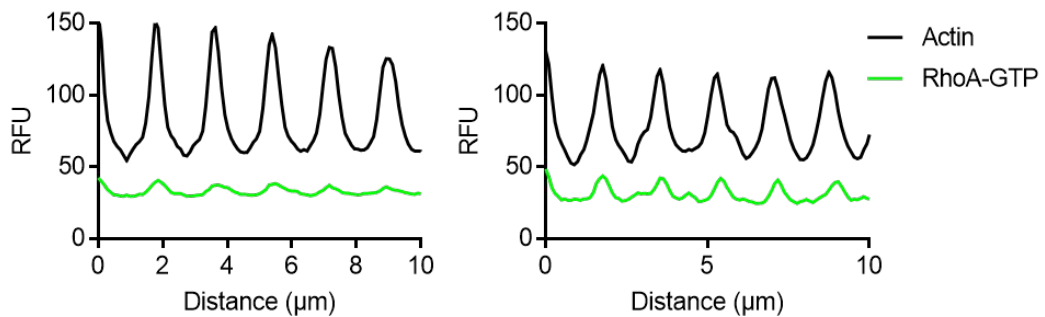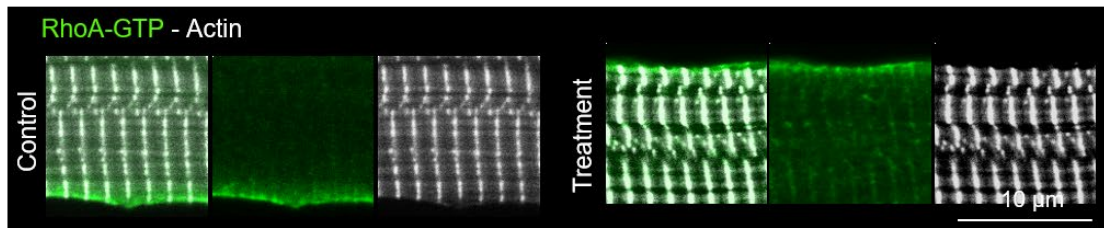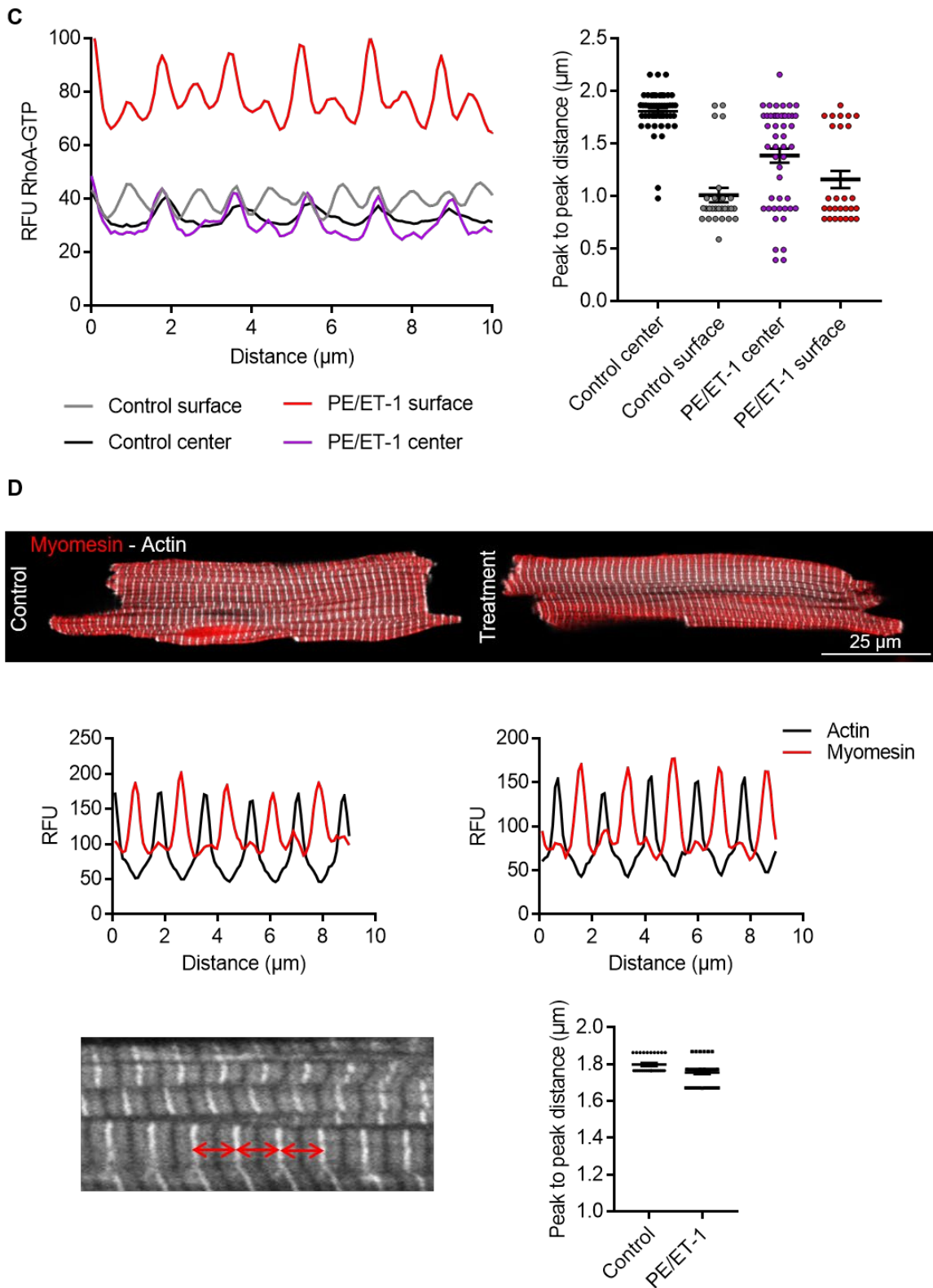
Fig. 8: Analysis of RhoA-GTP localization and intensity in WT-AMCM after treatment with PE/ET-1.

Adult mouse cardiomyocytes (AMCM) were cultured for 24 h and treated either with BSA or with 100 µM phenylephrine and 50 nM endothelin-1 (PE/ET-1) for 90 sec. **A)** Magnification of a confocal center view image showing RhoA-GTP is presented (left). The vertical line (yellow) illustrates where RhoA-GTP localization was

analyzed (left). The profile of RhoA-GTP intensities in different imaging depths in a z-stack (every third of 15 images, total depth 6.5 µm) were analyzed (right). The graph depicts scan lines from center (light green) to the surface (black) of an AMCM treated with PE/ET-1. **B)** Representative magnifications of confocal images of AMCM stained for RhoA-GTP and F-actin at the surface (top) and center (bottom) with the corresponding line profiles is shown. Scale bar 10 µm. **C)** Combination of the different RhoA-GTP line profiles from (**B**) illustrating the changes in pattern in different views for PE/ET-1-treated and BSA condition (left) is presented. Extraction and quantification of the peak-to-peak distances from RhoA-GTP line profiles was performed (right). Given are the values of one treatment experiment. **D)** Representative confocal center view images (top) of AMCM cultured for 24 h, treated with BSA (left) or PE/ET-1 (right) and stained for myomesin-1 (red) and F-actin (grayscale) are shown. Representative line profiles (middle) of F-actin and myomesin-1 are shown. Magnification of F-actin staining demonstrating the sarcomere pattern (bottom left) is shown. Representative quantification (bottom right) of the Z-disc peak-to-peak distance in control and treated AMCM of one treatment experiment is given. Scale bar 25 µm.

To confirm the PE/ET-1-induced activation of RhoA in isolated AMCM detected by immunofluorescence analysis, a G-Lisa assay was performed. This biochemical assay uses a pre-coated surface, which selectively binds the active forms of RhoA, RhoB or RhoC present in cell lysates, and a specific RhoA antibody to detect bound RhoA. For normalization an immunoblot of the lysates was performed in addition to quantify total RhoA levels. Comparable to the immunofluorescence analysis, the G-Lisa experiment demonstrated that RhoA activity was significantly increased in AMCM after PE/ET-1 treatment (Fig. 9 A).

Further analysis of the obtained cell lysates and of the residual insoluble fraction by immunoblot revealed that most of the RhoA protein resides in the insoluble fraction. This fraction contains in addition sarcomeric proteins as demonstrated by α-actinin (Fig. 9 B). This finding supports the above described localization of total RhoA indicating that most of the protein is associated to the sarcomere and only the minor fraction of active RhoA resides at the sarcolemma.

To further confirm, that the treatment of AMCM with PE/ET-1 induced the activation of heterotrimeric $G_{q/11}$ protein signaling, the phosphorylation of the PKC substrates Ezrin/ Radixin/ Moesin (ERM) and of ERK1/2 after PE/ET-1 treatment was studied by immunoblotting (Fig. 9 C and 9 D). The ratio of phosphorylated ERM to total ERM significantly increased ~3-fold after treatment. The ratio of phosphorylated ERK1/2 to total ERK1/2 significantly increased ~2-fold after PE/ET-1 treatment.
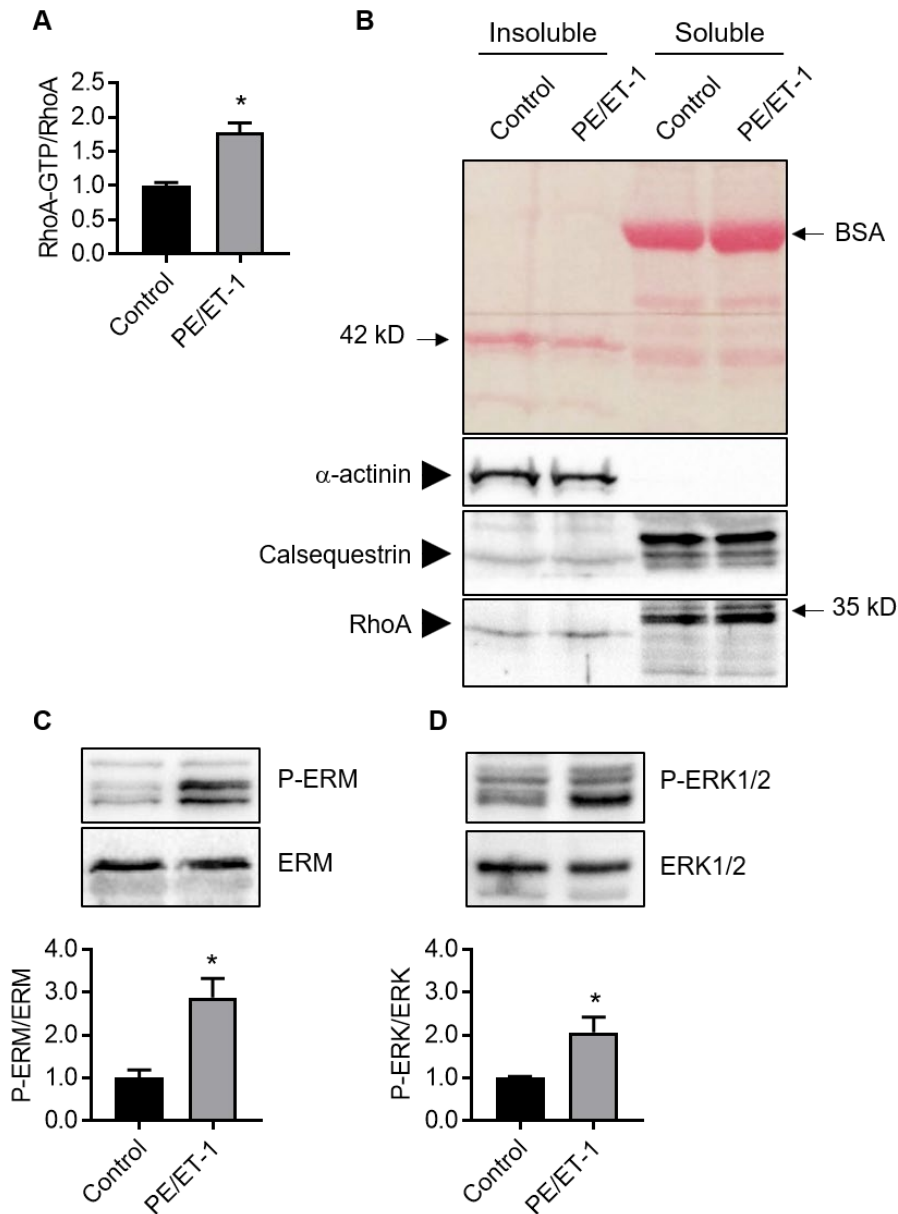
Fig. 9: Quantification of PE/ET-1-induced changes in RhoA, ERM and ERK1/2 activity in WT-AMCM.

Adult mouse cardiomyocytes (AMCM) were isolated and cultured for 24 h. Treatment with 100 µM phenylephrine and 50 nM endothelin-1 (PE/ET-1) was performed for 90 sec. **A)** RhoA-GTP was measured in lysates by G-Lisa activity assay kit. Total RhoA was determined by immunoblot in G-Lisa lysates. Given is the ratio of RhoA-GTP and total RhoA relative to control. Data are presented as means ± SEM. n=4 control, n=6 treated, *p<0.05 vs. control assessed by unpaired t-test. **B)** Treated and untreated AMCM were lysed with G-Lisa lysis buffer and separated into soluble and insoluble fractions by centrifugation. Ponceau-S staining (top) of representative immunoblots (bottom) of α-actinin, calsequestrin and RhoA is shown. Representative immunoblots of **C)** phosphorylated ERM and total ERM (left), **D)** phosphorylated ERK and total ERK (right) in control and PE/ET-1 treated AMCM are shown. For quantification (bottom), the signals of the phosphorylated proteins were normalized to the respective total protein signals. Data are presented as means ± SEM relative to controls. n=3, *p<0.05 vs. control assessed by unpaired t-test.

So far, both GPCR agonists ET-1 and PE had been used as a combined treatment for the AMCM. For discrimination of their individual effects on the localization of active RhoA, the cells were individually treated and the active RhoA pattern was analyzed at the cell surface with the help of the ImageJ plugin TTorg [156]. Both ligands induced a more pronounced striated pattern on the cell surface of the AMCM compared to control (Fig. 10 A). The analysis demonstrated that the fraction of cells having the dominant localization of active RhoA in the costamere region (pattern 1.8 µm) increased after application of ET-1 and PE (Fig. 10 B). Moreover, the power of the general periodic pattern (0.9 µm) increased after ET-1 and PE treatment and of the dominant 1.8 µm pattern after ET-1 application (Fig. 10 C).
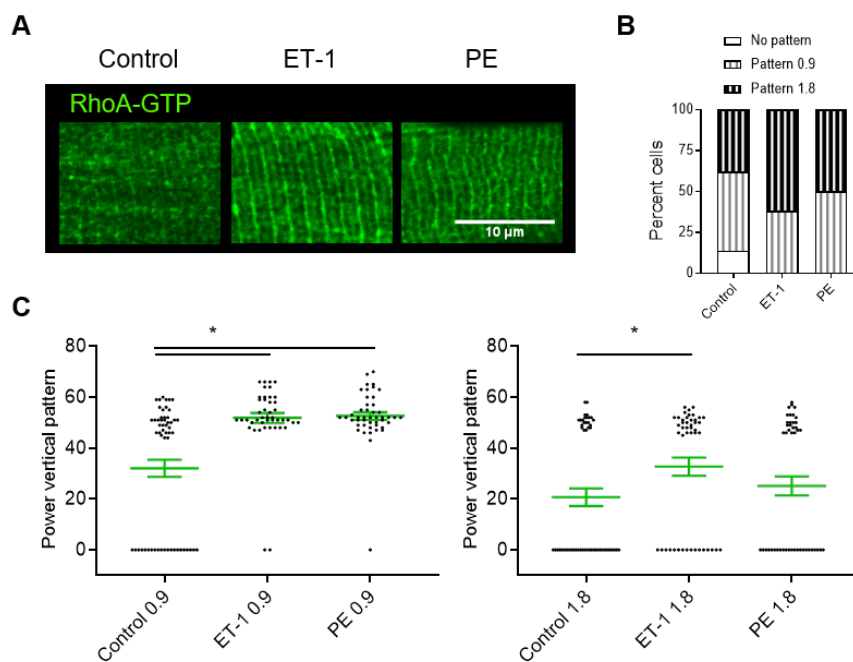
Fig. 10: Analysis of RhoA-GTP localization in WT-AMCM after individual treatment with PE and ET-1.

Adult mouse cardiomyocytes (AMCM) were cultured for 24 h and treated either with BSA, with 50 nM endothelin-1 (ET-1) or with 100 µM phenylephrine (PE) for 90 sec. Immunofluorescence analysis of active RhoA was performed. **A)** Magnification of confocal surface view images showing RhoA-GTP are presented. Scale bar 10 µm **B)** A pattern analysis with the help of the ImageJ plugin TTorg was performed. The fractions of cells showing no pattern, a dominant pattern with a striation regularity of around 0.9 µm or 1.8 µm are presented. **C)** The power of the vertical 0.9 µm (left) and 1.8 µm (right) pattern is given. In total 20 to 30 cells were analyzed from 3 independent experiments.

Taken together, active RhoA mainly resides in the sarcolemma of adult cardiomyocytes. The fraction of active RhoA compared to total RhoA, which showed a preferential sarcomeric localization, can be considered as rather low based on the immunofluorescence analysis and the biochemical fractionation. In response to the GPCR ligands ET-1 and PE active RhoA

increases and translocates to the sarcolemma towards the costameric region as demonstrated by actin co-staining.

4.2 Analysis of RhoA activation and localization in adult mouse cardiomyocytes after transverse aortic constriction

RhoA has been shown to be fast and permanently activated in mouse hearts after TAC [114]. However, whether this includes its activation in cardiomyocytes was not demonstrated. Moreover, it is not clear how RhoA is activated in the diseased heart. Therefore, transverse aortic constriction experiments with C57BL/6J mice were performed (Fig. 11 A). For the control group, a sham surgery was performed. Sham mice underwent the same surgical procedure, only without the final constriction of the aorta. Three days after the interventions, pressure gradients in the aorta were determined by Doppler echocardiography. Compared to control mice (sham) with an average gradient of ~8 mmHg, TAC mice had an average pressure gradient of ~70 mmHg (Fig. 11 B). In addition, an echocardiographic phenotyping was performed before and 4 weeks after the intervention. Four weeks after TAC, the development of hypertrophy was observed reflected by a significant increase of the left ventricular weight to body weight ratio (LVW/BW) from 4 mg/g to 8 mg/g in the TAC. No changes were found in the sham group (Fig. 11 C). Furthermore, the ejection fraction (EF) was significantly reduced from ~50% to ~30% after TAC (Fig. 11 D) and a significant dilation of the left ventricle had taken place as demonstrated by an increase of the diastolic volume from 100 µL to 150 µL (Fig. 11 E). Taken together, the transition of compensatory heart hypertrophy to heart failure had taken place 4 weeks after TAC.
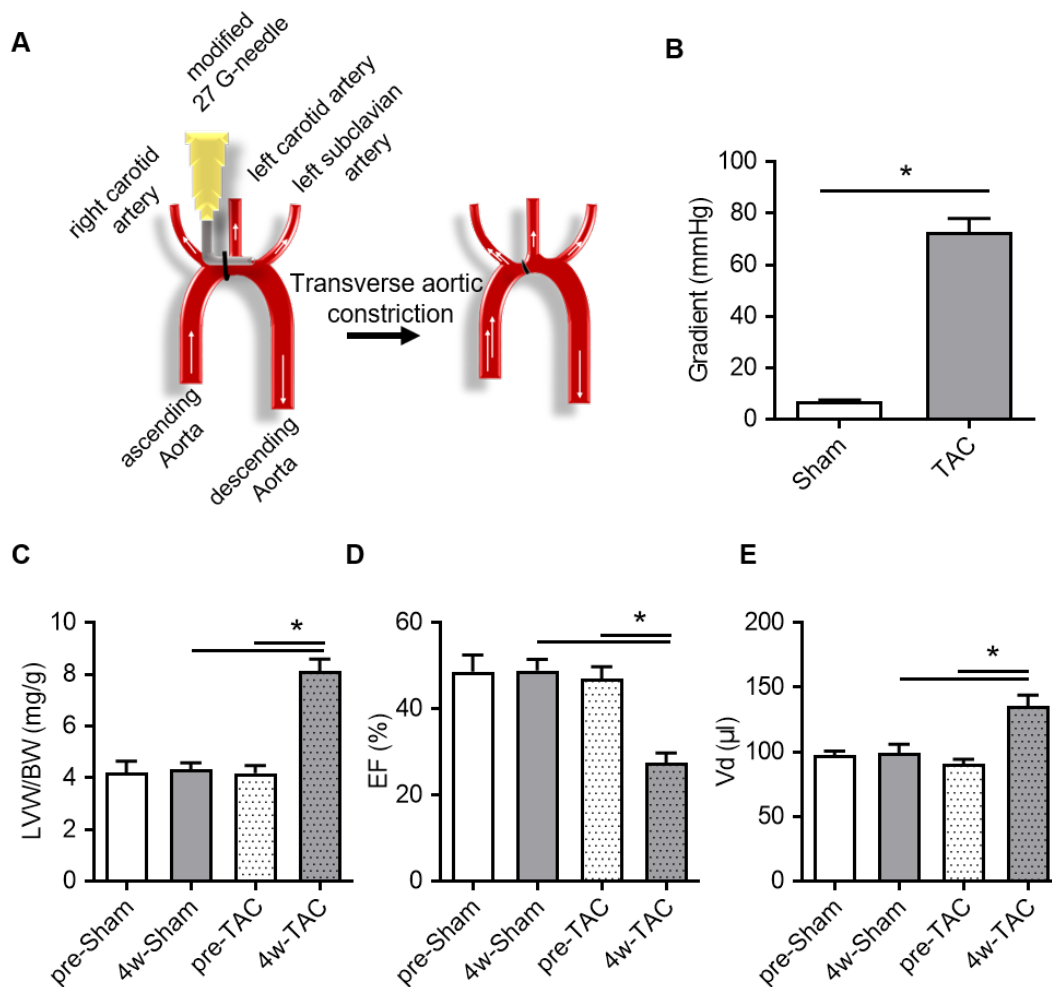
Fig. 11: Analysis of the heart function in response to transverse aortic constriction.

Nine week old male mice subjected to transverse aortic constriction (TAC) or sham intervention were characterized by echocardiography before and 4 weeks after the intervention. **A)** Schematic illustration of a TAC intervention modified from Luo *et al.*, 2015 is presented [157]. **B)** Pressure gradients in the transverse aorta were measured by Doppler echocardiography. Values are shown as means ± SEM, n=5 Sham, n=7 TAC, *p<0.05 assessed by unpaired t-test. **C)** The left ventricular weight to body weight ratio (LVW/BW), **D)** ejection fraction (EF) and **E)** diastolic volume (Vd) were determined by echocardiography. Values are shown as means ± SEM, n=5 Sham, n=7 TAC, *p<0.05 assessed by 1 way ANOVA.

Subsequently, the morphology of isolated cardiomyocytes in cell culture was analyzed. For that purpose, ventricular myocytes from TAC and sham mice were isolated and either directly fixed or cultured for 24 h before fixation. The isolated and fixed cells were stained for F-actin and imaging was performed with a low magnification (10x) to obtain representative overview images (Fig. 12). In those overview images, mean cell area, depth, length and width were determined. Determination of the cell area revealed a significant increase in TAC-AMCM compared to sham-AMCM from 2800 µm^2 to 3800 µm^2 directly after the isolation. This change was slightly reduced to 2500 µm^2 in control and 3000 µm^2 in TAC-AMCM after 24 h in culture.

Consistent with these results, significant increases in mean cell depth, length and width were detected for directly fixed and 24 h cultured cells 4 weeks after TAC. As observed for the cell area, also cell depth and length were slightly smaller after 24 h in culture compared to directly fixed cells. In contrast to these findings, the cells showed a significant increase in cell width after 24 h in culture. In summary, it could be shown that the hypertrophic phenotype of isolated cardiomyocytes after TAC was preserved during the first 24 h in culture.
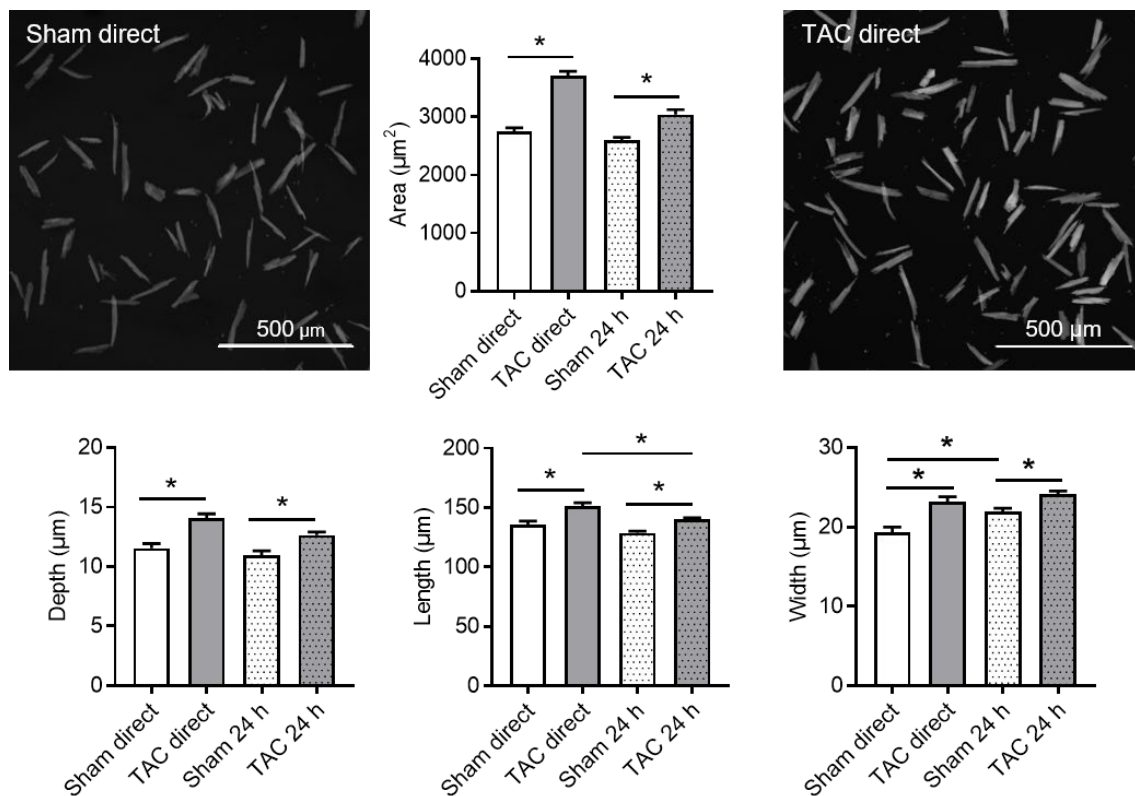
Fig. 12: Quantification of morphological changes of AMCM after transverse aortic constriction.
Adult mouse cardiomyocytes (AMCM) were isolated from animals 4 weeks after sham or transverse aortic constriction (TAC) intervention and seeded on laminin-coated coverslips. The cells were either directly fixed after 1 h (direct) or cultured for further 24 h. F-actin was stained with FITC-labeled phalloidin. Representative overview images (10x magnification) of directly fixed sham (left) and TAC (right) AMCM are shown. Analyses of AMCM areas (middle, top row), cell depths (left, bottom row), cell lengths (middle, bottom row) and cell widths (right, bottom row) after direct fixation or 24 h culture are depicted. Values are presented as means ± SEM, n=5 Control, n=7 TAC, *$p < 0.05$ assessed by 1 way ANOVA.

In addition to the analysis of the cell morphology, sarcomere lengths were measured in the sham- and TAC-AMCM. After fixation and permeabilization cells were stained with FITC-labeled phalloidin and DAPI to visualize the sarcomeric Z-lines and the nuclei. After single cell confocal imaging, sarcomeric lengths were measured in line scans by peak-to-peak analysis of the actin signals. Isolated cardiomyocytes from all groups (directly fixed, cultured for 24 h, sham and TAC) showed consistent sarcomere lengths of ~1.8 µm. These results indicate that

neither the TAC intervention nor fixation or cultivation had an influence on sarcomere length and did not lead to abnormal cellular contraction (Fig. 13).
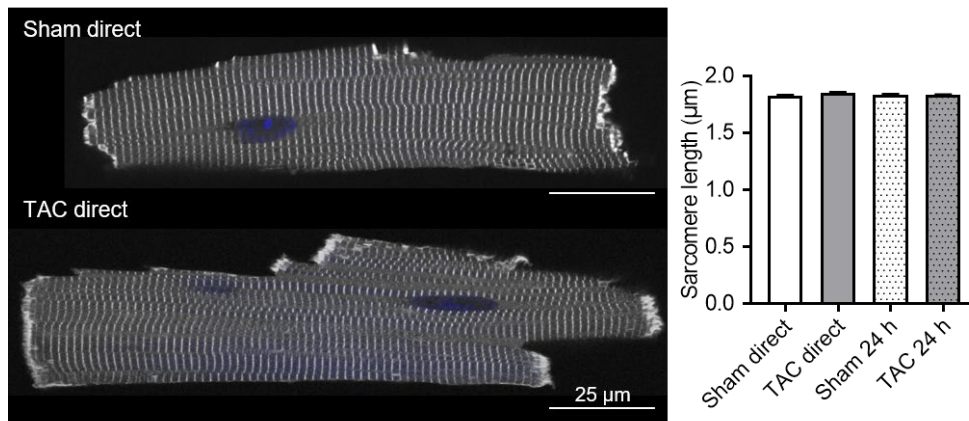
Fig. 13: Analysis of sarcomere length in AMCM after transverse aortic constriction.
Adult mouse cardiomyocytes (AMCM) were isolated from animals 4 weeks after sham or transverse aortic constriction (TAC) and seeded on laminin-coated coverslips. The cells were either directly fixed after 1 h (direct) or cultured for further 24 h. F-actin was stained with FITC-labeled phalloidin and nuclei with DAPI. Representative confocal center view images of F-actin (grayscale) and nuclei (blue) staining are shown. Scale bar: 50 µm. Sarcomere lengths were determined by line scan and peak-to-peak analysis of the Z-disc. Values are presented as means ± SEM, n=5 Control, n=7 TAC.

As shown in Fig. 7, active RhoA localized predominately at the sarcolemma and to a lesser extent at the sarcomere in WT-AMCM. As pressure overload had been shown to perturb membrane organization in cardiomyocytes, active RhoA localization was studied in directly fixed sham- and TAC-AMCM. In addition, F-actin, myomesin-1, dystrophin and caveolin-3 were detected. By confocal microscopy, single cell imaging was performed. Initially, RhoA-GTP / F actin double stains were imaged (Fig. 14 A, 14 C). In comparison to sham-AMCM, a clear disorganization of the periodic active RhoA at the sarcolemma was found in TAC-AMCM by surface imaging. TTorg analysis revealed that more cells were present showing no regular active RhoA pattern at the cell surface (Fig. 14 B). Similar, the membrane-associated myomesin-1, dystrophin and caveolin-3 showed less organized distributions at the sarcolemma in TAC-AMCM (Fig. 14 C). These results indicate that the organizational changes of the sarcolemma, which occur during the process of cardiac remodeling, influences also the localization of active RhoA.
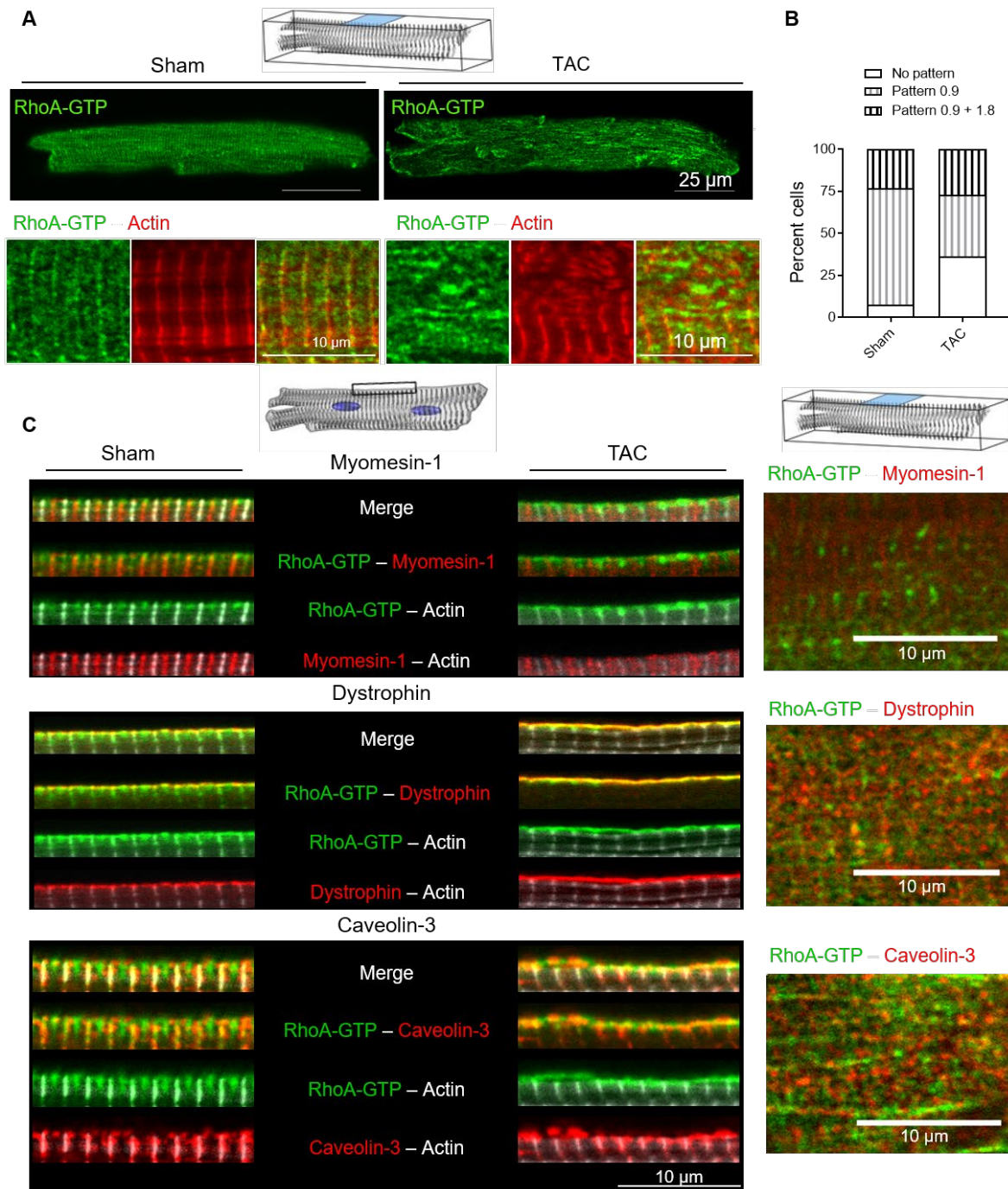
Fig. 14: Analysis of RhoA-GTP distribution at the sarcolemma of AMCM after transverse aortic constriction.

Adult mouse cardiomyocytes (AMCM) were isolated from animals 4 weeks after sham or transverse aortic constriction (TAC) intervention and seeded on laminin-coated coverslips. The cells were directly fixed and immunofluorescence analyses for the indicated proteins were performed. In addition, F-actin was stained with FITC-labelled phalloidin. **A)** Representative confocal surface view images for RhoA-GTP (green) and F-actin (red) are shown. Scale bar 25 μm. Magnification of RhoA-GTP (green), F-actin (red) and merges (from left to right) of the surface region of directly fixed sham (left) and TAC (right) AMCM are given below. Scale bar 10 μm. **B)** TTorg analysis of surface view images was performed. In total 10 to 15 cells of 3 independent experiments were analyzed. **C)** Magnifications of confocal center (left) and surface (right) view images of the sarcolemma of sham- and TAC-

AMCM are depicted. Immunostaining was performed for RhoA-GTP (green) in combination with myomesin-1 (red), dystrophin (red) and caveolin-3 (red). F-actin (grayscale) is shown in addition in the center view images. Scale bar 10 μm.

Having shown an altered localization of active RhoA in AMCM after TAC, the next aim was to analyze the activation of RhoA by different GPCR agonists in AMCM isolated from sham and TAC hearts. For that purpose, the isolated cells were cultured for 24 h and then treated with the indicated receptor agonist for 90 sec. BSA was used as a control treatment. After immediate fixation, active RhoA was detected by immunofluorescence analysis. To investigate potential changes confocal overview (10x magnification) and single cell (63x magnification) images were generated. Figure 15 A shows the quantification of RhoA-GTP intensities in overview images. Those values represent the amount of active RhoA in the whole cell and not from a single imaging plane as it is shown and quantified in Fig. 15 B, 15 C and 15 D.

In sham-AMCM, RhoA could be activated by treatment with ET-1, PE and AngII. Here, the highest and most significant responses were observed after application of PE and AngII. In TAC cardiomyocytes, RhoA was no longer activated upon the addition of the three agonists. Interestingly, ET-1 and PE seemed to have an inhibitory effect on RhoA (Fig. 15 A). Importantly, the basal RhoA activity in TAC-AMCM was significantly higher compared to the basal RhoA activity in sham-AMCM.

By quantification of single cell image with a 63x magnification, the same pattern of RhoA activation after application of ET-1, PE or AngII (Fig. 15 B, C) was observed in sham cardiomyocytes compared to total cell imaging (Fig. 15 A). Both at the sarcolemma and in the cytosol, active RhoA showed the highest increase in response to stimulation with PE or AngII. However, results obtained for TAC-AMCM from single cell images (63x) compared to overview images (10x) differed. The high basal RhoA activity measured in overview images could not be seen in single cell images as well as the inhibitory effect of ET-1 and PE on RhoA activity in TAC-AMCM was less pronounced. To exclude that these changes resulted from differences in the sarcolemmal width, vertical line scans were performed of RhoA-GTP images with 63x magnification. In TAC and sham cardiomyocytes, the sarcolemma was found to be ~1.4 μm wide (Fig. 15 D).

The most important difference between the two different imaging modalities was that RhoA-GTP intensities in overview images originate from the complete cell depth and include the sarcolemma at the top and at the bottom of a cardiomyocyte. In contrast to that, single cell images obtained with a magnification of 63x and a confocal pinhole adjusted to one airy unit, only represent a single imaging plane with a depth of ~800 nm and do not include signals from

top and bottom sarcolemma. Thus, to explain the higher basal RhoA activity observed in overview images of TAC-AMCM, volumes of TAC and sham cardiomyocytes were calculated based on the mean morphological values given in Fig. 12. The averaged sham-AMCM had a volume of 23,372 µm^3, averaged TAC-AMCM were significantly larger and had a volume of 34,592 µm^3. Taking those values into account, values for RhoA-GTP intensities in 63x single cell images were extrapolated and compared to the intensities obtained from overview (10x) images (Fig. 15 E). Those calculations revealed that the significant basal increase of RhoA activity in TAC-AMCM could also be reproduced in single cell images.
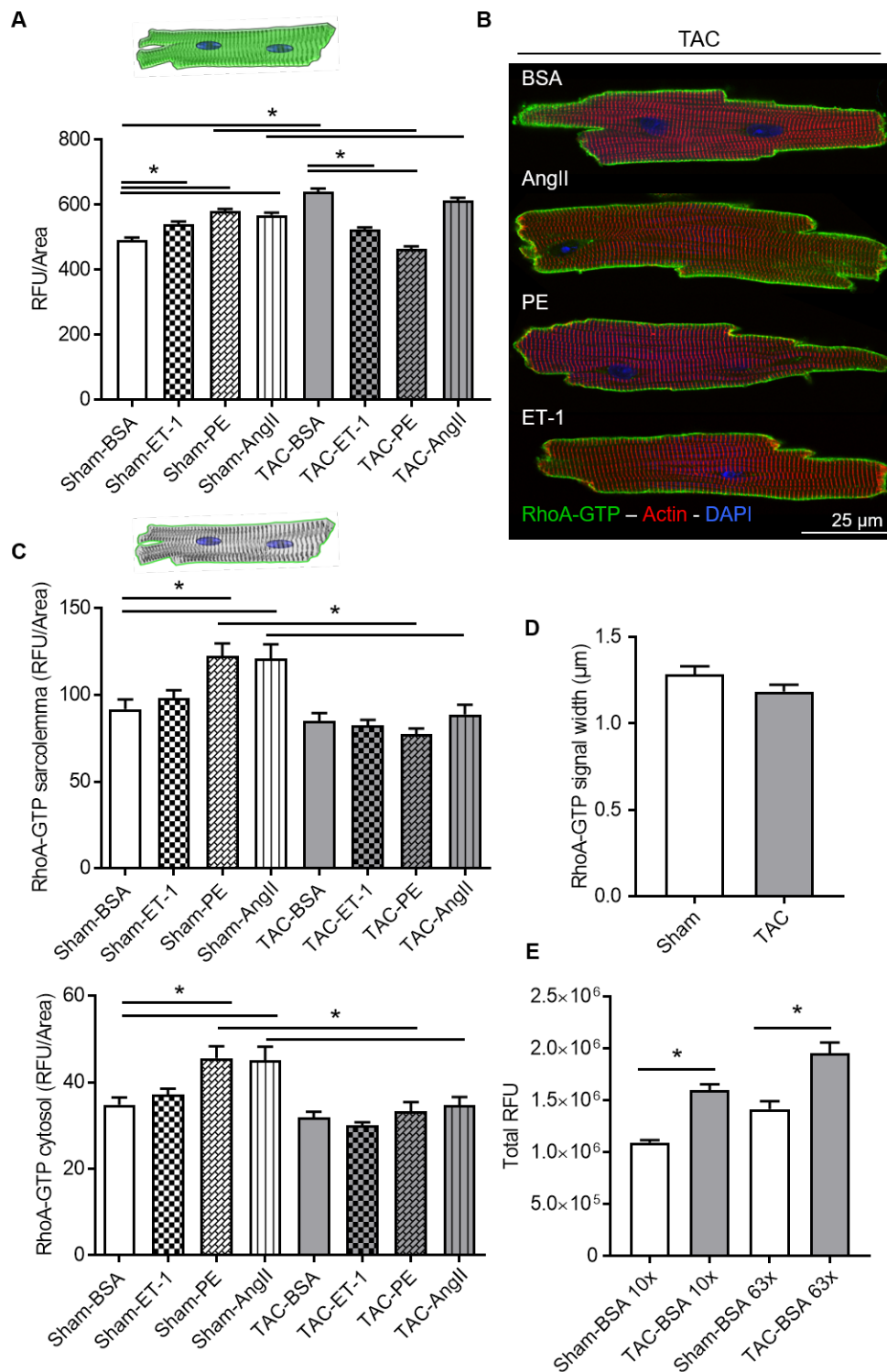
Fig. 15: Analysis of GPCR-dependent RhoA activation in isolated AMCM after transverse aortic constriction.

Adult mouse cardiomyocytes (AMCM) were isolated from animals 4 weeks after sham or transverse aortic constriction (TAC) intervention and seeded on laminin-coated coverslips. The cells were cultured for 24 h and then treated with 100 µM phenylephrine (PE), 50 nM endothelin-1 (ET-1) or 100 nM angiotensin II (AngII) for 90 sec. For control BSA was added to the cells. Afterwards the cells were directly fixed and immunofluorescence analysis for RhoA-GTP with subsequent confocal imaging was performed. **A)** Total RhoA-GTP fluorescence from confocal

overview images (10x magnification) was quantified and is given as means ± SEM normalized by the area, n=3 with >200 cells per group,*p<0.05. **B)** Representative confocal center view images of RhoA-GTP (green) and additionally stained F-actin (red) and cell nuclei (blue) in treated AMCM are shown. Scale bar 25 μm. **C)** RhoA-GTP fluorescence from confocal center view images (63x magnification) was quantified and with help of the wand tool of ImageJ the fluorescence of the sarcolemma and the intracellular region was calculated. The intensity values are given as means ± SEM normalized by the area, n=3 with ≥ 23 cell per group,*p<0.05. **D)** The width of the RhoA-GTP signal was analyzed by line scans. Shown are means ± SEM. **E)** The fluorescence intensities shown in A) and C) of the sham and TAC controls were used to calculate the total relative fluorescent units with help of the calculated cell volumes. Shown are the means ± SEM, n=3, *p<0.05.

Taken together, the basal RhoA activity is increased in TAC compared to sham-AMCM. Additionally, ET-1 and PE seem to have an unexpected inhibitory effect on RhoA in TAC-AMCM.

Different image analysis approaches revealed an increase of active RhoA after TAC and an altered response to different GPCR agonists. For further characterization, the amount of total RhoA in isolated AMCM was determined by immunoblot analysis. In addition, the expression of α-actinin and caveolin-3 were analyzed. Calsequestrin expression was used to normalize the individual values. Representative immunoblots for lysates of sham- and TAC-AMCM and the Ponceau S-stained membrane are shown in Fig. 16 A. Quantification of the detected proteins revealed a slight, however not significant, increase in α-actinin after TAC. The expression of RhoA was significantly decreased after TAC to 59% of the protein amount found in sham-AMCM lysate. This was accompanied by a significant decrease of caveolin-3 to 57% in AMCM after TAC (Fig. 16 B).
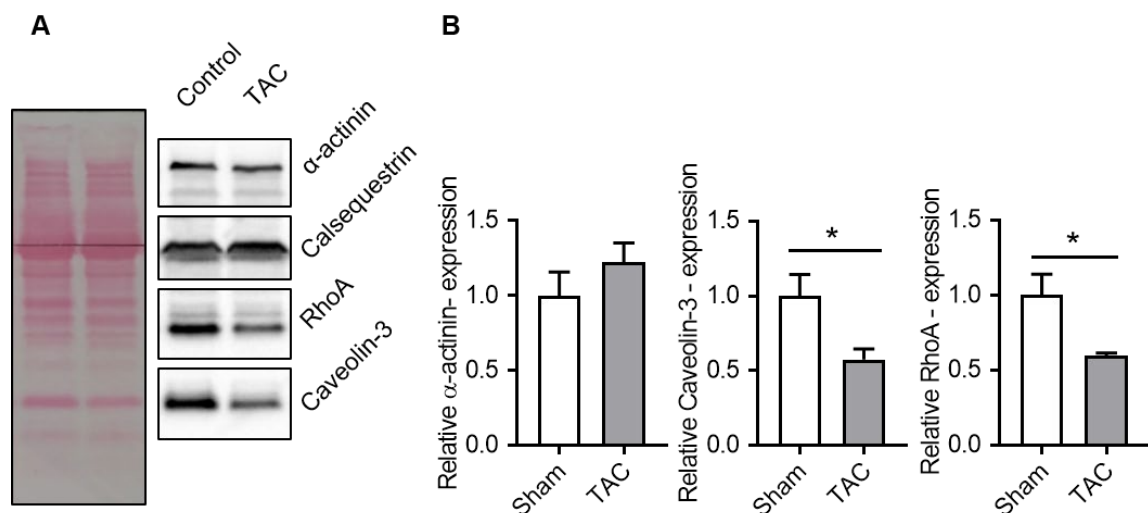
**Fig. 16: Analysis of RhoA expression in isolated AMCM after transverse aortic constriction.**
Adult mouse cardiomyocytes (AMCM) were isolated from animals 4 weeks after sham or transverse aortic constriction (TAC). The cells were directly lysed after isolation and immunoblot analysis was performed. **A)**

Representative Ponceau S staining and the corresponding immunoblots of α-actinin, calsequestrin, total RhoA, and caveolin-3 are shown. **B)** The quantification of the expression levels of α-actinin (left), total RhoA (middle) and caveolin-3 normalized to calsequestrin are given as means ± SEM relative to sham, n=3-4 per group, *p< 0.05.

4.3 Analysis of RhoA activation in adult mouse cardiomyocytes after cholesterol depletion

The observed down-regulation of caveolin-3 and the high basal RhoA activity after TAC implied that changes in the sarcolemmal structure could be responsible for alterations in RhoA signaling. To prove this hypothesis, AMCM were treated with 0.3 mM methyl-β-cyclodextrin (MβCD) for 24 h to deplete the cholesterol out of the membranes and thereby to disrupt lipid rafts and caveolae. Afterwards, the cells were treated with 50 nM ET-1 for 90, immediately fixed and active RhoA was detected by immunofluorescence.

The effect of the MβCD treatment on the structure of the membrane and on the distribution of the caveolae protein caveolin-3 is shown in Fig. 17 A. Quantification of the respective images revealed that in response to cholesterol-depletion, the prominent perinuclear caveolin-3 pool in the perinuclear region of cultured cells was redistributed towards the tubular membrane system, but no changes were detectable with respect to the pattern regularity and fluorescence intensity (Fig. 17 B). Fig. 17 C shows representative confocal images of active RhoA in either MβCD- or control-AMCM without treatment or after ET-1 application. Under control conditions, ET-1 treatment leads to brighter RhoA-GTP signals especially at the sarcolemma as shown before. MβCD-treated AMCM already showed brighter RhoA-GTP signals in the absence of ET-1 indicating a higher basal activity induced by membrane disruption. The quantification of RhoA activity in those images (Fig. 17 D) revealed that under control conditions, RhoA could be significantly activated by ET-1 treatment. On the contrary, ET-1 treatment led to a decrease in RhoA activity after cholesterol depletion. These data indicate that although RhoA-GTP shows only a very minor co-localization with caveolin-3 (Fig. 6), its regulation by GPCRs is dependent on cholesterol and the organization of the sarcolemma. Both, after TAC and MβCD treatment, this organization is strongly disrupted and the activity of RhoA is modified.
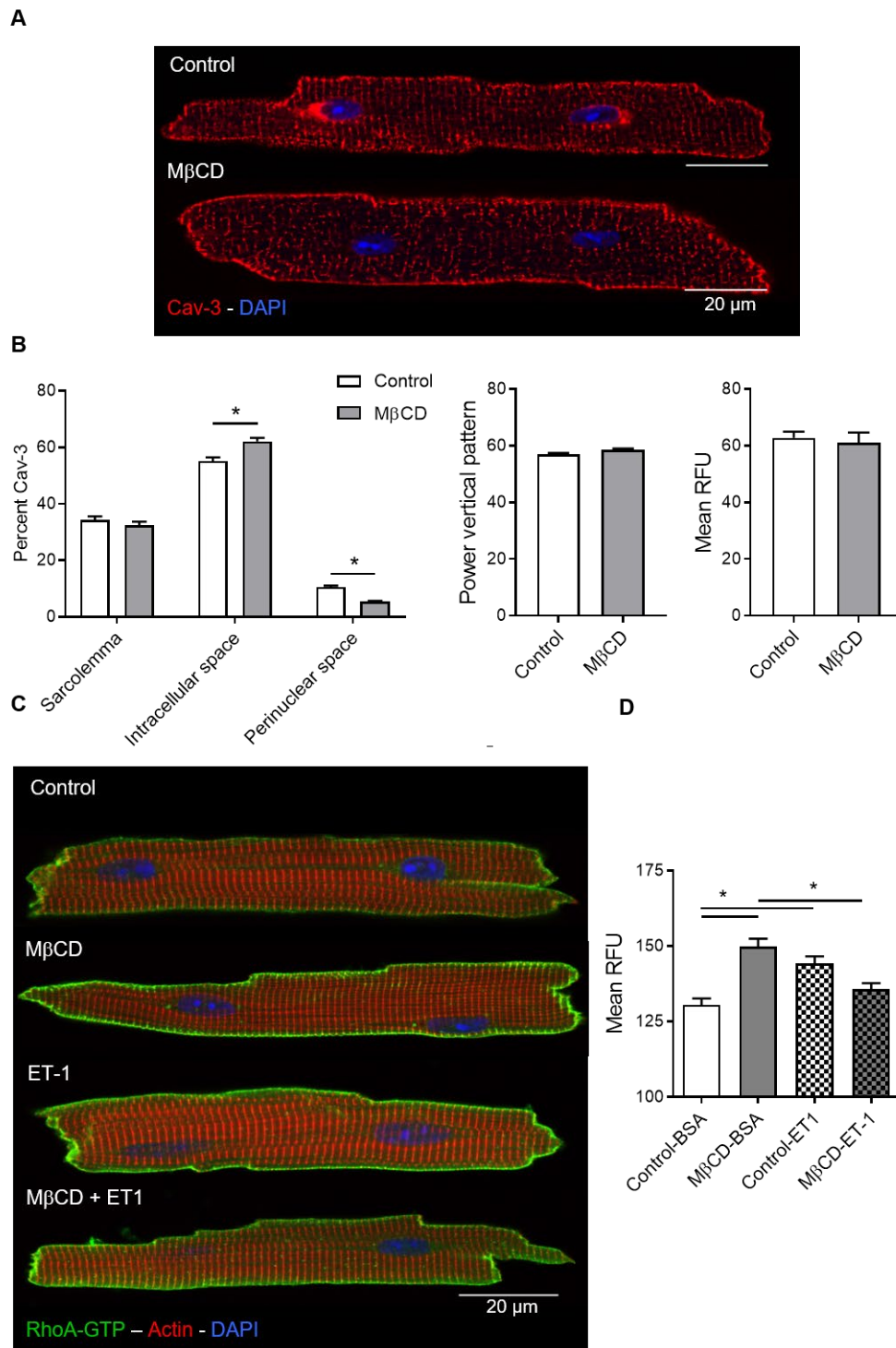
Fig. 17: Analysis of GPCR-dependent RhoA activation in isolated AMCM after MβCD treatment.
Adult mouse cardiomyocytes (AMCM) were isolated and cultured for 24 h in the presence or absence of 0.3 mM methyl-β-cyclodextrin. For RhoA activation 50 nM endothelin-1 (ET-1) was added to the cells for 90 sec, for control BSA was added. Afterwards the cells were directly fixed and immunofluorescence analysis for caveolin-3 or RhoA-GTP with subsequent confocal imaging was performed. **A)** Representative confocal center view image merges (63x magnification) of caveolin-3 (red) and nuclei (blue) are shown. **B)** Quantification of the percentage distribution of caveolin-3 in different cellular compartments is given as bar graph at the left. TTorg analysis of the intracellular caveolin-3 pattern is shown in the middle. Mean fluorescence units of complete cells are given at the right.

Presented are the means ± SEM, n=3, in total 40 to 50 cells per group, *p<0.05 by 2way ANOVA. **C)** Representative confocal center view images (63x magnification) of RhoA-GTP (green) are shown in combination with actin (red) and nuclei (blue). **D)** Mean RhoA-GTP fluorescence from confocal overview images (10x magnification) was quantified and is given as means ± SEM, n=3 with >200 cells per group,*p<0.05 by 1way ANOVA. Scale bars 20 µm.

4.4   Analysis of active RhoA localization in human adult atrial cardiomyocytes

All data presented so far, are showing a predominant localization of active RhoA at the sarcolemma in adult mouse cardiomyocytes. To confirm that this staining is not restricted murine cells, human atrial cardiomyocytes were used for immunofluorescence analysis. The cells were kindly provided by Prof. Niels Voigt from the Institute of Pharmacology and Toxicology, University Medical Center Göttingen. As shown in Fig. 18, active RhoA showed a similar distribution in the human cardiomyocyte compared to AMCM. Besides the predominant localization at the sarcolemma, a fine intracellular striation was detectable. Unlike in human adult atrial cardiomyocytes, perinuclear granules were detected by confocal imaging with the anti-RhoA-GTP antibody. However, as these granules also appeared upon excitation with the 633 nm laser without having a corresponding fluorophore used, the detected signal is highly likely based on autofluorescence of this structure.
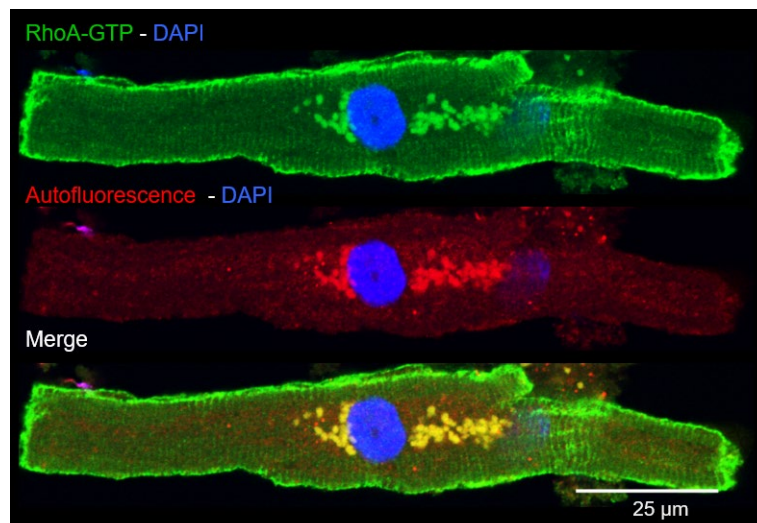
Fig. 18: Detection of RhoA-GTP in adult human atrial cardiomyocytes.
The adult human atrial cardiomyocytes were kindly provided by Prof. N. Voigt. After isolation, the cells were fixed and immunofluorescence analysis of active RhoA (green) was performed. The nuclei were stained with DAPI (blue). In addition, image acquisition with the 633 nm laser was performed to demonstrate the autofluorescence of the perinuclear granules. Shown is a representative cell, scale bar 25 µm.

4.5 Analysis of p63RhoGEF localization in adult mouse cardiomyocytes

The guanine nucleotide exchange factor p63RhoGEF had been demonstrated to be expressed in the heart and to be up-regulated after transverse aortic constriction [151]. Moreover, p63RhoGEF was shown to mediate the $G_{q/11}$-dependent RhoA activation in neonatal rat cardiomyocytes (Preliminary results chapter 2) and fibroblasts, as well as in adult rat smooth muscle cells [150].

To validate the role of p63RhoGEF in AMCM, the localization of the protein had to be analyzed first. To do so, several commercially available antibodies were tested by immunoblotting of different cell lysates from fibroblasts and cardiomyocytes. Out of four different antibodies, only one was able to detect endogenous p63RhoGEF as confirmed by p63RhoGEF-knockout cell lysates (data not shown). This antibody, however, strongly detected an additional protein with a molecular weight of around 50 kD. By using this antibody in immunofluorescence studies, it became apparent that the detected 50 kD protein is likely a tubulin isoform. As these experimental obstacles made it impossible to analyze the localization of endogenous p63RhoGEF in AMCM, an overexpression approach was chosen for the subsequent localization studies.

Isolated AMCM were transduced with adenoviruses encoding c-myc-tagged full-length p63RhoGEF (Ad-p63RhoGEF) or c-myc-tagged N-terminally truncated p63RhoGEF (Ad-p63ΔN). Both viruses additionally led to the expression of EGFP, which allowed the identification of efficiently transduced cells. After 48 h of transduction AMCM were fixed and immunostained. The localization of full-length or N-terminally truncated p63RhoGEF was visualized with an antibody against the c-myc tag. To ensure that the signal coming from the anti-c-myc-antibody was specific, AMCM were transduced with a virus encoding EGFP only. In these cells no signal could be detected..

In general, full-length p63RhoGEF appeared to be mainly associated to membranes including the perinuclear ER membrane as well as the outer sarcolemma. This is in line with the by Smith and colleagues described localization of the long 618 aa p63RhoGEF variant in adult mouse heart tissue [142]. In contrast, truncated p63ΔN showed a dominant sarcomeric localization and seemed to accumulate at the intercalated disk when higher expressed (Fig. 19 B). For quantification, the fluorescence distribution between different cellular compartments in AMCM with low and high transduction efficiency was analyzed. The cells were chosen based on their strengths of the EGFP signal. The comparison of cells expressing low and high amounts of full-length p63RhoGEF showed a similar percentage of the protein in the perinuclear region but differed significantly in the intracellular and sarcolemmal compartment. When compared to

lowly transduced cells, highly transduced cells showed a lower and higher percentage of the protein in the intracellular space and sarcolemma, respectively (Fig. 19 A). In contrast, the percentage of p63ΔN located at the sarcolemma was not dependent on the expression height. It is important to mention that in this analysis the sarcolemma did not contain the intercalated disc region as in this region a higher percentage of protein was present in highly transduced cells. Similar as for the full-length protein, the fraction of p63ΔN in the intracellular compartment was reduced in strongly overexpressing cells (Fig. 19 B).

A

B
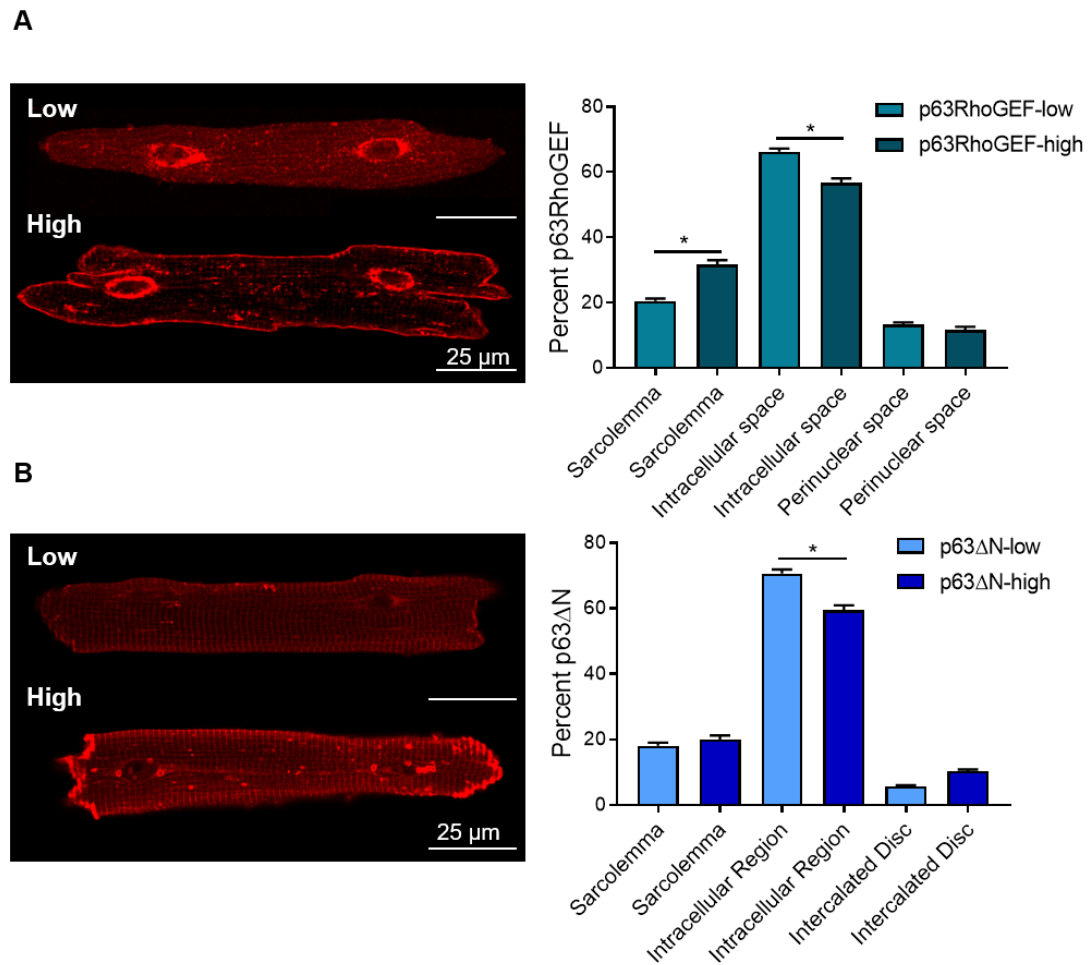
Fig. 19: Relation of p63RhoGEF transduction efficiency and localization in AMCM.
Transduced AMCM were cultured for up to 36 h with adenoviruses encoding for EGFP, p63RhoGEF or p63ΔN. **A)** Representative confocal images for AMCM with low (top) and high (bottom) transduction efficiency for full-length p63RhoGEF and corresponding quantification of p63RhoGEF localization. **B)** Representative confocal images for AMCM with low (top) and high (bottom) transduction efficiency for N-terminally truncated p63ΔN and corresponding quantification of p63ΔN localization. The p63RhoGEF and p63ΔN localization were visualized with an anti-c-myc antibody. Data are presented as means ± SEM for 30 cells per group, *$p < 0.05$. Scale bars: 25 µm.

Next to the analysis of the localization pattern of p63RhoGEF and its truncated mutant p63ΔN, co-localization studies were performed. Therefore, the transduced AMCM were additionally immunostained for α-actinin (Fig. 20 A, green), RhoA (Fig. 20 B, green), active RhoA (Fig. 20 C, green), and caveolin-3 (Fig. 20 D, green). The representative confocal images of complete cells in Fig. 16 show an overlay of the four channels with DAPI in blue, the additional protein of interest in green and c-myc in red. Magnifications additionally show the individual color channels and EGFP for positive transduction in grey. These multi-color images are shown and compared for AMCM transduced with all three viruses. As expected, AMCM transduced with the control virus (EGFP) exhibited no signal for c-myc since that virus does not express a c-myc-tagged protein.

Co-detection of α-actinin demonstrated that the sarcomeric regularity was not disturbed by the transduction with the different viruses and the respective expression of p63RhoGEF variants as shown in Fig. 20 A. AMCM transduced with all three viruses had a clear and regular striated pattern. A partial overlap with p63ΔN was visible at the z-disc, but no co-localization was found for the full-length protein (Fig. 20 A). Similar results were obtained for total RhoA as the protein was regularly distributed at the sarcomere in AMCM transduced with all three viruses. A partial co-localization with p63ΔN was detectable in the sarcomere. An additional, moderate perinuclear localization became apparent in p63RhoGEF overexpressing cells (Fig. 20 B). As observed before, active RhoA (RhoA-GTP) located in all three conditions predominantly at the sarcolemma (Fig. 20 C). This membrane distribution of RhoA-GTP was comparable for AMCM transduced with the three different viruses. Full-length p63RhoGEF seemed to co-localized at the sarcolemma with active RhoA and p63ΔN showed an overlap at the intercalated disc. The membrane protein caveolin-3 showed strong signals at the sarcolemma and in the perinuclear region for AMCM transduced with all three viruses (Fig. 20 D). Clear co-localization with full-length p63RhoGEF in these membrane compartments was found, whereas p63ΔN mainly showed an overlap at the former intercalated disc.

A

Ad-EGFP

| Merge | DAPI | α-actinin | c-myc | EGFP |

Ad-p63RhoGEF

| Merge | DAPI | α-actinin | c-myc | EGFP |

Ad-p63ΔN

25 µm

| Merge | DAPI | α-actinin | c-myc | EGFP |

10 µm

B

Ad-EGFP

| Merge | DAPI | RhoA | c-myc | EGFP |

Ad-p63RhoGEF

| Merge | DAPI | RhoA | c-myc | EGFP |

Ad-p63ΔN

25 µm

| Merge | DAPI | RhoA | c-myc | EGFP |

10 µm
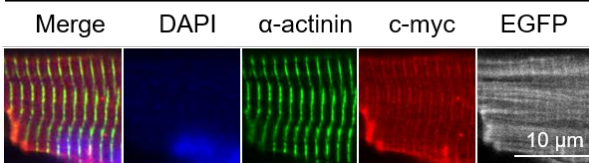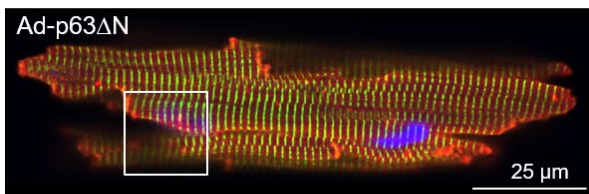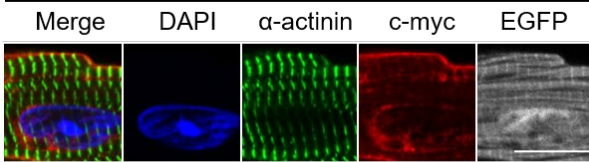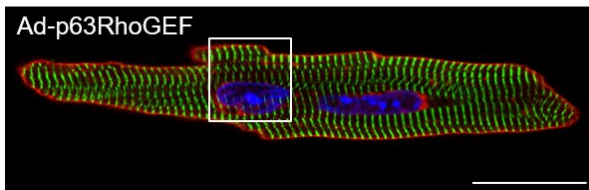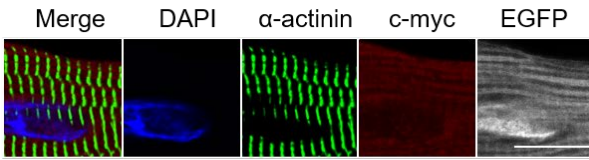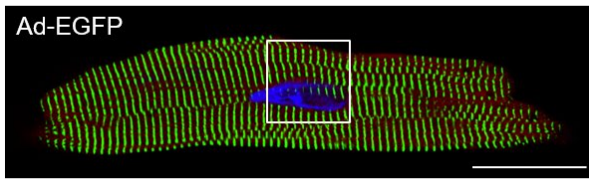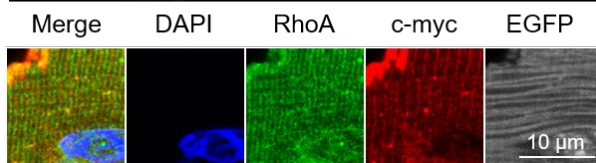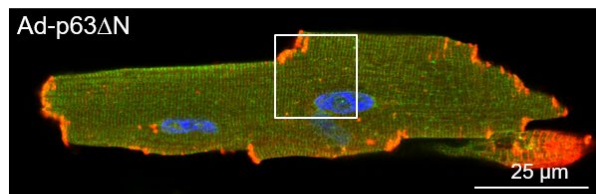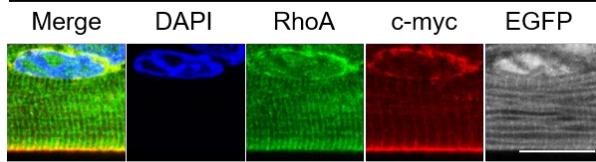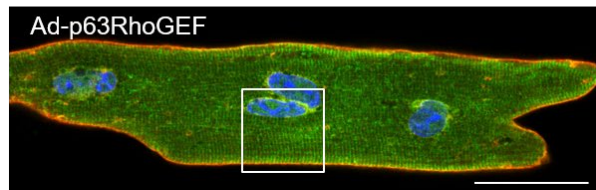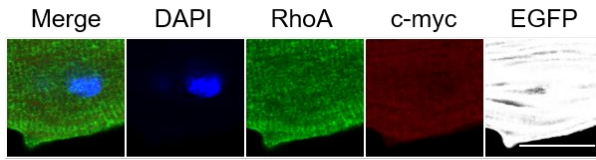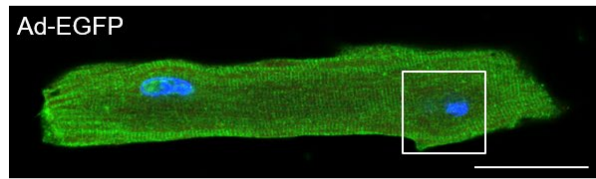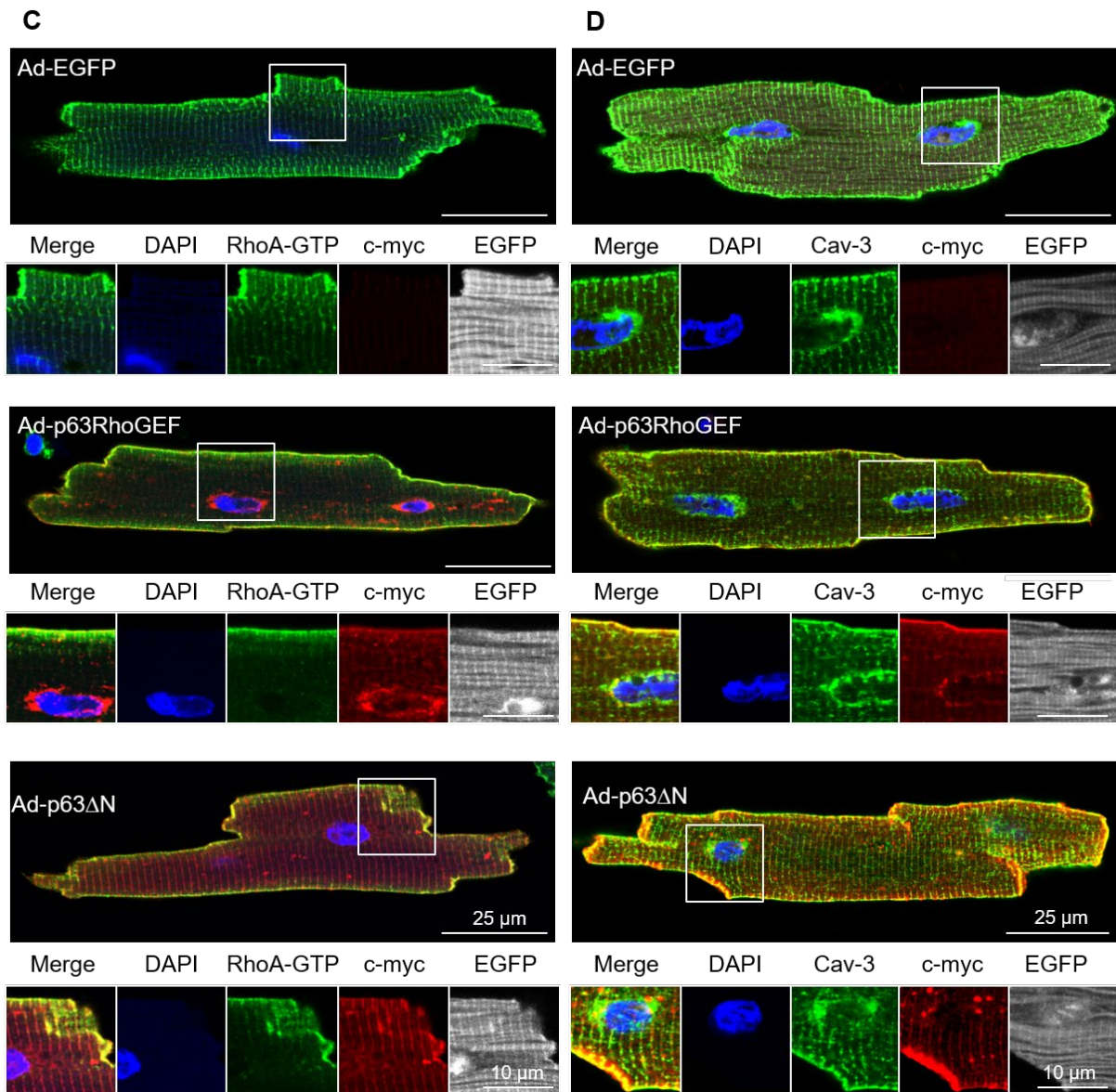
Fig. 20: Analysis of p63RhoGEF localization in AMCM.

Isolated adult mouse cardiomyocytes (AMCM) were transduced for up to 48 h with recombinant adenoviruses encoding EGFP only (Ad-EGFP), or EGFP and full-length, c-myc-tagged p63RhoGEF (Ad-p63RhoGEF), or EGFP and N-terminally, c-myc-tagged truncated p63RhoGEF (Ad-p63ΔN). The localization of p63RhoGEF was visualized by immunofluorescence with help of an anti-c-myc antibody (red). Transduced cells were identified by EGFP (gray scale) expression. Co-staining of nuclei with DAPI (blue) was performed. To characterize the localization of p63RhoGEF, the following proteins were additionally analyzed by immunofluorescence: **A)** α-actinin (green), **B)** RhoA (green), **C)** active RhoA (green) and **D)** caveolin-3 (green). The representative images of complete cells show an overlay of all four channels. Magnifications (below) show all individual channels and overlay excluding the EGFP signal. Scale bar: 25 μm or 10 μm.

Due to the observed co-localization of overexpressed full-length p63RhoGEF and active RhoA at the sarcolemma in center view images (Fig. 20 C), surface view imaging was performed in order to study the pattern of both proteins. As shown in Fig. 21 A, the overexpressed

p63RhoGEF showed no overall co-localization with active RhoA. The distribution of p63RhoGEF at the surface was in general patchier than of active RhoA. The degree of signal overlaps was low and mainly restricted to areas of the former intercalated discs (Fig. 21 A). Next, active RhoA levels were detected in 10x overview images. Unfortunately, application of the GPCR ligands ET-1, PE and AngII did not show any positive responses in control-transduced cells and only minor changes in p63RhoGEF overexpressing cells (Fig. 21 B). If the observed unresponsiveness of the transduced cells was a consequence of the adenoviral transduction, the long culture time or both is difficult to assess.

A

B
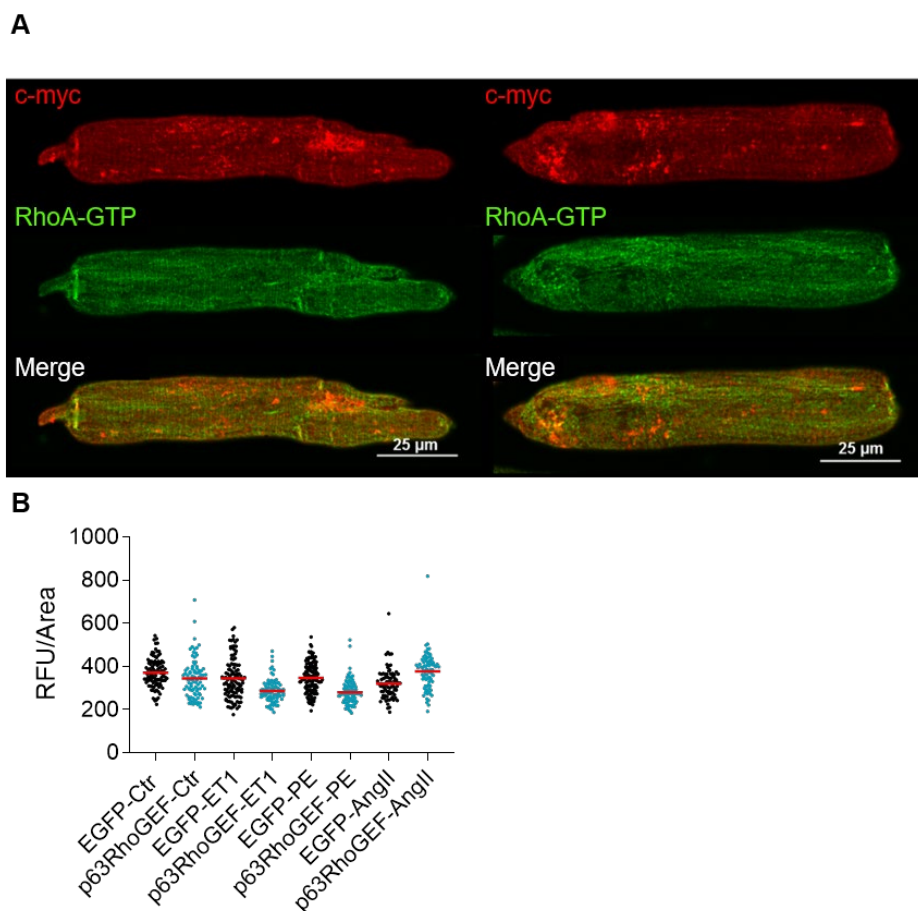
Fig. 21: Sarcolemmal localization of p63RhoGEF and active RhoA in AMCM.

Isolated adult mouse cardiomyocytes (AMCM) were transduced for up to 48 h with recombinant adenoviruses encoding EGFP only (Ad-EGFP) or EGFP and full-length, c-myc-tagged p63RhoGEF (Ad-p63RhoGEF). **A)** The localization of p63RhoGEF and active RhoA were visualized in Ad-p63RhoGEF transduced AMCM by immunofluorescence with help of an anti-c-myc antibody (red) and a RhoA-GTP antibody (green). Confocal surface view images were taken. Shown are two representative cells. Scale bar 25 µm **B)** The transduced cells were treated after 48 h with 50 nM endothelin-1 (ET-1), 100 µM phenylephrine (PE) or 100 nM angiotensin II (AngII) for 90 sec. For control BSA was added to the cells. Afterwards the cells were directly fixed and immunofluorescence analysis for RhoA-GTP with subsequent confocal imaging was performed. Total RhoA-GTP fluorescence from confocal

overview images (10x magnification) was quantified and is given normalized to the area as individual vales of 85 to 135 cells per condition. The means are indicated in red.

4.6 Regulation of membranous structures by p63RhoGEF overexpression in adult mouse cardiomyocytes

Co-localization analysis of p63RhoGEF and caveolin-3 in confocal center view images revealed (Fig. 22 A) that when p63RhoGEF is relatively low expressed, its correlation with caveolin-3 is higher than *vice versa*. This is mainly due to its predominant perinuclear localization and the lacking sarcolemmal localization. In highly expressing cells both proteins co-localize to a similar extent to each other, which can be explained by the increasing localization of p63RhoGEF at the sarcolemma (Fig. 22 B). However, by analyzing surface view images of both proteins, the obtained correlation coefficients were remarkable lower as those detected in center view images (Fig. 22 C). This is mainly based on the missing signal resolution at the sarcolemma in center view images. In addition to the degree of co-localization of both proteins, the impact of p63RhoGEF on the distribution of caveolin-3 was assessed. Interestingly, the accumulation of p63RhoGEF in the perinuclear region, which is independent of its expression height, led to an increased accumulation of caveolin-3 in the same area. The observed increase of p63RhoGEF at the sarcolemma in highly transduced cells did not result in higher caveolin-3 levels, instead its intracellular amount was decreased (Fig. 22 D).
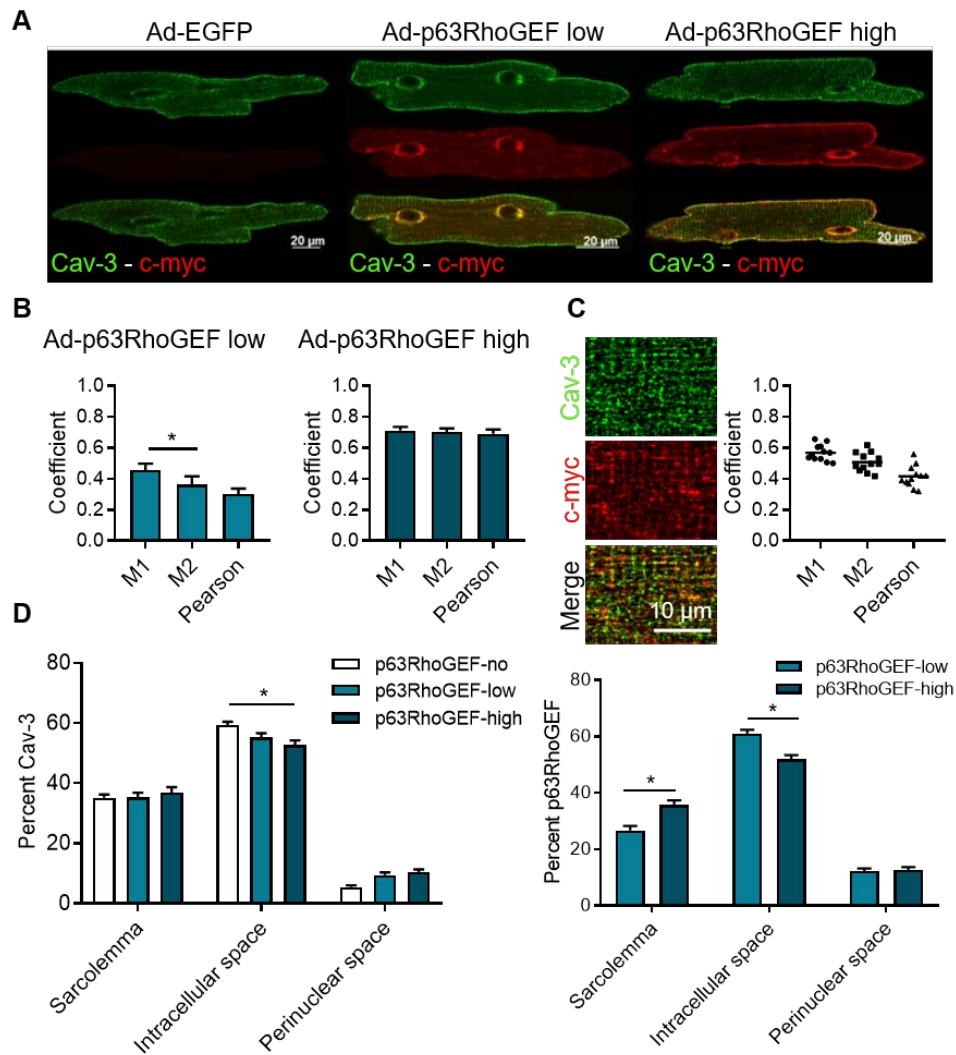
Fig. 22: Analysis of the co-localization of p63RhoGEF and of caveolin-3 in AMCM.

Isolated adult mouse cardiomyocytes (AMCM) were transduced for up to 48 h with recombinant adenoviruses encoding for EGFP only (Ad-EGFP), or for EGFP and for full-length, c-myc-tagged p63RhoGEF (Ad-p63RhoGEF). The localization of p63RhoGEF and caveolin-3 were visualized by immunofluorescence with help of a c-myc antibody (red) and an anti-caveolin-3 antibody (green), respectively. **A)** Representative center view images of p63RhoGEF and caveolin-3 are given of control transduced (Ad-EGFP) and Ad-p63RhoGEF-transduced cells showing low and high p63RhoGEF expression. The merges are presented below. Scale bar 20 µm. **B)** Co-localization of p63RhoGEF and caveolin-3 was analyzed by the ImageJ plugin Coloc2 in center view images. M1 reflects the co-localization of p63RhoGEF with caveolin-3 and M2 of caveolin-3 with p63RhoGEF. In total 20 to 25 cells were analyzed from 3 independent transduction experiments. Given are the means ± SEM, *p<0.05. **C)** Representative magnifications of surface view images are given of cells highly expressing p63RhoGEF. Co-localization of p63RhoGEF and caveolin-3 was analyzed by the ImageJ plugin Coloc2 in 4 cells in three different areas. The single values are shown together with their mean. **D)** The localization of caveolin-3 (left) and p63RhoGEF (right) was analyzed in control transduced cells (for caveolin-3 analysis, p63RhoGEF-no) and cells expressing low (p63RhoGEF-low) and high (p63RhoGEF-high) amounts of p63RhoGEF. In total 20 to 25 cells of 3 independent transduction experiments were analyzed. Given are the percentages as means ± SEM of the respective proteins in each compartment, *p<0.05.

As p63RhoGEF expression influenced the distribution of the membrane protein caveolin-3, its impact on the intracellular secretory membrane system was analyzed.

First, the co-localization of both p63RhoGEF constructs with proteins containing the ER retention and targeting motif KDEL (lysine - aspartic acid - glutamic acid - leucine) was investigated. Surprisingly, this revealed a very strong overlap between full-length p63RhoGEF and KDEL-containing proteins as well as between p63ΔN and KDEL-proteins (Fig. 23 A). Quantification of the co-localization demonstrated that p63RhoGEF and KDEL-proteins co-localized to a similar extent to each other, whereas the KDEL-proteins showed a higher correlation to p63ΔN than *vice versa* (Fig. 23 B). Although a certain degree of co-localization was also found for caveolin-3, the surprising increase in KDEL-signal intensity in cells overexpressing the two p63RhoGEF constructs compared to control transduced cells was unusual. To further investigate this phenomenon, immunoblot studies were performed. However, with the used antibody no difference in the detected KDEL-proteins were found (data not shown), but instead the p63RhoGEF constructs could be detected. This is exemplarily shown for p63ΔN in Fig. 23 C. Thus, it can be assumed that the observed co-localization results from an experimental artefact. The reason for this artefact could lay in the recognition of the antibody of the C-terminal EDEL sequence of p63RhoGEF.
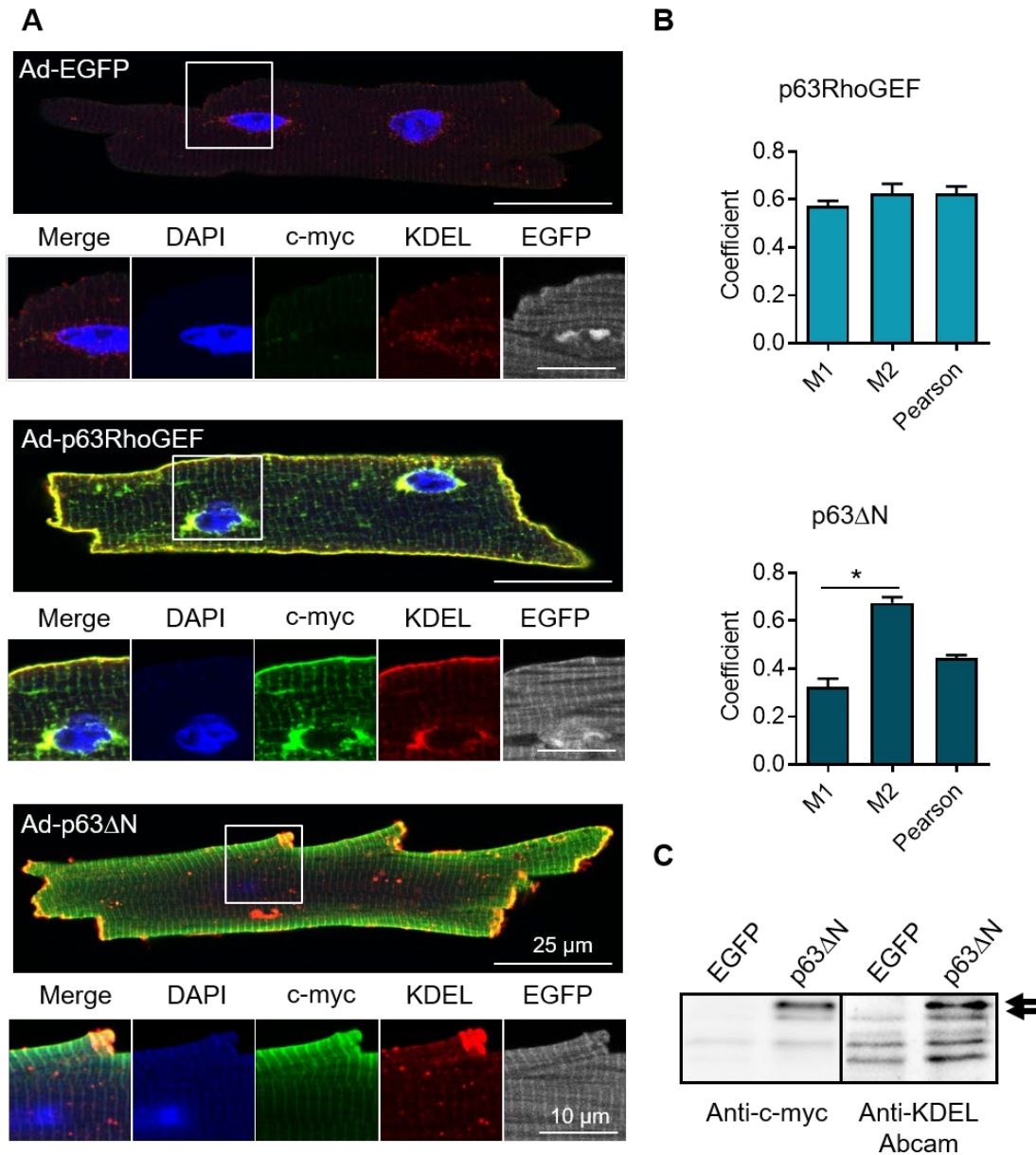
Fig. 23: Analysis of the co-localization of p63RhoGEF and of KDEL-proteins in AMCM.

Isolated AMCM were transduced for up to 48 h with recombinant adenoviruses encoding EGFP only (Ad-EGFP), EGFP and full-length c-myc-tagged p63RhoGEF (Ad-p63RhoGEF), or EGFP and N-terminally truncated c-myc-tagged p63RhoGEF (Ad-p63ΔN). The localization of c-myc tagged p63RhoGEFand p63ΔN were detected with an anti-c-myc antibody, KDEL proteins were detected with an antibody against the KDEL-motif. Immunostained AMCM were visualized by confocal microscopy and confocal images were used for co-localization analyses. **A)** The representative images of complete cells show an overlay of all four channels. Magnifications (below) show all individual channels and overlay excluding the EGFP (gray scale) signal. Scale bar: 25 µm or 10 µm. **B)** Co-localization of p63RhoGEF constructs and KDEL-proteins was analyzed by the ImageJ plugin Coloc2 in center view images. M1 reflects the co-localization of the respective p63RhoGEF construct with KDEL and M2 of KDEL with the p63RhoGEF construct. In total 31 cells per condition were analyzed from 3 independent transduction experiments. Given are the means ± SEM, *p<0.05. **C)** Representative Immunoblots of c-myc and KDEL in cell lysates from

AMCM transduced either with Ad-EGFP or with Ad-p63ΔN. For immunoblotting, the same antibodies were used as for the immunostains shown in **A**) The arrows indicate the specific p63ΔN bands.

Second, localization analysis of the cis-Golgi matrix protein GM-130 was performed together with the p63RhoGEF constructs. Independent of the used adenoviral constructs, GM-130 was found in discrete speckles in the perinuclear region and in speckles distributed over the cells (Fig. 24 A). Furthermore, GM-130 was located close to p63RhoGEF accumulations in the in the Ad-p63RhoGEF-transduced cells. Quantification of the particle size revealed a significant decrease from 0.57 μm² to 0.52 μm² for p63RhoGEF and p63ΔN compared to control AMCM expressing EGFP only. The average particle number per cell in one center view imaging plane changed significantly from 42 particles in AMCM overexpressing EGFP only, to 45 particles for p63ΔN and to 58 particles per AMCM in p63RhoGEF transduced AMCM. Moreover, p63RhoGEF expression led to a slight, but significant reduction of GM-130 in the perinuclear region. Instead more GM-130 could be detected in the cell periphery (Fig. 24 B).
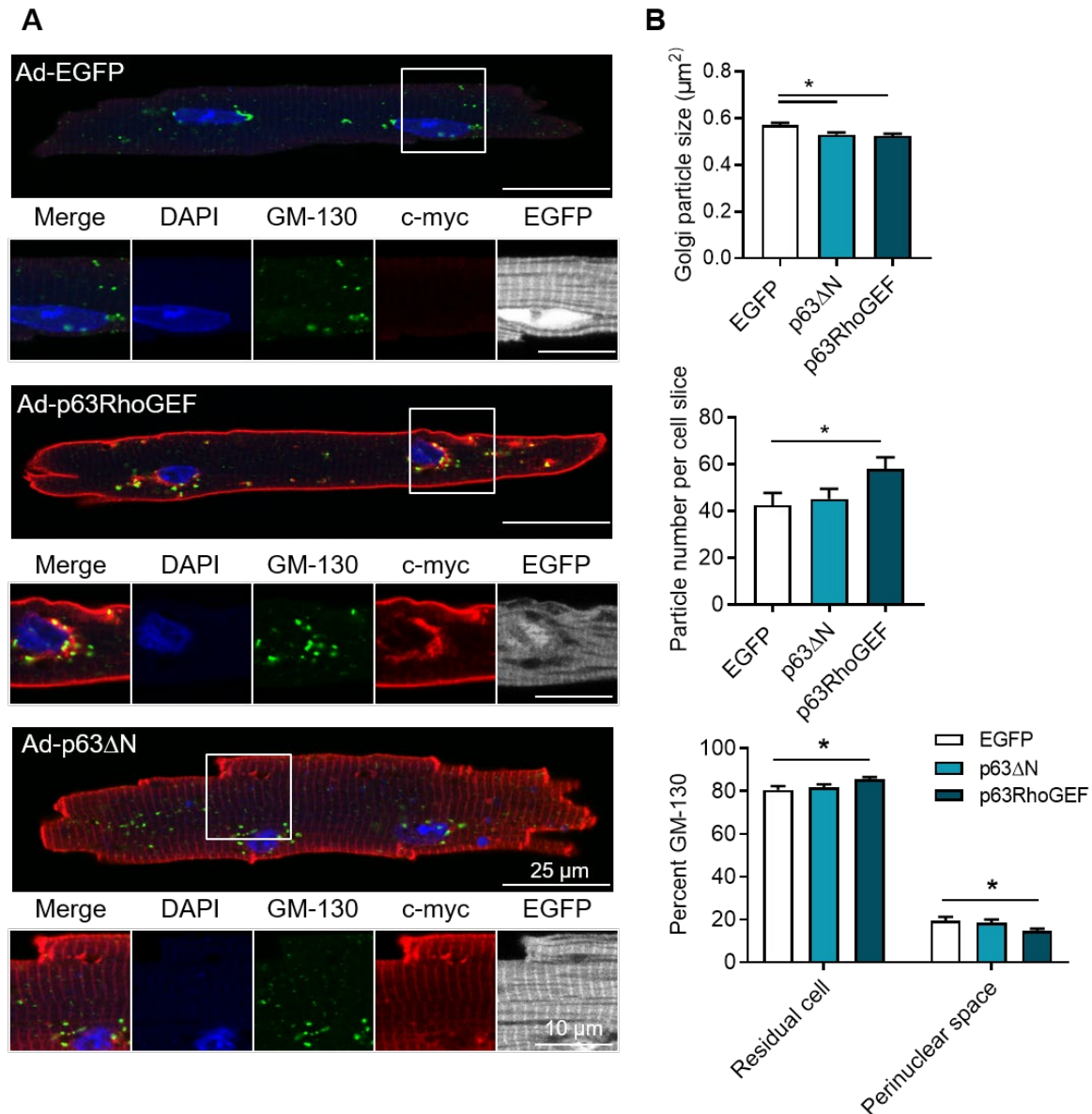
Fig. 24: Analysis of the co-localization of p63RhoGEF and of the cis-Golgi matrix protein GM-130 in AMCM.

Isolated adult mouse cardiomyocytes (AMCM) were transduced for up to 48 h with recombinant adenoviruses encoding for EGFP only (Ad-EGFP), or for EGFP and for full-length, c-myc-tagged p63RhoGEF (Ad-p63RhoGEF), or for EGFP and for N-terminally, c-myc-tagged truncated p63RhoGEF (Ad-p63ΔN). The localization of p63RhoGEF was visualized by immunofluorescence with the help of a c-myc antibody (red) and the Golgi apparatus with an antibody against the cis-Golgi matrix protein GM-130. Transduced cells were identified by EGFP (gray scale) expression. Co-staining of nuclei with DAPI (blue) was performed. **A)** Representative center view confocal images are shown as an overlay of all four channels. Magnifications (below) show all individual channels and overlay excluding the EGFP signal. Scale bar: 25 µm. **B)** Analysis of the Golgi particle size (upper) and the particle number (middle) was performed with the help of the particle analysis tool of ImageJ. In total 35 to 45 cells per group were analyzed. The distribution of GM-130 was analyzed by its fluorescence in the perinuclear region (selection of the nuclei with 2.5 µm enlargement) and in the rest of the cells. In total 20 to 25 cells per group were analyzed. All values are given as means ± SEM, n=4, *p<0.05.

4.7 Regulation of cell morphology by p63RhoGEF overexpression in adult mouse cardiomyocytes

Another question that had to be addressed was the impact of the different p63RhoGEF constructs on the morphology of AMCM. To answer that question quantitatively, AMCM of three individual mice were isolated, adenovirally transduced with the three different constructs (EGFP only, p63RhoGEF and p63ΔN), cultured for up to 36 h, fixed and immunostained. By visualizing the EGFP signal with a confocal microscope using a 10x objective, several cells could be imaged simultaneously. Imaging and quantitative analysis of AMCM overexpressing EGFP only revealed no direct correlation between individual transduction efficiency (RFU of EGFP) and cell size (area and length) (Fig. 25 A).

The representative confocal images in Fig. 25 B show α-actinin (green) and c-myc (red) immunostains of AMCM overexpressing EGFP only, p63ΔN or p63RhoGEF. For the EGFP only construct no signal was expected because of the missing c-myc tag. These representative confocal images visualize that AMCM overexpressing p63RhoGEF appear larger than AMCM overexpressing EGFP only or p63ΔN. The representative immunoblots of AMCM lysates on the right confirm overexpression of the three different constructs.

To validate the size of AMCM overexpressing p63RhoGEF, cross-sectional area, length and depth were quantitatively analyzed in AMCM overexpressing either EGFP only, p63ΔN or p63RhoGEF. These data were summarized as bar graphs in Fig. 25 C. As expected from the representative confocal images (Fig. 25 B), average data show that AMCM cross-sectional area is moderately larger and smaller in cells overexpressing p63RhoGEF and p63ΔN, respectively. However, only the difference between the two different p63RhoGEF constructs was significant. The averaged data of cell length for all three constructs show a significant increase for p63RhoGEF compared to EGFP only and p63ΔN. Deviating from these results, the cell depth seems not to be influenced by the overexpression of p63RhoGEF. In summary, these data indicate that only overexpression of p63RhoGEF, but not of EGFP alone or of p63ΔN, has an impact on cell morphology and leads to an increase in cell size.
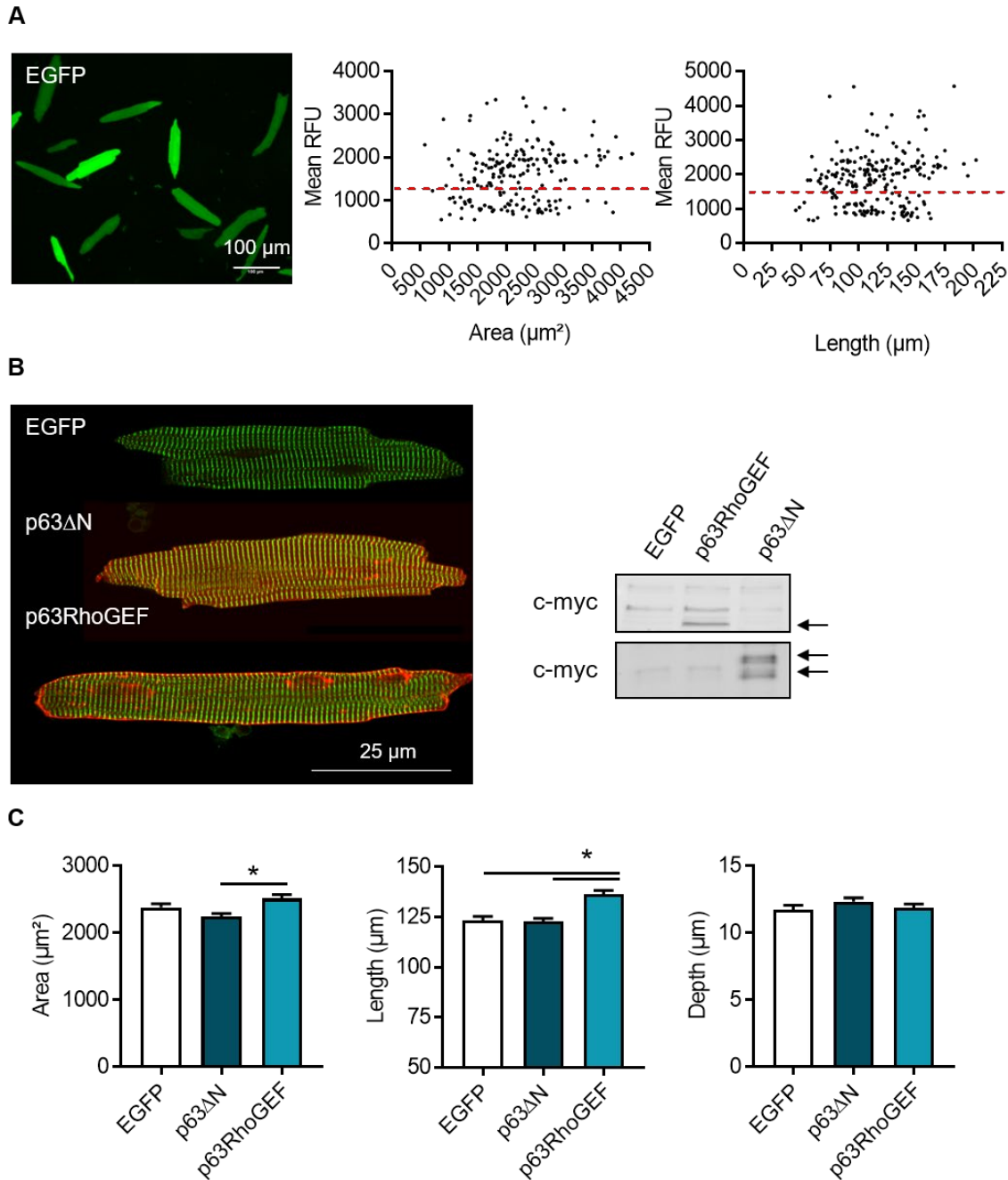
Fig. 25: Impact of the adenovirus-mediated expression of p63RhoGEF on the morphology of WT-AMCM.

AMCM were transduced with adenoviruses encoding for EGFP, for full-length p63RhoGEF or for N-terminally truncated p63RhoGEF (p63ΔN) and cultured for up to 36 h. **A)** (left) Representative fluorescence image of AMCM transduced with adenovirus overexpressing EGFP only. Individual EGFP positive cells show different transduction efficiencies as indicated by the intensity of the green signal. (right) Correlation of transduction efficiency measured by relative fluorescence units (RFU) with area (μm²) and length (μm) of individual AMCM (scale bar 100 μm). The red dashed line represents the fluorescence threshold of positively transduced cells. Values underneath the line are based on autofluorescence of the cells. **B)** Representative confocal images of α-actinin (green) and c-myc (red) in adenovirally transduced AMCM (left) and the corresponding representative immunoblots of the cell lysates (right) are shown. Overexpression of p63RhoGEF and p63ΔN was confirmed in an immunoblot with an anti-c-myc

antibody. Scale bar 25 µm. **C)** Analysis of the cross-sectional area (left), cell length (middle) and cell depth (right) of EGFP, p63RhoGEF and p63ΔN transduced AMCM measured in confocal images with 10x magnification are depicted. The values are given as means ± SEM. For area and length analysis: n=3, >200 cells *p<0.05; for depth analysis: n=3, >70 cells.

Having shown that overexpression of p63RhoGEF in AMCM increased cell size, especially in length (as shown in Fig. 25 C), the subsequent question was if that morphological change also has an influence on sarcomeric architecture. Although already briefly mentioned, the sarcomeric structure was further quantitatively analyzed here. For that purpose, AMCM were transduced with viruses encoding for EGFP only, for p63ΔN or for p63RhoGEF. Then, the cells were fixed and stained for F-actin. By peak-to-peak distance measurements of line scans, the average sarcomeric length of transduced AMCM was determined. Comparison of average sarcomere lengths in AMCM overexpressing either EGFP only, N-terminally truncated p63RhoGEF or full-length p63RhoGEF revealed no detectable difference indicating that overexpression of the two different p63RhoGEF constructs does not influence the sarcomeric length in AMCM (Fig. 26).
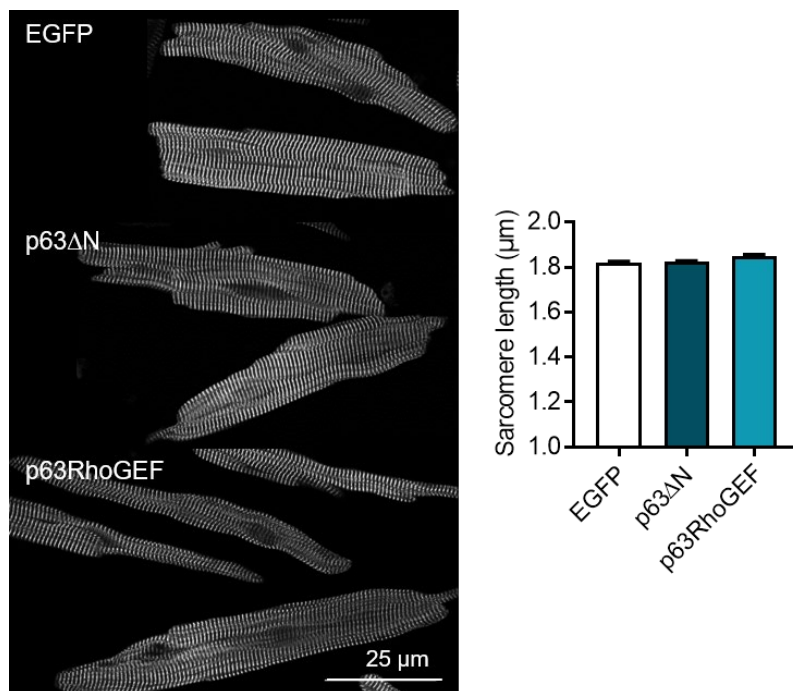
Fig. 26: Analysis of sarcomere lengths in WT-AMCM overexpressing p63RhoGEF or p63ΔN.
AMCM were transduced with adenoviruses encoding for EGFP, for full-length p63RhoGEF or for N-terminally truncated p63RhoGEF (p63ΔN) and cultured for up to 36 h. α-actinin was stained and confocal imaging was performed. (Left) Representative α-actinin images in gray scale are given. (Right) Corresponding quantification by peak-to-peak analysis of the sarcomeric lengths are depicted as means ± SEM, n=13 cells per group. Scale bar: 25 µm.

Based on the detected morphological changes in AMCM transduced with adenoviruses encoding for EGFP only, p63RhoGEF or p63ΔN (Fig.25, 26), the impact of the observed cell growth on the nuclear dimensions was analyzed. For all three adenoviruses, area, circularity and roundness of nuclei stained with DAPI were measured using the wand tool of ImageJ (Fig. 27 A). Interestingly, the average nucleus area significantly decreased from 69 µm² for EGFP only to 64 µm² for p63RhoGEF and 53µm² for p63ΔN. However, nuclei circularity, the ratio between area and perimeter, did not change. On the other hand, nuclear roundness, which refers to the major nuclear axis, was significantly changed. A value of 1 for roundness and circularity would describe a perfect circle. For EGFP only, a flat oval shape was depicted by the measured roundness of 0.38. In comparison to that, the pattern changed significantly to oval for p63RhoGEF (with a roundness of 0.43) and p63ΔN (with a roundness of 0.5) (Fig. 27 B).

A

$$Circularity = 4\,\pi \times \frac{[Area]}{[Perimeter]^2}$$

$$Roundness = 4 \times \frac{[Area]}{\pi[Major\ axis]^2}$$

B
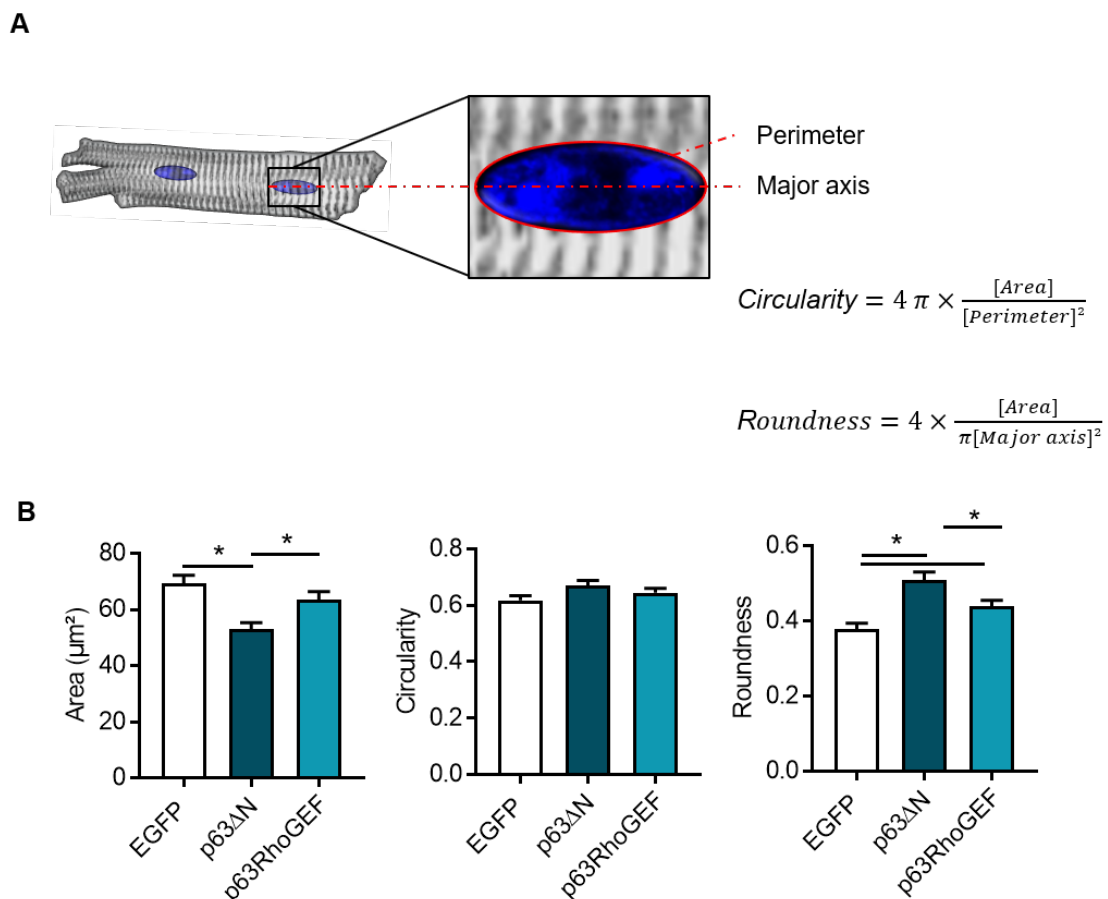
Fig. 27: Influence of p63RhoGEF on nuclei morphology in AMCM.

Adult mouse cardiomyocytes were cultured and transduced for up to 36 h with adenoviruses encoding EGFP, full-length p63RhoGEF (p63RhoGEF) and the N-terminal truncated construct (p63ΔN). **A)** Graphical illustration of an AMCM with two nuclei and magnification with perimeter and major axis highlighted is shown. Equations for the calculation of nucleus circularity and roundness measured with ImageJ are given. **B)** Analysis of nucleus area (left),

circularity (middle) and roundness (right) in EGFP-, p63RhoGEF- and p63ΔN-transduced AMCM measured in fluorescence images with 20x magnification are presented as means ± SEM, n=6 ,≥80 cells *p<0.05.

The data presented so far provided an understanding of the expression height dependent localization of p63RhoGEF and the resulting morphological changes in AMCM. By overexpressing the N-terminally truncated construct of p63RhoGEF, the importance of the N-terminus for the proper localization at the sarcolemma could be shown. For full-length p63RhoGEF a sarcolemmal, perinuclear and partially sarcomeric localization was found. For p63ΔN a predominant localization at the intercalated discs and in the sarcomere was detected. Furthermore, an influence of p63RhoGEF on the localization of membrane proteins like caveolin-3 and on the morphology of the Golgi apparatus was identified. Finally, an increase in cell volume, reflected by an increase in cell length and no changes in area and depth, in p63RhoGEF overexpressing cells was identified which was accompanied by a rounding of the cell nucleus. p63ΔN did not influence the cell volume but reduced the nucleus area and increased the nuclear roundness.

4.8   Influence of the genetic deletion of p63RhoGEF on heart and cardiomyocyte morphology

The results obtained with transduced AMCM, led to the question which consequence a lack of p63RhoGEF in AMCM might have. To answer this question, a p63RhoGEF knockout mouse was generated. By integration of flox-sites flanking exons 1 and 2 of the p63RhoGEF allele in the genome and subsequent mating with a mouse line expressing Cre-recombinase, the p63RhoGEF knockout mouse line was generated.

Prior to the cellular analysis, the morphological properties of the hearts were investigated by echocardiography, which was kindly performed by the service unit from the SFB 1002 at the University Medical Center Goettingen. For that purpose, hearts (Fig.28 A) from 10-12 week old male mice were investigated for anterior and posterior wall thickness and for the cross-sectional area of the left ventricular lumen during systole and diastole. These values are indicators for hypertrophy and dilation of the heart. Male wild-type mice were compared with male mice heterozygous (HET) and homozygous (KO) for the p63RhoGEF knockout. In general, no significant differences were found in all parameter investigated in the three mouse lines. By trend, the heterozygous mice showed slightly thinner wall dimensions as well as increased ventricular areas in systole and diastole pointing to mild dilation of the ventricle (Fig. 28 B). This is in line with data of Dr. Anita Ongherth, who demonstrated that the systolic

and diastolic volume of these mice is significantly higher compared to wildtype mice (http://hdl.handle.net/11858/00-1735-0000-002B-7CC9-0).
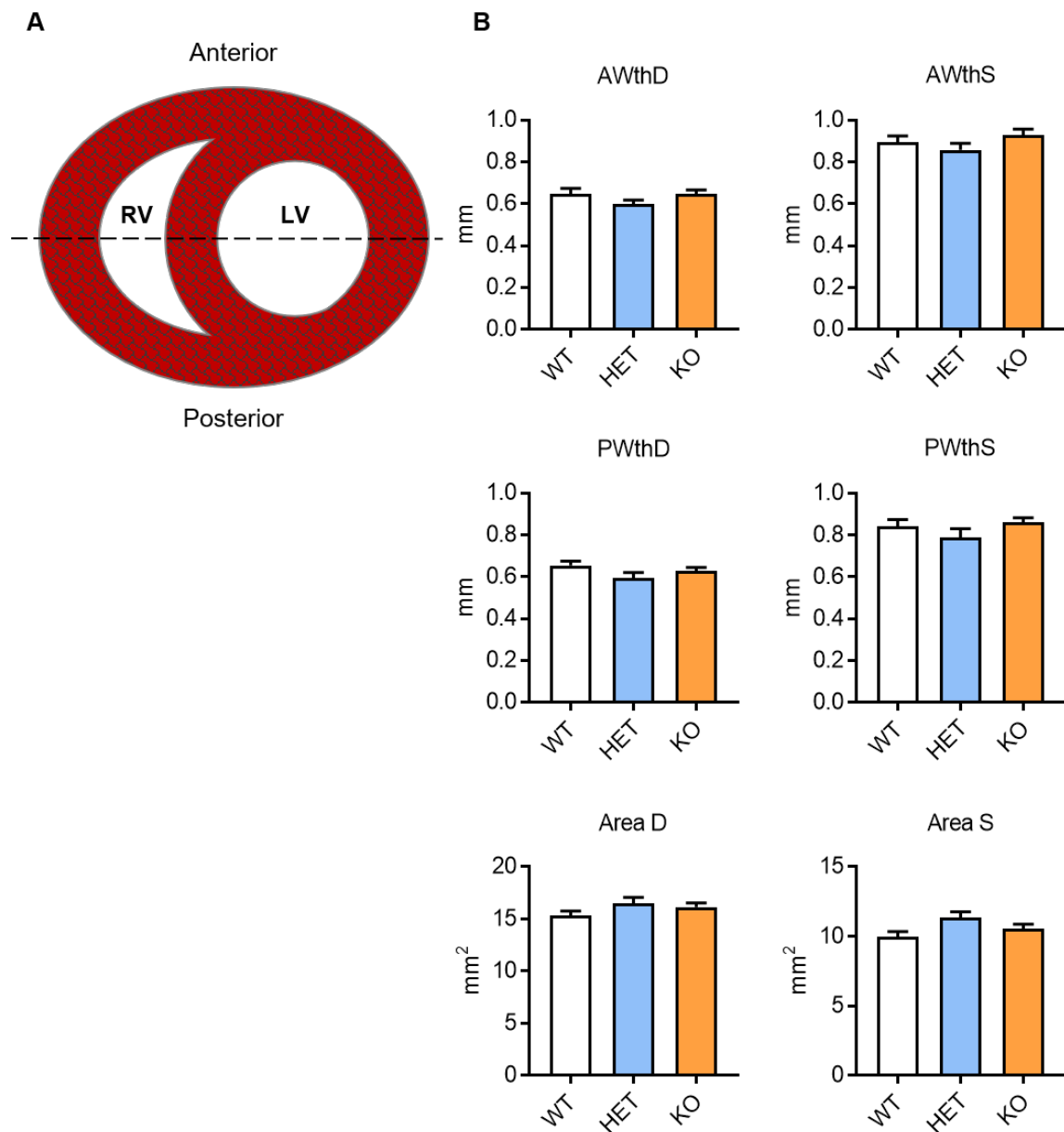
Fig. 28: Analysis of the cardiac dimensions in mice with p63RhoGEF deletion.
The basal cardiac dimension of 10-12 weeks old male mice was determined by echocardiography. **A)** Schematic cross section of the heart is shown for better orientation. Indicated are the right (RV) and left (LV) ventricles and the anterior-posterior orientation. **B)** Average values of anterior wall thickness in diastole (AWthD), anterior wall thickness in systole (AWthS), posterior wall thickness in diastole (PWthD), posterior wall thickness in systole (PWthS), area of the cross sectional left ventricular lumen in diastole (Area D) and area of the cross sectional left ventricular lumen in systole (Area S) are shown as means ± SEM from 28 wildtype (WT), 16 heterozygous (HET) and 43 homozygous knockout (KO) animals.

Subsequently, the AMCM were isolated using a modified Langendorff perfusion system and fixed after 1 h or 24 h in culture. The dimensions of the cells were quantified using ImageJ.

For cardiomyocytes length, no significant differences were measured between all three genotypes. In addition, during 24 h in culture the cell length did not change over time. In contrast to cardiomyocyte length, the cell depth was slightly smaller in AMCM from HET and KO mice. Strikingly, all three genotypes showed a slight reduction of cardiomyocytes depth for cells cultured for 24 h (Fig. 29 A). Directly fixed HET and KO AMCM were 6% flatter in average depth compared to control AMCM. In addition, AMCM cultured for 24 h lost 6% of depth for HET, 10% for WT and 16% for KO (Fig. 29 B).

The average area of directly fixed HET and KO AMCM was 4% larger compared to the controls. Furthermore, the average area of all AMCM significantly decreased significantly during 24 h of culture, by 10% in HET, 11% in WT and 12% in KO (Fig. 29 C).

To better understand the morphological changes in cell culture and in the different genotypes, the surface and volume of an elliptical barrel was calculated based on the measured parameters. Again, the culture-dependent reduction was evident for both the cellular volume and the associated surface. Cardiomyocytes from KO animals had the smallest average cell volume with 19600 μm^3 compared to control with 21800 μm^3 after 24 h of culture (Fig. 29 E). The calculated average cell surface was also strongly reduced after 24 h of culture with 6600 μm^2 compared to directly fixed WT cardiomyocytes with 6800 μm^2 (Fig. 29 D). In summary, cardiomyocytes of all three genotypes become smaller after 24 h in culture. Specifically, cardiomyocytes of p63RhoGEF KO mice developed a flatter cell shape in culture. In line with these results, the cell surface and volume were clearly smaller.
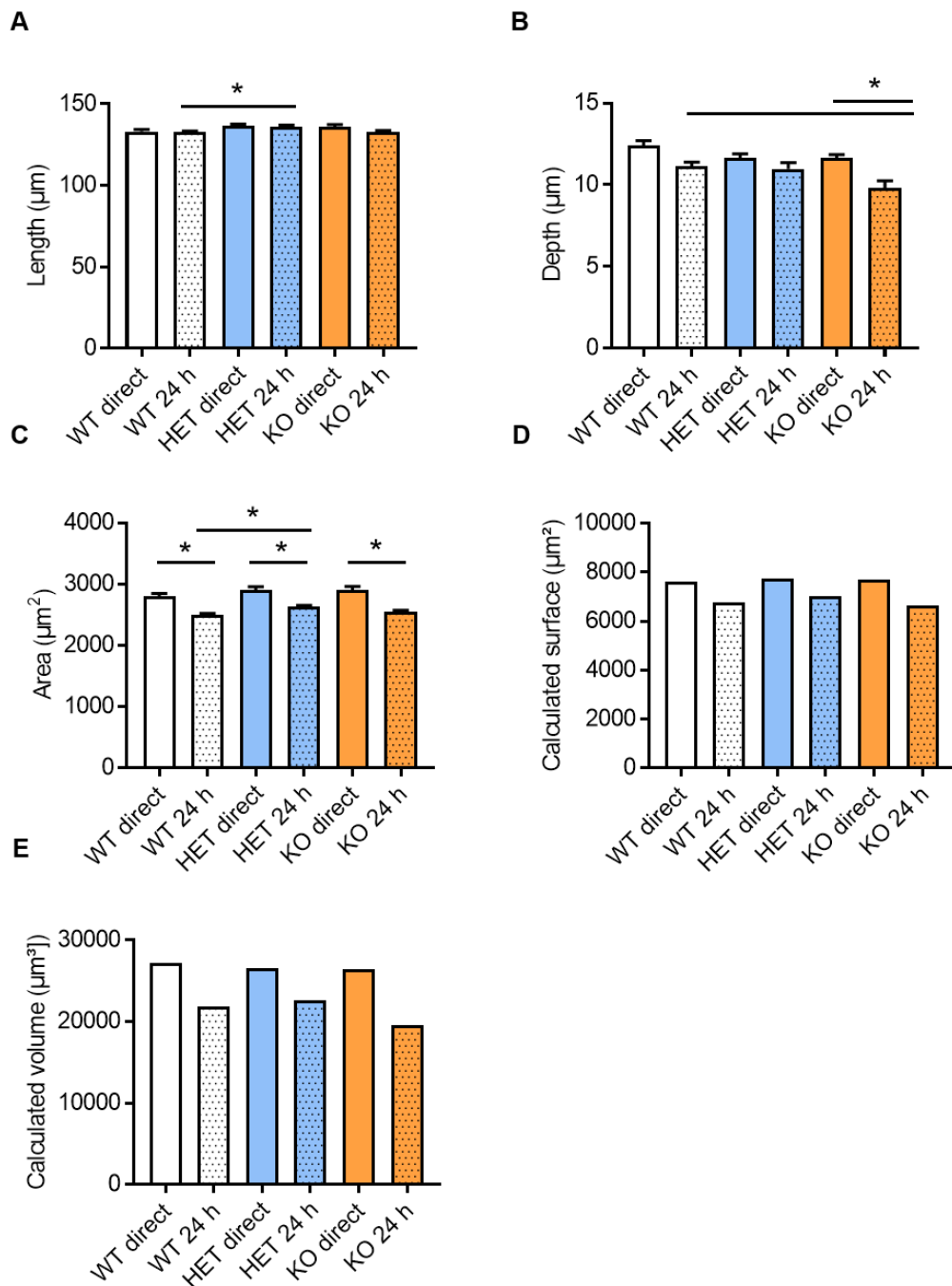
Fig. 29: Influence of p63RhoGEF deletion on the cellular morphology of AMCM.

Analysis of isolated AMCM from 10-20 week old male mice was performed. Cardiomyocytes from all three genotypes (wildtype (WT) heterozygous (HET) and knockout (KO)) were isolated via modified Langendorff perfusion system and seeded on laminin coated glass coverslips. Cells were either fixed after 1 h (direct) or after 24 h in culture. Dimensions were measured with ImageJ. Bar graphs summarize average values for **A)** length, **B)** depth, **C)** calculated area, **D)** calculated surface, and **E)** calculated volume of AMCM cultured for 1-24 h of various genotypes. Given are the values as means ± SEM, n>3, *p<0.05, length: 293-1345 cells, depth: 30 cells, area: 235-1040 cells.

As previously demonstrated, overexpression of p63RhoGEF had a significant influence on the nucleus morphology (Fig. 27 B). This raised the question if deletion of p63RhoGEF has an influence on the nuclear morphology as well. In line with results of the significant reduction of the area of AMCM cultured for 24 h, demonstrated in Fig. 29, nucleus morphology was analyzed in WT-, HET- and KO-AMCM. A significant reduction of the averaged nuclei area up to 21 % (WT 14%, HET 17%, KO 21%) was shown after 24 h in culture. Furthermore, AMCM with a full deletion of p63RhoGEF (KO) showed a significantly smaller nucleus area, both in directly fixed AMCM and in AMCM cultured for 24 h compared to WT AMCM. In addition, the roundness as an indicator for the flattening of the nuclei significantly decreased in WT-AMCM, but not in HET- or KO-AMCM over time (Fig. 30).
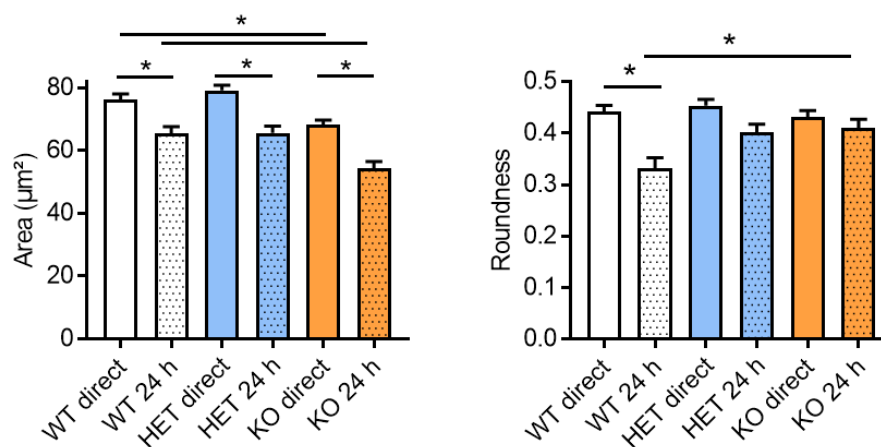
Fig. 30: Influence of p63RhoGEF deletion on nucleus morphology in AMCM.
Cardiomyocytes were isolated from 10-20 week old male mice. Cells were either fixed after 1 h (direct) or after 24 h in culture. Subsequently, cell nuclei were stained with DAPI. For quantification of the nucleus area and the nucleus roundness the ImageJ wand tool and function analyze particle were used. Parameters were measured in fluorescence images with 20x magnification (means ± SEM, n=6 ,≥74 cells *p<0.05).

To investigate if the observed changes in the KO-AMCM reflect the morphology of these cells in the myocardium, cell dimensions were analyzed in paraffin-embedded tissues, which were a kind gift of Dr. Anita Ongherth. The diameter of the cardiomyocytes was determined in tissue areas showing a cross section of cardiomyocytes. Based on the obtained area and perimeter data, the diameter of the cells was determined for better comparison. Similar as shown for the depth of the isolated AMCM, the mean diameter of KO-AMCM was significantly smaller when compared to the diameter of WT-AMCM (Fig. 31 A). Next, the size of the nuclei was analyzed in tissue areas showing a longitudinal section of cardiomyocytes. Cardiomyocyte nuclei were identified based on their localization with the help of the FITC-WGA stain as well as by their characteristic DAPI pattern (Fig. 31 B). As shown in Fig. 27 a cardiomyocyte nucleus is

characterized by its chromatin ring at the periphery and the strong DAPI-positive clusters inside the nucleus [158].
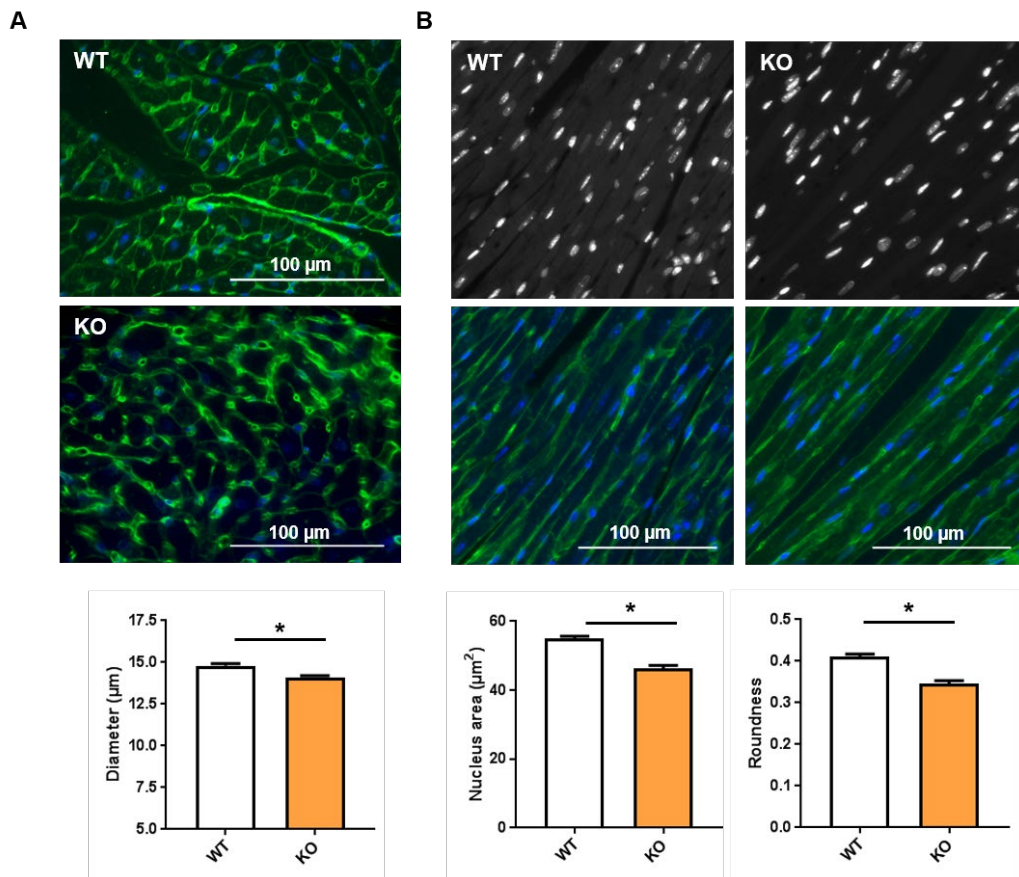
Fig. 31: Influence of p63RhoGEF deletion on cell and nucleus morphology of AMCM in the myocardium.

Hearts from 12 to 14 weeks old male wildtype (WT) and p63RhoGEF knockout (KO) mice were isolated, fixed, paraffin-embedded and cut in 7 μm thick sections. The sections were stained with FITC-labeled wheat germ agglutinin (WGA) and DAPI. Fluorescence imaging was performed. **A)** Representative cross-sectional merged images of the heart sections are shown. The cardiomyocytes were encircled in ImageJ, and based on the obtained areas and perimeters, the diameters of the cardiomyocytes were calculated. In total 800 to 1200 cells from 8 to 10 mice per group were analyzed. Given are the values as means ± SEM, *$p < 0.05$ assessed by unpaired t-test. **B)** Representative longitudinal DAPI (gray scale) and merged images of the heart sections are shown. The nuclei of the cardiomyocytes were identified due their localization and typical morphology and were encircled in ImageJ. The areas and corresponding roundness values are given as means ± SEM. In total 350-450 cells from 8 to 10 mice per group were analyzed, *$p < 0.05$ assessed by unpaired t-test.

4.9 Influence of the genetic deletion of p63RhoGEF on RhoA activity in adult mouse cardiomyocytes

Next, basal RhoA activity was investigated in freshly isolated AMCM from all three genotypes. With the help of a biochemical RhoA activation assay and by immunoblotting active RhoA, total RhoA and calsequestrin were analyzed. Both, active RhoA and total RhoA were normalized to calsequestrin, and active RhoA to total RhoA. In KO-AMCM a significant increase of more than 50% of active RhoA was found compared to WT- and HET-AMCM, when normalized by calsequestrin. Additionally, total RhoA showed a gradual and significant increase of up to 80% in KO-AMCM when normalized by calsequestrin. Thus, the ratio of active RhoA to total RhoA was unchanged in HET- and KO-AMCM compared to WT-AMCM (Fig. 32 A). In parallel, active RhoA levels were investigated by immunofluorescence analysis. Confocal center view images were prepared and the fluorescence at the sarcolemma and inside the cell measured. Similar as found by biochemical analysis, an increase in of around 50% was found at the sarcolemma of KO-AMCM. The little amount of active RhoA in the intracellular compartment was not change. To further validate this increase, the percent change of active RhoA at the sarcolemma and in the intracellular space was calculated, confirming the increased amount of RhoA-GTP at the sarcolemma in KO-AMCM (Fig. 32 B).
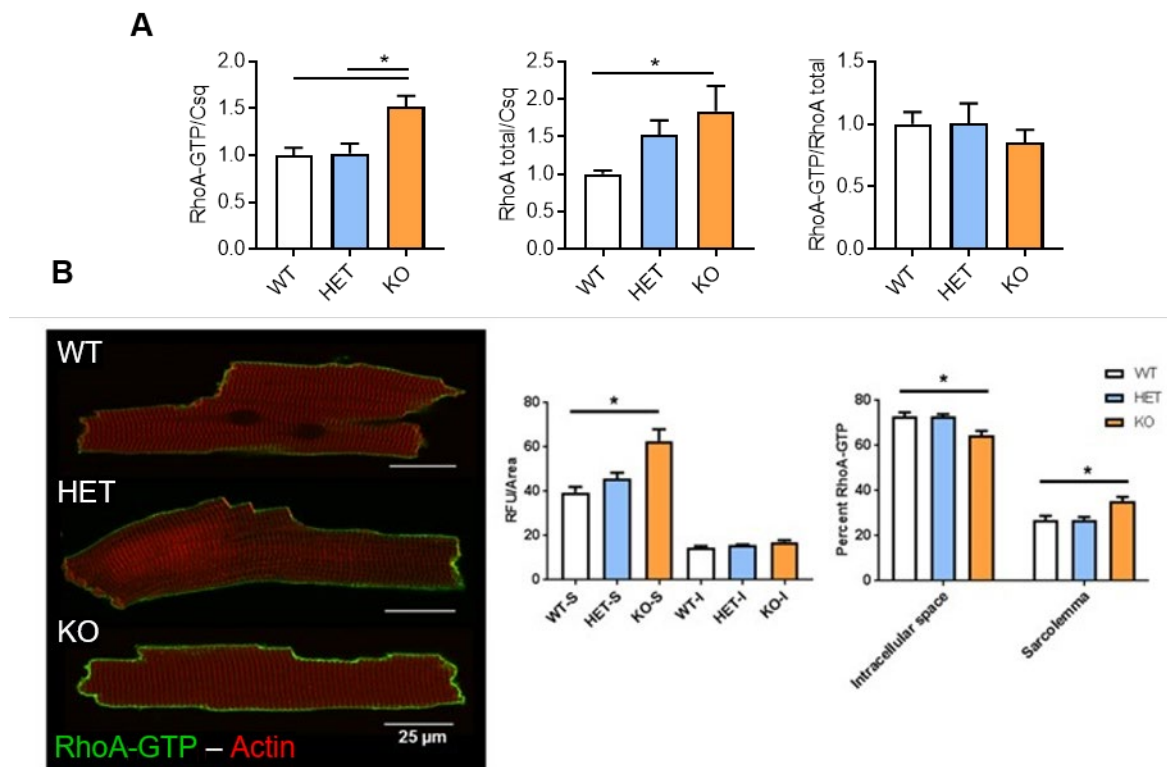
Fig. 32: Influence of p63RhoGEF deletion on the basal level of active RhoA in AMCM.

Freshly isolated AMCM from wildtype (WT), heterozygous (HET) and homozygous (KO) male p63RhoGEF knockout mice were used for the analysis. **A)** AMCM were directly stored after isolation at -80°C as pellet. RhoA-GTP levels were determined by the G-Lisa activity assay. Calsequestrin and total RhoA expression was determined in cell lysates by immunoblot analysis. Mean values of RhoA-GTP normalized to calsequestrin (left) and total RhoA (right), as well as of total RhoA normalized to calsequestrin (middle) were calculated. Data are presented as means ± SEM, n=3, *p<0.05. **B)** AMCM were directly fixed after isolation. Active RhoA (green) was detected with the anti-RhoA-GTP antibody (green) and actin with TRITC-labeled phalloidin (red). Confocal center view imaging was performed. Representative images are depicted. Active RhoA levels at the sarcolemma (S) and in the rest of the cell (I) were quantified and are given normalized to the area (left). The distribution of the total cell signal was calculated for the sarcolemma and the intracellular space (right). In total 15 cells per genotype were analyzed. The values are given as means ± SEM, n=3, *p<0.05.

Continuing the investigation of p63RhoGEF-dependent effects, cardiomyocytes from WT, HET and KO mice were isolated and cultured for 24 h, treated with the GPCR agonists ET-1, PE and AngII for 90 sec, and immunostained for active RhoA. Imaging was performed in two magnification steps. In the first step, the overall cellular activity of RhoA was imaged with a 10x objective (Fig. 33 A). In the second step, single cell RhoA activity was observed with a 63x objective resulting in 800 nm thick layers of the cell center plane (Fig. 33 B).

In wild-type AMCM, a significant RhoA activation with GPCR agonists was found in response to all three treatments as revealed by analysis of the 10x overview images (Fig. 33 A). The most efficient activation was induced by ET-1 application in this set of experiments. ET-1 treatment was also sufficient to induce RhoA activation inside the cells (Fig. 33 B). Interestingly, none of the GPCR agonist was able to induce RhoA activation in the HET- and KO-AMCM (Fig. 33 A, B). Similar as found in TAC-AMCM as well as in MβCD-treated AMCM, ET-1 and PE application led to a reduction in RhoA activation in HET- and KO-AMCM, at least when 10x overview imaging was performed. Moreover, the increased basal RhoA activity in KO-AMCM seemed to be preserved during the culture (Fig. 33).
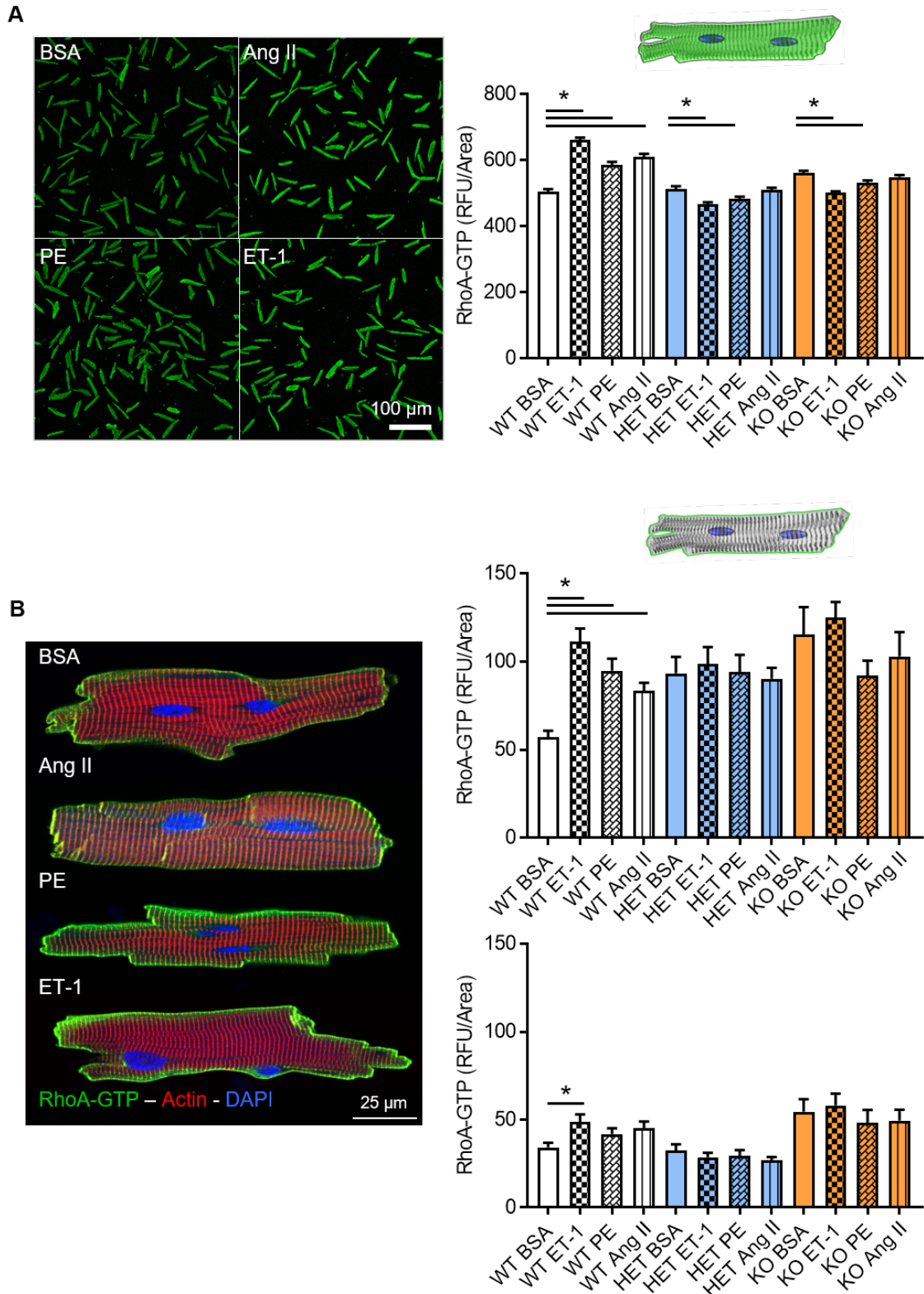
Fig. 33: Analysis of RhoA activation in AMCM with p63RhoGEF deletion.

AMCM were isolated from 10-20 week old male wild-type (WT), heterozygous (HET) and knockout (KO) mice and cultured for 24 h. Then the cells were treated with ET-1, PE or AngII for 90 sec. For control, AMCM were treated with BSA for 90 sec. After fixation, cells from all groups were stained for RhoA-GTP (green) and actin (red) as well as with DAPI (blue). **A)** Representative confocal 10x overview images (left) of RhoA-GTP of treated WT-AMCM are

shown. Bar graphs (right) summarize average values of the determined RhoA-GTP intensities per area. Data are shown as means ± SEM, n=3, 259-390 cell per group, *p< 0.05. Scale bar: 100 μm. **B)** Representative confocal 63x center view images (left) of treated AMCM stained for RhoA-GTP (green), F-actin (red) and cell nuclei (blue) are presented. Scale bar 25 μm. Bar graphs on the right show the quantification of the mean RhoA-GTP fluorescence per area ±SEM at the sarcolemma (top) and in the cytosol (bottom), n≥3 mice, ≥ 18 cells per group, *p < 0.05.

4.10 Influence of the genetic deletion of p63RhoGEF on the regulation of membranous structures

As by overexpression of p63RhoGEF, changes in the distribution of caveolin-3 were identified, the impact of the p63RhoGEF deletion was studied next. For that purpose, AMCM of all three genotypes were isolated and fixed directly after one hour of culture. Immunostaining of the cells for caveolin-3 and DAPI was performed (Fig. 34). Analysis of the caveolin-3 distribution at the sarcolemma and in the intracellular space showed no significant changes between the different genotypes (Fig. 34 A). After ImageJ processing and extraction of the membrane system, the orientation of caveolin-3 positive membranes were analyzed. Representative confocal images (top) and extracted skeleton (below) showed no visible differences between the different genotypes (WT, HET, KO). In the confocal images and the membrane distribution analyzed here, transversal elements were more strongly represented than longitudinal elements for all three genotypes. These data match the obvious transversally striated pattern which is typical for confocal images of AMCM and represents the T-tubule system (transverse tubules) while longitudinal tubules are less frequent in confocal images of AMCM. Furthermore, the composite of the averaged peak values (0°±10°, 90°±10°) showed no significant change between the different genotypes (Fig. 34 B).
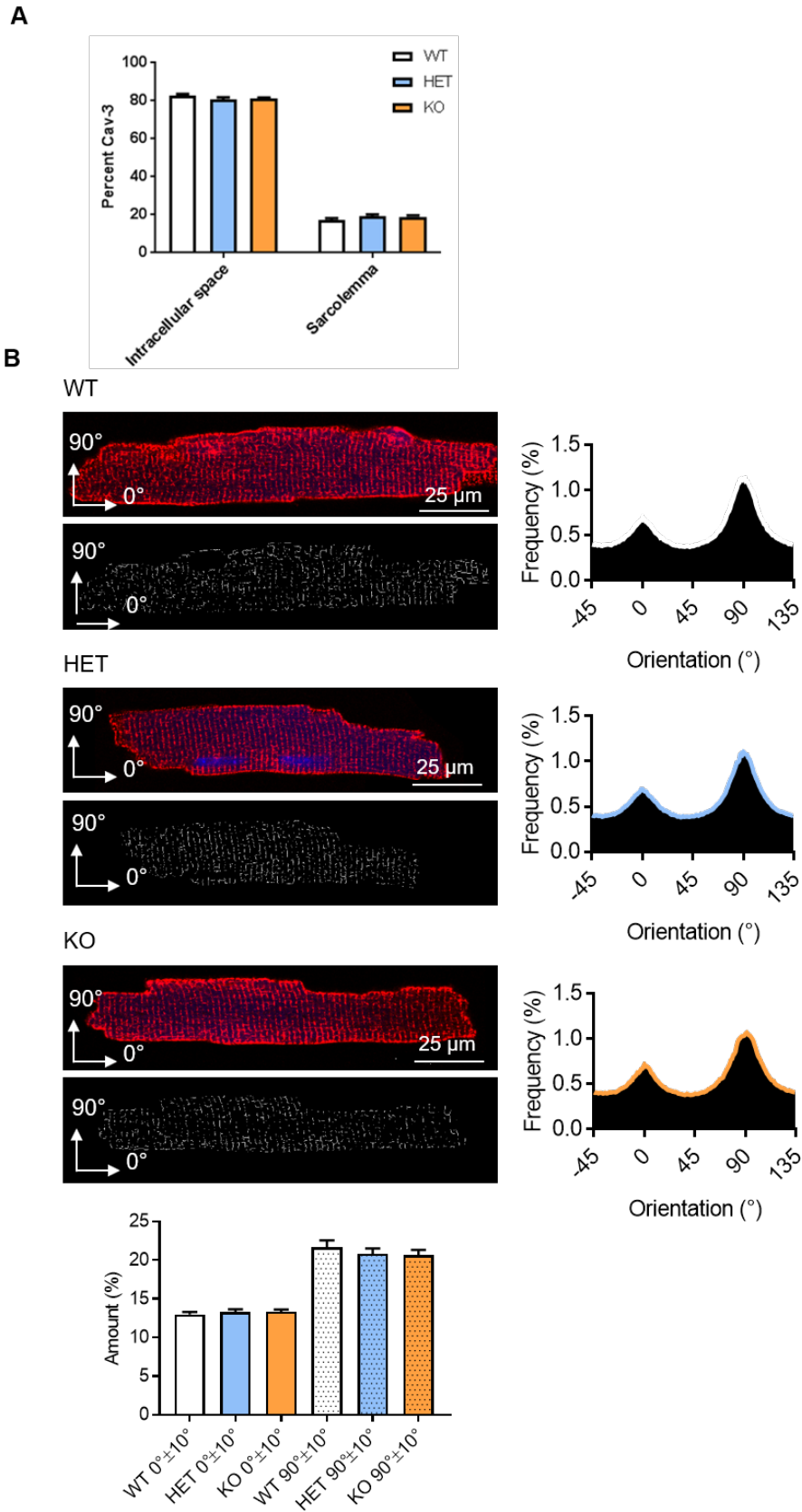
Fig. 34: Influence of p63RhoGEF deletion on the caveolin-3 localization in transverse and longitudinal tubules in AMCM.

Analysis of the caveolin-3 distribution in transverse and longitudinal tubules in isolated cardiomyocytes from 10-20 week old male, wildtype (WT), heterozygous (HET) and knockout (KO) p63RhoGEF mice was performed. Cells were seeded on laminin coated glass coverslips in adequate amount and fixed after 1 h in culture. Confocal center view images were taken. **A)** The distribution of caveolin-3 at the sarcolemma and in the intracellular space was determined and is given in percent of the total signal. **B)** Representative confocal images show immunostaining for caveolin-3 (red) together with DAPI (blue) to visualize nuclei. Caveolin-3 images were processed with ImageJ to extract the membrane system (below) and used for further analysis (right) of the orientation. The obtained values for the distribution of caveolin-3 (A) as well as of the tubular orientation with 0°±10° (longitudinal tubules) and 90°±10° (transverse tubules) (B) are given as means ± SEM, n=3, 15 cells per condition.

As the overexpression of p63RhoGEF led to an increase in the Golgi apparatus particle number (Fig. 24), the impact of its deletion on the Golgi apparatus was studied next. AMCM from WT and p63RhoGEF-KO mice were isolated and the cis-Golgi protein GM-130 was detected by confocal immunofluorescence analysis (Fig. 35 A). By particle analysis, it could be demonstrated that in isolated AMCM the complete loss of p63RhoGEF resulted in a decrease in particle number as well as in particle size. The mean GM-130 signal was lower and the distribution analysis of GM-130 suggested that the fewer and smaller Golgi apparatus particles in KO-AMCM are slightly more confined to the perinuclear region (Fig. 35 B).
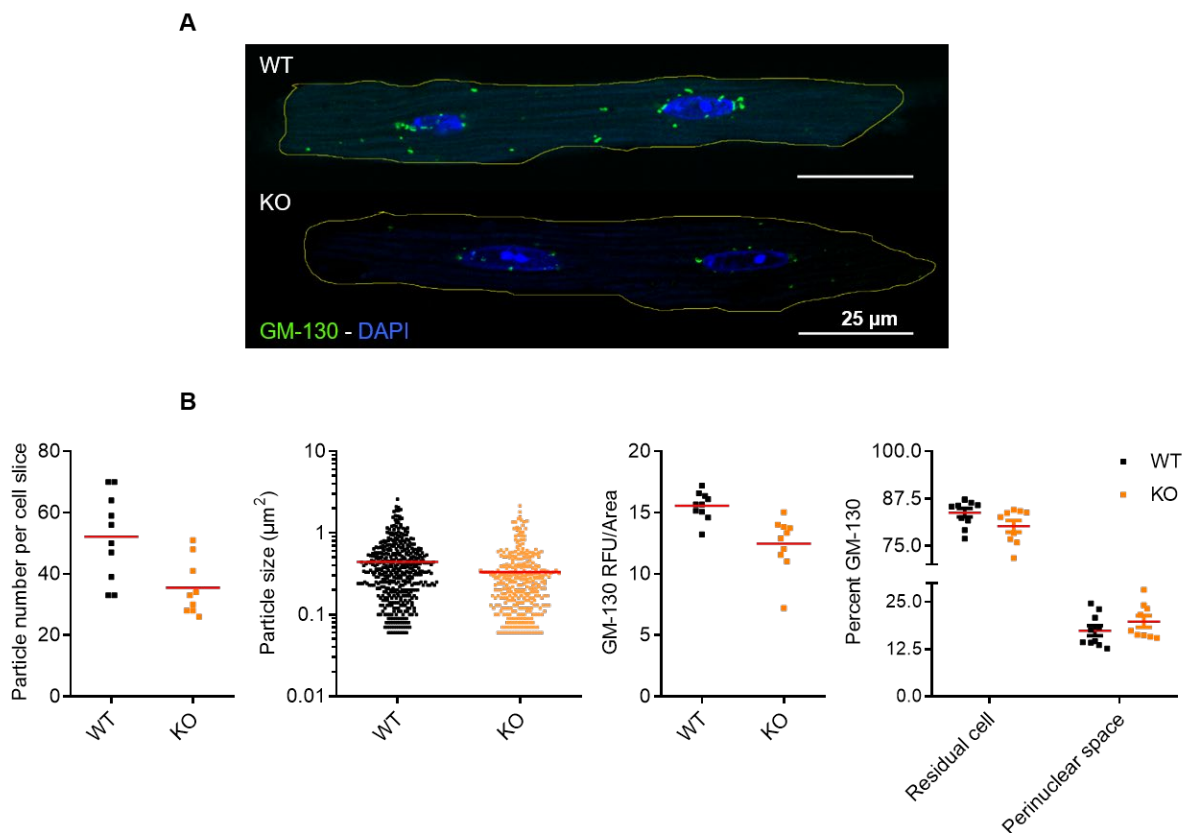
Fig. 35: Influence of p63RhoGEF deletion on the Golgi apparatus morphology in AMCM.

Isolated adult mouse wildtype (WT) and p63RhoGEF knockout (KO) cardiomyocytes (AMCM) were cultured and then immunostained for GM-130. **A)** Representative center view confocal images are shown as overlays of GM-130 (green) and DAPI (blue). The cell borders had been marked (yellow line) in ImageJ for better comparison. **B)** Analysis of the Golgi particle number (left) and the particle size (left middle) was performed with the help of the particle analysis tool of ImageJ. The intensity (right middle) and distribution (right) of GM-130 was analyzed by its fluorescence in the perinuclear region (selection of the nuclei with 2.5 µm enlargement) and in the rest of the cells. In total 10 cells per group were analyzed. The obtained values are shown individually, the means are indicated. Scale bar 25 µm.

Due to the opposing effects of p63RhoGEF overexpression and deletion on the Golgi particle number, changes in the Golgi apparatus in TAC- compared to sham-AMCM were analyzed. This investigation was based on our previous finding that p63RhoGEF expression was increased in wildtype TAC hearts (refer to chapter 2, preliminary results). Therefore, sham- and TAC-AMCM were isolated and the cis-Golgi protein GM-130 detected by confocal immunofluorescence analysis (Fig. 36 A). In line with the identified role of p63RhoGEF in the regulation of the Golgi particle number, an increase in Golgi particle number could be determined in isolated TAC-AMCM. The particle size as well as the distribution of GM-130 was unchanged (Fig. 36 B).
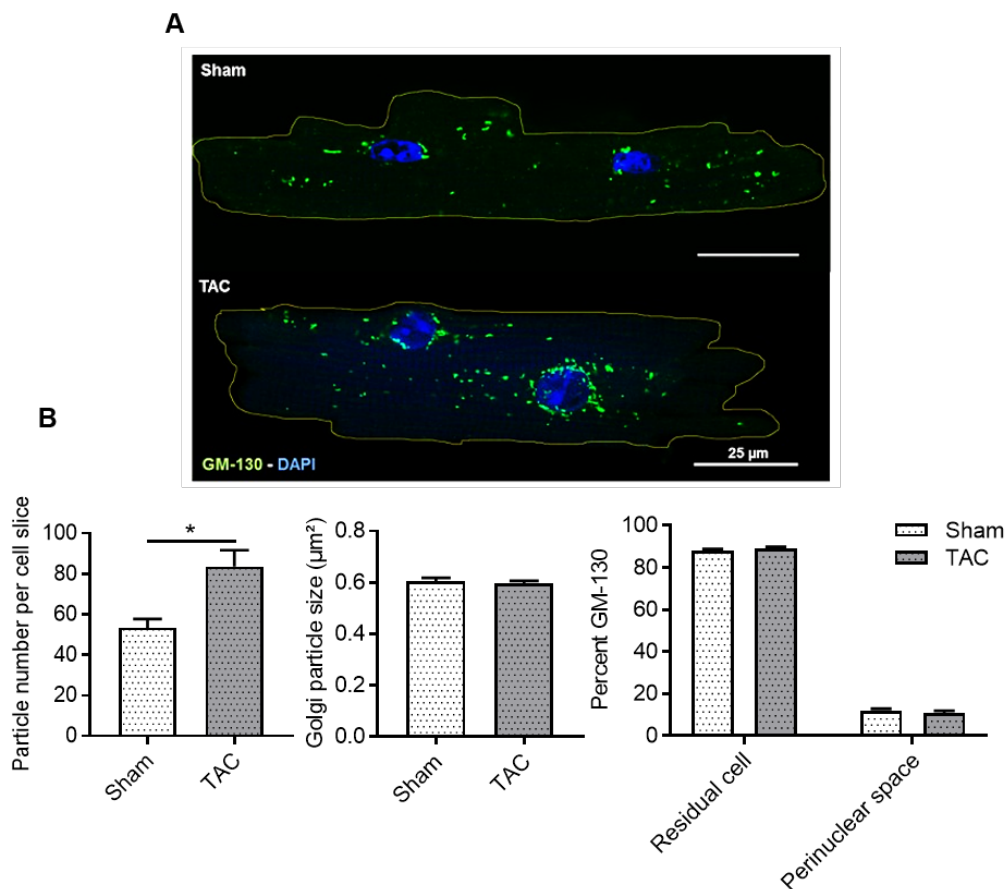
Fig. 36: Influence of TAC on the Golgi apparatus morphology in AMCM.

Adult mouse cardiomyocytes (AMCM) were isolated from animals 4 weeks after sham or transverse aortic constriction (TAC). The cells were cultured and then immunostained for GM-130. **A)** Representative center view confocal images are shown. Representative center view confocal images are shown as overlays of GM-130 (green) and DAPI (blue). The cell borders had been marked (yellow line) in ImageJ for better comparison. **B)** Analysis of the Golgi particle number (left) and the particle size (right) was performed with the help of the particle analysis tool of ImageJ. The distribution (right) of GM-130 was analyzed by its fluorescence in the perinuclear region (selection of the nuclei with 2.5 µm enlargement) and in the rest of the cells. In total 25 cells from 3 different animals per group were analyzed. Values are given as means ± SEM, *p>0.05. Scale bar 25 µm.

Finally, the size and shape of cell nuclei of sham- and TAC-AMCM were studied. Opposite to the observed changes in nucleus area in KO-AMCM, TAC-AMCM displayed an increase in the mean nucleus size. The shape of the nuclei was however unaltered (Fig. 37).
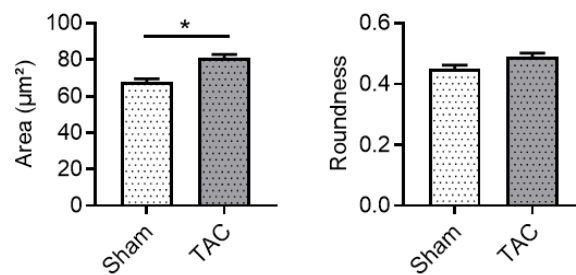
Fig. 37: Influence of TAC on the nuclear morphology in AMCM.

Adult mouse cardiomyocytes (AMCM) were isolated from animals 4 weeks after sham or transverse aortic constriction (TAC). The cells were cultured and then DAPI stained. The mean nucleus area (left) as well as their roundness (right) were quantified. Given are the means ± SEM, n=3, 120-180 cells per group in total, *p>0.05.

5. Discussion

5.1 Characterization of the GPCR-induced RhoA activation and localization in isolated adult mouse cardiomyocytes

The monomeric G protein RhoA is an ubiquitously expressed protein having its main function in the modulation of the actin cytoskeleton in most cell types. In muscle cells, its role is best understood in smooth muscle cells. In these cells, RhoA acts as a regulator of contraction by augmenting the phosphorylation of the myosin light chain via its downstream signaling [106, 159]. In striated muscle cells, however, there is still a lack of knowledge on its regulation and function, especially in the highly differentiated adult myocytes.

With respect to cardiomyocytes, the role of RhoA had so far only been investigated in immature neonatal cells and in complex mouse models. Therefore, one aim of this thesis was to characterize the localization and activation of RhoA in isolated healthy and diseased adult cardiomyocytes. To address this aim, isolated adult mouse cardiomyocytes were used from healthy and pressure-overloaded hearts, and RhoA activity and localization were assessed by confocal immunofluorescence analysis with the help of an antibody recognizing the GTP-loaded conformation of RhoA. The obtained results were exemplarily confirmed by biochemical analyses. In order to study the activation of RhoA, important cardiovascular GPCRs were activated which have been shown in the past to induce RhoA activation in neonatal cardiomyocytes and to play a role in pathological cardiac remodeling.

The standard method to analyze RhoA activity uses a RhoA-binding domain (RBD), which specifically binds GTP-loaded RhoA. This biochemical assay can be performed with the help of a rhotekin-RBD fusion protein coupled to glutathione-S-transferase in a so called pulldown experiment with subsequent immunoblot analysis [160], or with a RBD-construct immobilized on a membrane with subsequent immunodetection of RhoA (commercially available G-Lisa system). A clear disadvantage of these biochemical approaches is their inability to give information on the spatial distribution of the RhoA activation in a certain cell type. Thus, in this thesis a monoclonal antibody was used, which recognizes the confirmation of GTP-loaded RhoA, combined with high resolution confocal imaging. This antibody has so far mostly been used to precipitate GTP-loaded RhoA from cell lysates and thus serves as an alternative to the RBD-based methods [161, 162]. Only rarely, the antibody was used for immunocytochemistry [151, 163]. Therefore, the initial results obtained with this antibody with respect to the localization and activation of RhoA in adult mouse cardiomyocytes were confirmed by

biochemical analyses to exclude experimental artifacts. Moreover, human adult atrial cardiomyocytes were used to confirm the localization of active RhoA detected in the mouse cardiomyocytes.

Localization and activation of RhoA in healthy adult cardiomyocytes

In summary, the data obtained in this thesis demonstrate that active RhoA is predominantly located at the sarcolemma in adult cardiomyocytes. This localization is species-independent as it was similar in mouse ventricular and human atrial cells (Fig. 5, Fig. 18). In some cells, a moderate accumulation of active RhoA in the former regions of the intercalated discs was detected (Fig. 5). By the staining of rarely occurring cell doublets, this localization could be confirmed (Fig. 5 E). In many but not all cells, a thin striated pattern of active RhoA was found inside the cell, which however, was only marginal compared to the strong sarcolemmal localization. To rule out any unwanted side-effects and damage due to cultivation, directly fixed AMCM and AMCM after 24 h in culture were compared (Fig. 7). While the faint sarcomeric pattern did not change, the intensity of the RhoA-GTP signals on the sarcolemma increased after 24 h in culture, indicating that RhoA activity might be initially suppressed by the cell isolation procedure or later activated due to the cell culture conditions. That active RhoA is associated to the plasma membrane via its C-terminal isoprenoid-group is a well-known fact and has been initially used to determine the activation status of the GTPase by analyzing its cytosol/membrane ratio [164]. In more recent publications, this activity dependent localization of RhoA had been confirmed with the help of FRET-based biosensors [165, 166]. Inactive RhoA mainly resides inside the cell, as its isoprenoid-group is covered by RhoGDI proteins [167]. In accordance, by using an antibody directed against a specific RhoA-epitope and not a certain RhoA confirmation, a predominant intracellular, sarcomeric localization in AMCM was detected (Fig. 5). Surprisingly, there was no overlap between the total RhoA and the active RhoA signal. A possible explanation could be the insensitivity of the total RhoA antibody. Indeed, by lysing the AMCM with a low stringent buffer containing sufficient detergent to solubilize the membranes, but insufficient salt to dissolve the sarcomere, the majority of RhoA was found in the insoluble fraction together with the sarcomeric protein α-actinin (Fig. 9). This suggested that only a very minor fraction of RhoA is active in adult cardiomyocytes. Alternatively, the total RhoA antibody might not detect membrane-associated active RhoA. This antibody was generated against an epitope which is located near the C-terminus of RhoA. Whether this might interfere with the conjugated isoprenoid group at the C-terminus and/or the membrane attachment is not clear.

To study the activation of RhoA in AMCM, three different ligands for GPCRs were used in this study: Endothelin-1 (ET-1) and angiotensin II (AngII) as well as the synthetic α-adrenoceptor agonist phenylephrine (PE). Based on our own data (preliminary results) and data from other groups, all three ligands were found to activate RhoA signaling in neonatal rat cardiomyocytes (NRCM) [117, 119]. Moreover, the signaling elicited by the corresponding GPCRs had been demonstrated to be involved in the pathogenesis of heart diseases, with the AngII type 1 receptor being one of the most important pharmacological targets [168-170]. So far, the activation of RhoA by these ligands had not been demonstrated in adult cardiomyocytes. Therefore, a combination of ET-1 and PE was initially used in order to achieve maximal effects. AngII was not implemented in this pilot analysis due to its low effect on the RhoA activity in NRCM (Fig. 1, previous results). The impact of ET-1 and PE on cardiomyocyte signaling was investigated in three different ways. First, the phosphorylation of ERK1/2 as known downstream targets of ET-1 and PE was investigated [171, 172]. Second, the activation of RhoA was determined with the G-Lisa system, and third, the change in the active RhoA signal was assessed by confocal imaging with the help of the active RhoA antibody. Consistently, 90 sec after addition of ET-1/PE an increase in ERK1/2 phosphorylation (Fig. 9 D) and an activation of RhoA in both experimental settings were found (Fig. 9 A). The advantage of the microscopic approach became obvious by the analysis of surface view images (Fig. 10). The amount of active RhoA was not simply increased at the sarcolemma, the protein also underwent a redistribution. In non-treated cardiomyocytes, active RhoA was detected in a moderate regular striated pattern with a striation width of around 0.9 μm. After application of the combination of ET-1/PE or of the single ligands, more cells displayed a pattern with a more pronounced signal width of 1.8 μm. By co-detection of the costamere via fluorescently-labeled phalloidin and of the M-band associated myomesin, it became clear that especially the active RhoA in or close to the costamere increased. Analysis of the cell morphology excluded that this effect was based on cell shrinkage or other morphological disturbances (Fig. 8).

The costamers of cardiomyocytes have several important functions. They link the sarcomere via its outermost Z-disc to the sarcolemma, they hold focal adhesion complexes which are important for cell-matrix interaction, and they are hot spots of mechanosignaling (reviewed in [173]). A central protein in the costamere is dystrophin [174]. In order to determine the exact localization of active RhoA, co-localization analysis of dystrophin and active RhoA was performed (Fig. 5). Surprisingly, both proteins resided in different compartments at the sarcolemma, which would argue against a costameric localization of active RhoA. However, in the initial description of costameres in cardiomyocytes presented by Pardo and colleagues, the organization of these structures were described as rib-like bands above the Z-disc [175]. This was not the case for the localization of dystrophin in the investigated AMCM. Here,

dystrophin showed a dotted irregular pattern, which was not confined to the Z-disc (Fig. 5). In contrast, activated RhoA was organized in a rib-like pattern with increasing intensities above the Z-disc upon GPCR activation (Fig. 8, Fig. 10). Further analyses are needed to clarify the exact localization of active RhoA in this sarcolemmal region.

Another important signaling hot spot in cardiomyocytes are caveolae. In these flask-shaped invaginations in the outer sarcolemma and in the transverse and longitudinal tubular system of cardiomyocytes, important signal components are clustered allowing their tight control [61, 176]. In neonatal cardiomyocytes, the role of caveolae for RhoA regulation had already been demonstrated. Anastasi and colleagues showed that the disruption of caveolae by cholesterol-depletion with methyl-β-cyclodextrin (MβCD) resulted in a blunted RhoA activation in response to stretch in NRCM. Moreover, they demonstrated that a substantial amount of RhoA is located in caveolae [49]. Comparable effects were described for the leptin-induced RhoA activation in NRCM. Interestingly, in this work the authors demonstrated that RhoA was absent from the caveolae without leptin and translocated into the caveolae within 5 min after leptin application [177]. Based on these findings, and the different patterns observed for dystrophin and active RhoA, the co-localization of active RhoA and caveolin-3 at the surface of AMCM was investigated (Fig. 6). However, the determined co-localization coefficients for both proteins were rather low. In summary, caveolin-3 showed a slightly better correlation with active RhoA than vice versa. The determined Pearson correlation coefficient was ~0.1, arguing against a general co-localization of both proteins.

Localization and activation of RhoA in diseased adult cardiomyocytes

As mentioned above, an important part of this thesis was to compare RhoA signaling in healthy and diseased cardiomyocytes. As a model system, murine adult cardiomyocytes were used, which offer the possibility to study healthy and diseased cardiomyocytes with the same genetic background. Moreover, the usage of mice as cell donors has the advantage of obtaining cardiomyocytes with a defined cellular disease phenotype. In this study, mice were subjected to transverse aortic constriction (TAC) which initially led to compensated hypertrophy and subsequently to decompensated heart failure as demonstrated by the reduction in the contractile performance and the ventricular dilation (Fig. 11). Moreover, the isolated cardiomyocytes were significantly thicker and longer compared to sham cells (Fig. 12), indicating that decompensated, eccentric hypertrophy was present at the end of the TAC experiment [178]. The TAC model was also chosen because RhoA had been demonstrated to be chronically activated in TAC hearts. Increased RhoA activation was found as early as 24 h

after TAC and lasted at least for up to one year [114]. Thus, the TAC model combined the advantages of a controlled disease progression with a relatively low mortality, and a very broad time window in which the pathological change in RhoA activity occurred. Importantly, the feasibility of using isolated adult cardiomyocytes to analyze disease-dependent changes in signal transduction had been demonstrated by others before [87, 179].

One goal of this part of the thesis was to obtain insight into the currently unknown localization of active RhoA in diseased cardiomyocytes. Confocal imaging and analysis of its pattern regularity revealed that together with the patterns of dystrophin and caveolin-3, also the pattern of active RhoA became less organized at the surface of AMCM four weeks after TAC (Fig. 14). As all three proteins were found to reside in different membrane compartments, this finding argues for a general disturbance of the sarcolemmal organization in diseased cardiomyocytes. This is in line with data on the distribution of dystrophin and on the general topography of the sarcolemma in diseased cardiomyocytes. For dystrophin, an abnormal distribution had been described in the diseased human myocardium with a loss of the normal punctate pattern at the sarcolemma [180]. Data obtained by scanning ion conductance microscopy revealed that in diseased human and rat cardiomyocytes a loss of the TT and Z-groove organization of the sarcolemma occurred [57, 61].

Besides the differences in RhoA localization and regularity, the ability of the different GPCR agonists to activate RhoA was significantly altered in AMCM after TAC. First, the basal activity of RhoA in TAC-AMCM was significantly higher as in sham-AMCM. This increase was not due to an increase in cell size, as all values were normalized to the cell area, and also not due to an increase in RhoA expression (Fig. 16). In contrast, a reduction in the total amount of the protein was found. Previous studies suggested that RhoA expression is increased in the diseased heart [181, 182]. However, individual cell type analysis was never performed before. In the diseased heart, a change in the cellular composition takes place, e.g. the number of myofibroblasts increases, which express high levels of RhoA [183]. Second, the application of the GPCR ligands did not induce any further augmentation of the RhoA activity. In contrast, ET-1 and PE even decreased the activity of RhoA after TAC (Fig. 15). Although, at the current status this cannot be finally explained, different mechanisms can be proposed. First, the corresponding receptors are desensitized in the setting of TAC due to the high neurohumoral stimulation. This is a well-known phenomenon, which has been demonstrated before for the AT1R, the α-adrenergic as well as the endothelin-1 receptors in cardiomyocytes [184-186]. Second, the disturbances in the membrane organization disrupt the corresponding signaling complexes, which has been nicely documented for the $α_2$-adrenoceptor [87]. Third, changes in the expression of accessory RhoA regulators occurred. A potential candidate in this scenario

is the RhoA-specific p190B-RhoGAP (alias ARHGAP5). According to preliminary RNA sequencing data from our lab, this GAP is strongly downregulated in hearts from mice after TAC and might thus explain the unleashed RhoA activity.

To further study the mechanisms underlying the changes in RhoA activity and activation in TAC-AMCM, the effect of the cholesterol-depleting reagent MβCD was investigated. Interestingly, this led to the same increase in basal RhoA activity as found in the TAC-AMCM (Fig. 17), although active RhoA did not reside in caveolae in AMCM. Moreover, the application of ET-1 to the cells resulted in the same decrease in RhoA activity as in the TAC-AMCM (Fig. 17 C). These data clearly argue that the disturbance of the sarcolemmal organization is a likely explanation for the changes observed in TAC-AMCM and MβCD-treated AMCM. The desensitization of the ET-1 receptor can be ruled out as a cause in the MβCD-treated AMCM.

5.2   Characterization of the localization of the guanine nucleotide exchange factor p63RhoGEF in isolated adult mouse cardiomyocytes

The guanine nucleotide exchange factor p63RhoGEF was first identified by Souchet and colleagues in 2002. By Northern blot analysis , they and others demonstrated that this GEF is expressed in the human heart and brain [144, 187]. Later studies revealed that the protein is also expressed in other tissues like the vasculature [149, 150].

In the initial characterization of p63RhoGEF, its localization was studied in the human myocardium and a sarcomeric, I-band associated localization was postulated [187]. In a later study, p63RhoGEF was found predominantly at the sarcolemma and in fine intracellular striations in the adult mouse myocardium [142]. In order to verify the localization of p63RhoGEF in AMCM and due to the lack of available antibodies recognizing the native protein in immunocytochemical studies, an adenoviral overexpression approach was used. The human 580 amino acid p63RhoGEF variant as well as the N-terminally truncated p63ΔN construct were overexpressed in AMCM and their localization was studied by confocal imaging based on the additional N-terminal c-myc-tag. The truncation of p63RhoGEF by the first 294 amino acids (p63ΔN) has two consequences for the function of the protein. One lays in the missing cysteine stretch in the N-terminus, which is found in the 580 amino acid full length protein. This stretch was demonstrated to be modified by S-palmitoylation leading to the membrane attachment of p63RhoGEF [136]. Moreover, in p63ΔN most of the catalytic DH-domain is missing. As the C-terminal extension of the PH domain is present in this construct,

p63ΔN is still able to interact with active Gα$_q$ and functions downstream as a dominant negative molecule, not only for RhoA but also for other Gα$_q$-elicited pathways [154].

In general, the localization of both proteins was dependent on the transduction efficiency of the AMCM. In cells with a lower expression, full length p63RhoGEF localized mainly in the perinuclear region and in randomly distributed intracellular speckles. When the protein was higher expressed, an additional strong sarcolemmal association was found (Fig. 19 A). This difference in low and high expressing cells could also be interpreted as a time-dependent effect as the onset of p63RhoGEF expression in highly transduced cells is faster than in lowly transduced. This would mean that p63RhoGEF is first targeted to the membrane system in the perinuclear region, then becomes palmitoylated there, and is finally transported outward to the sarcolemma. How p63RhoGEF gets palmitoylated is completely unknown. More than 20 mammalian palmitoyltransferases had been identified based on their sequence, which localize either in the membranes of the endoplasmic reticulum, the Golgi apparatus or in the plasma membrane [188]. None of these proteins had been investigated in cardiomyocytes so far.

However, the importance of the palmitoylation of p63RhoGEF can be appreciated by comparing its localization with the one of p63ΔN. This construct mainly resides in the sarcomere in low expressing cells and in high expressing cells an additional prominent localization in the region of the former intercalated disc occurred (Fig. 19 B). The latter is rather unexpected as this accumulation could only be due to protein-protein interaction and not due to membrane targeting via a lipid modification. Why full length p63RhoGEF did not show an accumulation in the intercalated disc is not clear, but suggests that the lipid-anchored protein might not be able to get in close contact with the potential interaction partner of p63ΔN. This raises the question for future studies whether the different p63RhoGEF splice variants, with or without palmitoylation, might have different functions in cardiomyocytes.

Although p63RhoGEF did not accumulate at the former intercalated disc, it also did not spare this region. This finding together with the localization of active RhoA in the intercalated disc (Fig. 5) indicates that this region of the cell might be of special importance with respect to RhoA signaling. In line, the intercalated disc had been suggested before to be a place of RhoA signaling by the characterization of Myozap. This protein was found in the intercalated discs of adult mouse cardiomyocytes, the adult myocardium, and was shown to be an activator of RhoA signaling in HEK293 cells and in NRCM [189, 190].

The dominant localization of full length p63RhoGEF in membranous structures was further characterized by co-localization analyses. As in caveolae palmitoylated proteins were found to be enriched [189, 191], the co-localization of caveolin-3 and p63RhoGEF was studied first

(Fig. 22). In cells with low p63RhoGEF expression the overall correlation of both proteins in center view images was low with a Pearson's coefficient of 0.3. The Manders' coefficients demonstrated that the overlap between p63RhoGEF and caveolin-3 is higher than vice versa (Fig. 22 B). This was mainly due to their common localization in the perinuclear region. Interestingly, independent of the height of the overexpressed p63RhoGEF, more caveolin-3 was found in the perinuclear region than in control-transduced cells (Fig. 22 D). This suggests that p63RhoGEF potentially influences the transport of caveolin-3 from its synthesis place at the ER to the caveolae. In cells with high p63RhoGEF expression, the overall correlation of both proteins in center view images was higher with a Pearson's coefficient of 0.7. This could be explained by their common localization in the perinuclear region and in the sarcolemma (Fig. 22 B). However, it has to be taken into account that the z-resolution in confocal imaging is always worse than the x,y-resolution. This can lead to a false-positive overlap of signals having the same x,y-positioning but localizing in a different z-depth. Therefore, surface view images were taken from the transduced cells (Fig. 22 C). In principle this bears the same problem. However, the analyzed proteins in this thesis, like active RhoA and p63RhoGEF, were dominantly located at the sarcolemma and thus the cytosolic signal noise underneath the sarcolemma was relatively low. The difference between both image modalities is nicely demonstrated by the fact that by analyzing surface view images the obtained correlation coefficients of caveolin-3 and p63RhoGEF were considerably lower than those obtained from center view images (Fig. 22 B, C). In summary, the co-localization of p63RhoGEF and caveolin-3 at the sarcolemma was not prominent. In former studies, our group had already shown that the AngII-dependent, p63RhoGEF-driven RhoA activation in smooth muscle cells could not be disturbed by the depletion of cholesterol and is thus not dependent on caveolae [150].

The first contact of membrane-associated proteins with the membranous system often takes place at the ER. In order to analyze the accumulation of p63RhoGEF in the perinuclear region, and thus in the rough ER, co-localization analyses of full-length p63RhoGEF and p63ΔN were performed together with an antibody recognizing proteins with the ER retention and targeting motif KDEL (lysine - aspartic acid - glutamic acid - leucine). This motif is found in many soluble ER proteins at the C-terminus and is detected by a family of GPCR-like receptors, the KDEL-receptors [192-194]. These receptors mainly reside in the cis-Golgi compartment and bind the escaped ER KDEL-proteins. This induces the retrograde transport of the receptor with its ligand to the ER. In the ER, the binding between the receptor and the KDEL protein is released due to the shift in the pH between the Golgi and the ER [195].

Surprisingly, in p63RhoGEF-overexpressing cells the localization of p63RhoGEF was almost completely mimicked by the anti-KDEL-antibody (Fig. 23 A). This led to positive KDEL-signals in membrane compartments where soluble KDEL-proteins normally do not reside, like in the sarcolemma. Moreover, compared to control transduced cells the overall signal intensity given by the KDEL-antibody was extraordinarily high in cells expressing either p63RhoGEF or p63ΔN. This all pointed to an experimental artefact as explanation for the more than unexpected finding. Therefore, immunoblot analyses of the transduced cells were performed with the KDEL-antibody, showing that the antibody could recognize the overexpressed p63RhoGEF constructs (exemplarily shown for p63ΔN in Fig. 23 C). The KDEL antibody used in this study (Abcam #ab176333) is supposed to recognize the six amino acid long antigen SEKDEL (serine - glutamic acid - lysine - aspartic acid - glutamic acid - leucine, personal communication with Abcam). However, it can be hypothesized that this antibody in addition recognizes the C-terminal EDEL motif of p63RhoGEF since that motif differs from the KDEL motif by only one amino acid.

Although based on this artefact, no insight was obtained on the localization of p63RhoGEF at the ER, further information could be gained on the structure of p63ΔN in the cytoskeleton and the intercalated disc. The KDEL antibody did not detect p63ΔN when it was localized at the sarcomere, only its localization at the intercalated discs was detected by the KDEL antibody. Since it is hypothesized that the KDEL antibody detects the EDEL motif of p63RhoGEF, two explanations for the observed phenomenon are possible: i) the C-terminal EDEL motif of p63ΔN is not accessible to the antibody when the protein is localized in the sarcomere; ii) the proportion of p63ΔN, which is localized in the sarcomere does not possess its C-terminus (Fig. 38). Based on former experiences with this construct the second explanation is more likely as the C-terminus of p63RhoGEF is relatively unstructured and labile [116]. Especially in truncated versions like p63ΔN it can easily break (personal communication with S. Lutz). If this explanation is correct, it can be concluded that the likelihood of the existence of a sarcomeric p63RhoGEF splice variant is low because so far, no p63RhoGEF splice variant with a missing C-terminus was characterized.
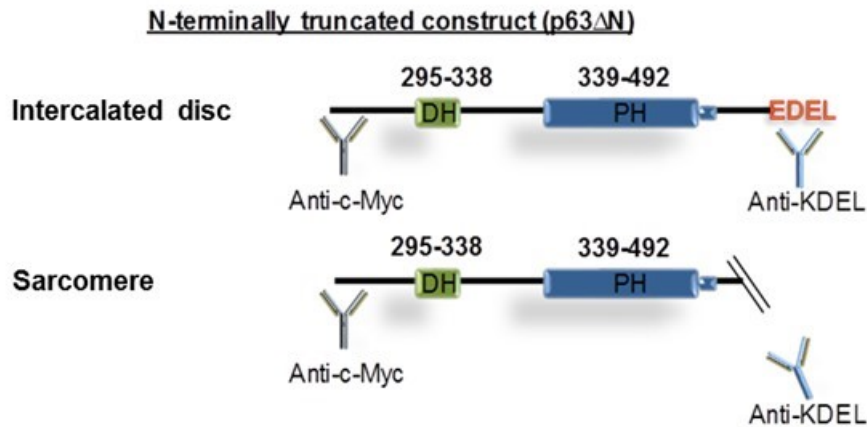
Fig. 38: Cartoon illustrating the potential binding modalities of the KDEL antibody to the N-terminally truncated p63RhoGEF.

Next, the co-localization of p63RhoGEF with the Golgi apparatus was analyzed (Fig. 24). For this, the cis-Golgi matrix protein GM-130 was detected together with full length p63RhoGEF and p63ΔN. The latter showed no co-localization with GM-130. But the full length protein and GM-130 were both found in close vicinity in the perinuclear region and in randomly distributed speckles in the cell. In general, the GM-130-containing Golgi particles, which had a mean size of around 0.6 µm^2, were rather confined independent of their localization. The overlap of GM-130 and p63RhoGEF was not prominent and the compartments in which both proteins resided appeared to be associated to each other. The knowledge on the Golgi apparatus in cardiomyocytes is surprisingly sparse. The speckled distribution had been demonstrated before in isolated rat cardiomyocytes with GM-130 as a marker protein [196]. The ultrastructure and organization of these speckles is not known. Based on the rather similar morphology of the Golgi apparatus in cardiac and skeletal myocytes, one could hypothesize that p63RhoGEF is located in the trans-Golgi network. For skeletal myocytes it was demonstrated by electron microscopy that each Golgi apparatus was a stack of three to four cisternae, with a height of around 0.7 µm. Immunolabeling revealed that these small stacks are polarized with the cis-Golgi side facing the nucleus [197]. A further argument for this hypothesis comes from one of our previous studies in cardiac fibroblasts. In these cells we could show that p63RhoGEF co-localized with the trans-Golgi network protein GOPC, but not with the cis-Golgi protein GM-130 [151]. As unfortunately, the GOPC staining in AMCM did not result in a reliable signal and the Golgi apparatus is so small in these cells, further analyses are needed with other Golgi markers and super resolution microscopy to shed light on the exact localization of p63RhoGEF in the adult cardiomyocyte Golgi apparatus.

Taken together, the localization studies performed in this thesis confirm the identified sarcolemmal-associated location of endogenous p63RhoGEF in the adult myocardium, which

had been described by Smith and colleagues [142]. Moreover, its localization at secretory endomembrane was found in AMCM similar as this was described for cardiac fibroblasts by our group [151]. The localization in the sarcomeric I-band that had been described by Souchet and colleagues could not be verified [187].

5.3 Characterization of the function of the guanine nucleotide exchange factor p63RhoGEF in isolated adult mouse cardiomyocytes

In order to get more insight into the function of p63RhoGEF in adult cardiomyocytes, three models were compared. On the one hand a gain-of-function model by adenoviral overexpression was used, on the other hand a loss-of-function model by heterozygous or homozygous knockout of p63RhoGEF was investigated. Moreover, AMCM from diseased hearts were analyzed as p63RhoGEF was found to be increased under this condition [151]. All three models clearly had their limitations. In the gain-of-function model, the culture of the adenovirally-transduced cells did not any longer allow the analysis of the RhoA activity. The used AMCM were isolated from a global, constitutive and not a cell-type specific, inducible mouse model, which can lead to adaptive processes during the development. The changes seen in TAC-AMCM are based on manifold changes in signaling and are not only due to one single signal cascade. Nonetheless, by comparing all three models, insights in the role of p63RhoGEF in adult cardiomyocytes could be obtained.

Does p63RhoGEF activate RhoA in adult cardiomyocytes?

One of the most important question in this context was if p63RhoGEF is a mediator of the GPCR-driven RhoA activation in adult cardiomyocytes. As shown in the preliminary data, in neonatal cardiomyocytes its knockdown and its overexpression resulted in a clear reduction and augmentation of the ET-1-induced RhoA activation (Fig. 1). In adult cardiomyocytes, the obtained results were much more complex. As the adenoviral transduction of the AMCM did not allow any analysis of RhoA activation, insights could only be gained by the knockout model. Here, the comparison of the heterozygous (HET) and homozygous (KO) knockout AMCM is of utmost importance. In both AMCM types, the responsiveness of RhoA to the investigated GPCR ligands was gone, which would argue for a prominent role of p63RhoGEF in the underlying signaling (Fig. 33). But in the KO-AMCM, the basal RhoA activity was increased as shown by directly fixed and cultured cells (Fig. 32). This fully mimicked the situation in TAC- and MβCD-treated AMCM and cannot be simply attributed to the role of p63RhoGEF as a

mediator of the $G_{q/11}$-dependent RhoA activation. The data indicate that p63RhoGEF has an additional effect in AMCM, which becomes only prominent by its full deletion, and is in line with the differences seen in the corresponding mouse models. Here, after TAC, a worsening of the contractile function was found only in HET-mice but not in KO-mice (refer to preliminary results). Instead the mortality of the KO-mice was tremendously increased (Fig. 3). Thus, it could be concluded that p63RhoGEF plays a role in the GPCR-induced RhoA activation in adult cardiomyocytes but has an additional effect on the signaling organization. Whether the additional function relies on a so far unclear role of p63RhoGEF in these cells, or if it is a consequence of the missing competition between p63RhoGEF and other $G_{q/11}$ signaling pathways, like the activation of phospholipase Cβ and PKC is not clear.

By comparison of data obtained in this thesis as well as of data obtained in the parallel p63RhoGEF-KO TAC study (Thesis of Dr. Anita Ongherth) with a study on the impact of the cardiomyocyte-specific deletion of RhoA during pressure overload some interesting common themes can be identified. The loss of RhoA resulted in an enhanced dilatation of the left ventricle after TAC and a worsened contractile function similar as demonstrated for the p63RhoGEF-HET mice (see preliminary results). Interestingly, the loss of RhoA resulted in an increased basal phosphorylation of PLCβ and PKC, suggesting that there is a close link between RhoA signaling and the canonical $G_{q/11}$ signaling in cardiomyocytes. After an acute stimulus of 10 min of TAC, the increased phosphorylation of both proteins was reduced, whereas it was increased in the corresponding WT animals. The authors explained this finding by a similarly directed, 2-fold change in the expression level of the phosphatase and tensin homolog (PTEN), which cleaves PIP3 into PIP2 and thus might be able to directly influence PLCβ activity [124]. However, 10 min is a rather short time for such a strong regulation of the total level of a protein. Alternatively, this could be explained by a less dominant p63RhoGEF signaling under basal conditions when RhoA is depleted, and a still possible competition of p63RhoGEF with PLCβ signaling when $G_{q/11}$ is activated. The G_q protein, p63RhoGEF and RhoA are all lipid-anchored proteins and might reside in a pre-complex at the sarcolemma [116, 198]. It was demonstrated that the complex has a certain basal activity, which is dependent on its membrane localization [136]. In case when RhoA is missing, this might lead to a preferential pre-coupling of $G\alpha_q$ to PLCβ. PLCβ and p63RhoGEF in principle interact with the same site in $G\alpha_q$, but the RhoA-p63RhoGEF-$G\alpha_q$ complex is supposed to be more offset from the membrane than the PLCβ-$G\alpha_q$ complex and thus the missing RhoA could indeed induce changes in pre-coupling and in basal signaling due to the interference with the membrane offset of $G\alpha_q$ [198]. However, upon GPCR activation, interaction of $G\alpha_q$ with p63RhoGEF could be still possible, but results in non-productive signaling as well as in a

competition with PLCβ. One further argument for a role of the missing competition between p63RhoGEF and other $G_{q/11}$ signaling pathways as a cause of the observed effects in KO-AMCM and KO-mice comes from a mouse model in which the activation of PKCα was studied for the heart function. Interestingly, the activation of PKCα caused a complete uncoupling of the β-adrenoceptors but had no impact on the heart/body weight ratio and contractile function in young mice. Moreover, PKC activation on the background of enhanced $G\alpha_q$-signaling, like in a $G\alpha_q$-overexpressing mouse, dramatically increased the mortality especially in male mice [199].

In summary this suggests that in the heterozygous p63RhoGEF knockout mice, the effects mainly rely on the diminished RhoA activation, whereas in homozygous knockouts a mixed answer of a blunted RhoA activation and an induced PLCβ/PKC activation occurred. The latter may play role in the heterologous desensitization of the GPCRs as this was e.g. demonstrated for the AT1R in NRCM [185]. But also an impaired membrane organization could account for the changes in RhoA activity in KO-AMCM, similar as in TAC and MβCD-treated AMCM.

Does p63RhoGEF play a role in the regulation of adult cardiomyocyte growth and nucleus size?

RhoA was initially proposed as a pro-hypertrophic factor in cardiomyocytes [124], but diverse mouse models argued against its role in the typical concentric heart growth. Changes in RhoA activity and expression in cardiomyocytes were either associated with a dilated phenotype [122, 124] or no with changes at all [123]. Similar results were obtained for p63RhoGEF. In the intact mouse heart, no differences in the cardiomyocyte size of the HET- compared to WT-mice was found, although the mice showed a slight ventricular dilation (Thesis Dr. Anita Ongherth). In the KO-mice, the geometry of the heart was not changed compared to WT-hearts, but the cardiomyocytes had a slightly smaller diameter (Fig. 29, 31). Isolation of these cells revealed that the KO-AMCM seemed to have also a decreased diameter, reflected by the analyzed cell depth. Culturing further decreased cell depth more pronounced in KO-AMCM than in the other two genotypes (Fig. 29). In contrast, cells which overexpressed p63RhoGEF were slightly longer, but showed no differences in cell depth and width (Fig. 25). This demonstrates that p63RhoGEF has no dramatic effect on the AMCM size but might support their stabilization at least in culture.

However, one interesting morphological finding was the difference in the mean nucleus area. AMCM overexpressing the dominant negative p63ΔN constructs and cells with a full depletion

of p63RhoGEF showed a significantly smaller mean nucleus area than control-transduced and WT cells. (Fig. 27, Fig. 30, 31). This phenotype was also present in the intact myocardium (Fig. 31). In contrast, in TAC-AMCM the nuclei were significantly bigger than in sham cells (Fig. 37), but p63RhoGEF overexpression was not sufficient in increasing the size of the nuclei (Fig. 27). How the size of the nucleus is regulated in cardiomyocytes is not known. An increase in nuclear size had been described for example in tissues from patients with doxorubicin-induced cardiotoxicity [200]. In general it is thought that the nuclear and cell volume are related to each other and the size expansion of a nucleus is restricted [201]. Factors that might regulate the nuclear size are the DNA content [202] and extra-nuclear factors [203]. One hypothesis suggests that the membrane synthesis occurring in the ER membrane is the limiting factor for the nucleus growth [204] and that so called reticulon proteins might be involved in growth control [205]. An even open question is if a difference in nucleus size can influence cell behavior. In this context, at least a correlation between the nucleus size and transcriptional activity had been described [206]. Diseased cardiomyocytes resemble some of these proposed features. Growth in cell size is accompanied by an increase in nucleus size, and the transcriptional activity is clearly increased in the hypertrophic cardiomyocyte. Most interestingly, in a comparative study of 5 different cardiac hypertrophy mouse models, only 5 common genes were found to be dysregulated. Amongst these, was the upregulated reticulon 4 [207]. This, however, does not explain the smaller nuclei in the p63RhoGEF-KO model. Further studies are needed to unravel the mechanism and to characterize the consequences of this morphological abnormality.

Does p63RhoGEF have an influence on endomembrane systems in adult cardiomyocytes?

In all three model systems used in this thesis, changes in the endomembrane system were detected. Amongst these, the most conclusive was the change in the Golgi apparatus. An increase in p63RhoGEF, as obtained by adenoviral transduction and observed in TAC hearts, increased the number of GM-130-positive particles, whereas the knockout of p63RhoGEF decreased the number of particles (Fig. 24, Fig. 35, Fig. 36). Also, here it is not clear how p63RhoGEF could play a role in this scenario. The two likeliest explanations are: First, this regulation is RhoA-dependent. A link between RhoA and the Golgi regulation had been published several times [183, 208]. However, this would be a secondary and not a direct effect since active RhoA was not detected at the Golgi particles in AMCM under any condition, as it was demonstrated before by others [209]. Second, p63RhoGEF interferes with the described KDEL-receptor induced $G\alpha_{q/11}$ activation. It was shown that depletion of $G\alpha_{q/11}$ inhibited the

transport of cargo from the Golgi to the plasma membrane. As a consequence, the cargo got stuck in the Golgi apparatus. As a potential mechanism the KDEL receptor-induced, $G\alpha_{q/11}$-mediated activation of Src kinases was postulated [210]. How $G\alpha_{q/11}$ activates Src kinases was not further elucidated. Therefore, a remaining open question is if p63RhoGEF competes with this signaling as it competes with PLCβ.

6. Bibliography

1.   WHO, *http://www.who.int/mediacentre/factsheets/fs317/en/*. 2018.

2.   McMurray, J.J., et al., *ESC Guidelines for the diagnosis and treatment of acute and chronic heart failure 2012: The Task Force for the Diagnosis and Treatment of Acute and Chronic Heart Failure 2012 of the European Society of Cardiology. Developed in collaboration with the Heart Failure Association (HFA) of the ESC.* Eur Heart J, 2012. **33**(14): p. 1787-847.

3.   Ponikowski, P., et al., *2016 ESC Guidelines for the diagnosis and treatment of acute and chronic heart failure: The Task Force for the diagnosis and treatment of acute and chronic heart failure of the European Society of Cardiology (ESC). Developed with the special contribution of the Heart Failure Association (HFA) of the ESC.* Eur J Heart Fail, 2016. **18**(8): p. 891-975.

4.   Tham, Y.K., et al., *Pathophysiology of cardiac hypertrophy and heart failure: signaling pathways and novel therapeutic targets.* Arch Toxicol, 2015. **89**(9): p. 1401-38.

5.   *Guidelines for the diagnosis of heart failure. The Task Force on Heart Failure of the European Society of Cardiology.* Eur Heart J, 1995. **16**(6): p. 741-51.

6.   Cohn, J.N., et al., *Ejection fraction, peak exercise oxygen consumption, cardiothoracic ratio, ventricular arrhythmias, and plasma norepinephrine as determinants of prognosis in heart failure. The V-HeFT VA Cooperative Studies Group.* Circulation, 1993. **87**(6 Suppl): p. VI5-16.

7.   Cohn, J.N., R. Ferrari, and N. Sharpe, *Cardiac remodeling--concepts and clinical implications: a consensus paper from an international forum on cardiac remodeling. Behalf of an International Forum on Cardiac Remodeling.* J Am Coll Cardiol, 2000. **35**(3): p. 569-82.

8.   Grossman, W. and W.J. Paulus, *Myocardial stress and hypertrophy: a complex interface between biophysics and cardiac remodeling.* J Clin Invest, 2013. **123**(9): p. 3701-3.

9.   Kehat, I. and J.D. Molkentin, *Molecular pathways underlying cardiac remodeling during pathophysiological stimulation.* Circulation, 2010. **122**(25): p. 2727-35.

10.   Tan, L.B., et al., *Cardiac myocyte necrosis induced by angiotensin II.* Circ Res, 1991. **69**(5): p. 1185-95.

11.   Anderson, K.R., M.G. Sutton, and J.T. Lie, *Histopathological types of cardiac fibrosis in myocardial disease.* J Pathol, 1979. **128**(2): p. 79-85.

12.   Villarreal, F.J., et al., *Identification of functional angiotensin II receptors on rat cardiac fibroblasts.* Circulation, 1993. **88**(6): p. 2849-61.

13.   Teiger, E., et al., *Apoptosis in pressure overload-induced heart hypertrophy in the rat.* J Clin Invest, 1996. **97**(12): p. 2891-7.

14. Olivetti, G., et al., *Apoptosis in the failing human heart.* N Engl J Med, 1997. **336**(16): p. 1131-41.

15. Sharov, V.G., et al., *Evidence of cardiocyte apoptosis in myocardium of dogs with chronic heart failure.* Am J Pathol, 1996. **148**(1): p. 141-9.

16. Anversa, P., G. Olivetti, and J.M. Capasso, *Cellular basis of ventricular remodeling after myocardial infarction.* Am J Cardiol, 1991. **68**(14): p. 7D-16D.

17. Cleutjens, J.P., et al., *Regulation of collagen degradation in the rat myocardium after infarction.* J Mol Cell Cardiol, 1995. **27**(6): p. 1281-92.

18. McKay, R.G., et al., *Left ventricular remodeling after myocardial infarction: a corollary to infarct expansion.* Circulation, 1986. **74**(4): p. 693-702.

19. Nag, A.C., *Study of non-muscle cells of the adult mammalian heart: a fine structural analysis and distribution.* Cytobios, 1980. **28**(109): p. 41-61.

20. Zhou, P. and W.T. Pu, *Recounting Cardiac Cellular Composition.* Circ Res, 2016. **118**(3): p. 368-70.

21. Woodcock, E.A. and S.J. Matkovich, *Cardiomyocytes structure, function and associated pathologies.* Int J Biochem Cell Biol, 2005. **37**(9): p. 1746-51.

22. Pinto, A.R., et al., *Revisiting Cardiac Cellular Composition.* Circ Res, 2016. **118**(3): p. 400-9.

23. Stephen, M.J., et al., *Do binucleate cardiomyocytes have a role in myocardial repair? Insights using isolated rodent myocytes and cell culture.* Open Cardiovasc Med J, 2009. **3**: p. 1-7.

24. Piquereau, J., et al., *Mitochondrial dynamics in the adult cardiomyocytes: which roles for a highly specialized cell?* Front Physiol, 2013. **4**: p. 102.

25. Vendelin, M., et al., *Mitochondrial regular arrangement in muscle cells: a "crystal-like" pattern.* Am J Physiol Cell Physiol, 2005. **288**(3): p. C757-67.

26. Hayashi, T., et al., *Three-dimensional electron microscopy reveals new details of membrane systems for Ca2+ signaling in the heart.* J Cell Sci, 2009. **122**(Pt 7): p. 1005-13.

27. Soeller, C. and M.B. Cannell, *Examination of the transverse tubular system in living cardiac rat myocytes by 2-photon microscopy and digital image-processing techniques.* Circ Res, 1999. **84**(3): p. 266-75.

28. Song, L.S., et al., *Calcium biology of the transverse tubules in heart.* Ann N Y Acad Sci, 2005. **1047**: p. 99-111.

29. Wang, S.Q., et al., *Imaging microdomain Ca2+ in muscle cells.* Circ Res, 2004. **94**(8): p. 1011-22.

30.   Wehrens, X.H., et al., *FKBP12.6 deficiency and defective calcium release channel (ryanodine receptor) function linked to exercise-induced sudden cardiac death.* Cell, 2003. **113**(7): p. 829-40.

31.   Marks, A.R., S.O. Marx, and S. Reiken, *Regulation of ryanodine receptors via macromolecular complexes: a novel role for leucine/isoleucine zippers.* Trends Cardiovasc Med, 2002. **12**(4): p. 166-70.

32.   Marx, S.O., et al., *Requirement of a macromolecular signaling complex for beta adrenergic receptor modulation of the KCNQ1-KCNE1 potassium channel.* Science, 2002. **295**(5554): p. 496-9.

33.   Brette, F., L. Salle, and C.H. Orchard, *Differential modulation of L-type Ca2+ current by SR Ca2+ release at the T-tubules and surface membrane of rat ventricular myocytes.* Circ Res, 2004. **95**(1): p. e1-7.

34.   Lingwood, D., et al., *Lipid rafts as functional heterogeneity in cell membranes.* Biochem Soc Trans, 2009. **37**(Pt 5): p. 955-60.

35.   Simons, K. and E. Ikonen, *Functional rafts in cell membranes.* Nature, 1997. **387**(6633): p. 569-72.

36.   Palade, G.E. and R.R. Bruns, *Structural modulations of plasmalemmal vesicles.* J Cell Biol, 1968. **37**(3): p. 633-49.

37.   Parton, R.G. and K. Simons, *The multiple faces of caveolae.* Nat Rev Mol Cell Biol, 2007. **8**(3): p. 185-94.

38.   Scherer, P.E., et al., *Identification, sequence, and expression of caveolin-2 defines a caveolin gene family.* Proc Natl Acad Sci U S A, 1996. **93**(1): p. 131-5.

39.   Galbiati, F., et al., *Caveolin-3 null mice show a loss of caveolae, changes in the microdomain distribution of the dystrophin-glycoprotein complex, and t-tubule abnormalities.* J Biol Chem, 2001. **276**(24): p. 21425-33.

40.   Knowles, C.J., M. Cebova, and I.M. Pinz, *Palmitate diet-induced loss of cardiac caveolin-3: a novel mechanism for lipid-induced contractile dysfunction.* PLoS One, 2013. **8**(4): p. e61369.

41.   Robenek, H., G. Weissen-Plenz, and N.J. Severs, *Freeze-fracture replica immunolabelling reveals caveolin-1 in the human cardiomyocyte plasma membrane.* J Cell Mol Med, 2008. **12**(6A): p. 2519-21.

42.   Rybin, V.O., et al., *Caveolae-associated proteins in cardiomyocytes: caveolin-2 expression and interactions with caveolin-3.* Am J Physiol Heart Circ Physiol, 2003. **285**(1): p. H325-32.

43.   Bai, Y., et al., *Differential roles of caveolin-1 in ouabain-induced Na+/K+-ATPase cardiac signaling and contractility.* Physiol Genomics, 2016. **48**(10): p. 739-748.

44.   Balijepalli, R.C. and T.J. Kamp, *Caveolae, ion channels and cardiac arrhythmias.* Prog Biophys Mol Biol, 2008. **98**(2-3): p. 149-60.

45.   Eldstrom, J., et al., *Localization of Kv1.5 channels in rat and canine myocyte sarcolemma.* FEBS Lett, 2006. **580**(26): p. 6039-46.

46.   Patel, H.H., F. Murray, and P.A. Insel, *Caveolae as organizers of pharmacologically relevant signal transduction molecules.* Annu Rev Pharmacol Toxicol, 2008. **48**: p. 359-91.

47.   Steinberg, S.F., *beta(2)-Adrenergic receptor signaling complexes in cardiomyocyte caveolae/lipid rafts.* J Mol Cell Cardiol, 2004. **37**(2): p. 407-15.

48.   Balijepalli, R.C., et al., *Localization of cardiac L-type Ca(2+) channels to a caveolar macromolecular signaling complex is required for beta(2)-adrenergic regulation.* Proc Natl Acad Sci U S A, 2006. **103**(19): p. 7500-5.

49.   Kawamura, S., S. Miyamoto, and J.H. Brown, *Initiation and transduction of stretch-induced RhoA and Rac1 activation through caveolae: cytoskeletal regulation of ERK translocation.* J Biol Chem, 2003. **278**(33): p. 31111-7.

50.   Doroudgar, S. and C.C. Glembotski, *New concepts of endoplasmic reticulum function in the heart: programmed to conserve.* J Mol Cell Cardiol, 2013. **55**: p. 85-91.

51.   Yang, Z., et al., *The Golgi apparatus is a functionally distinct Ca2+ store regulated by the PKA and Epac branches of the beta1-adrenergic signaling pathway.* Sci Signal, 2015. **8**(398): p. ra101.

52.   Bers, D.M., *Cardiac excitation-contraction coupling.* Nature, 2002. **415**(6868): p. 198-205.

53.   Unudurthi, S.D., R.M. Wolf, and T.J. Hund, *Role of sinoatrial node architecture in maintaining a balanced source-sink relationship and synchronous cardiac pacemaking.* Front Physiol, 2014. **5**: p. 446.

54.   Louch, W.E., et al., *Reduced synchrony of Ca2+ release with loss of T-tubules-a comparison to Ca2+ release in human failing cardiomyocytes.* Cardiovasc Res, 2004. **62**(1): p. 63-73.

55.   Gordon, A.M., E. Homsher, and M. Regnier, *Regulation of contraction in striated muscle.* Physiol Rev, 2000. **80**(2): p. 853-924.

56.   Yang, Z., et al., *Na+-Ca2+ exchange activity is localized in the T-tubules of rat ventricular myocytes.* Circ Res, 2002. **91**(4): p. 315-22.

57.   Lyon, A.R., et al., *Loss of T-tubules and other changes to surface topography in ventricular myocytes from failing human and rat heart.* Proc Natl Acad Sci U S A, 2009. **106**(16): p. 6854-9.

58.   Heinzel, F.R., et al., *Remodeling of T-tubules and reduced synchrony of Ca2+ release in myocytes from chronically ischemic myocardium.* Circ Res, 2008. **102**(3): p. 338-46.

59.   Sipido, K.R., et al., *T-tubule remodelling and ryanodine receptor organization modulate sodium-calcium exchange.* Adv Exp Med Biol, 2013. **961**: p. 375-83.

60.   van Oort, R.J., et al., *Disrupted junctional membrane complexes and hyperactive ryanodine receptors after acute junctophilin knockdown in mice.* Circulation, 2011. **123**(9): p. 979-88.

61.   Wright, P.T., et al., *Caveolin-3 regulates compartmentation of cardiomyocyte beta2-adrenergic receptor-mediated cAMP signaling.* J Mol Cell Cardiol, 2014. **67**: p. 38-48.

62.   Prasad, K. and P.K. Singal, *Ultrastructure of failing myocardium due to induced chronic mitral insufficiency in dogs.* Br J Exp Pathol, 1977. **58**(3): p. 289-300.

63.   Tarazon, E., et al., *Changes in human Golgi apparatus reflect new left ventricular dimensions and function in dilated cardiomyopathy patients.* Eur J Heart Fail, 2017. **19**(2): p. 280-282.

64.   Hatt, P.Y., *Cellular changes and damage in mechanically overloaded hearts.* Recent Adv Stud Cardiac Struct Metab, 1975. **6**: p. 325-33.

65.   Tagawa, H., et al., *Cytoskeletal mechanics in pressure-overload cardiac hypertrophy.* Circ Res, 1997. **80**(2): p. 281-9.

66.   Heling, A., et al., *Increased expression of cytoskeletal, linkage, and extracellular proteins in failing human myocardium.* Circ Res, 2000. **86**(8): p. 846-53.

67.   Hopkins, A.L. and C.R. Groom, *The druggable genome.* Nat Rev Drug Discov, 2002. **1**(9): p. 727-30.

68.   Pierce, K.L., R.T. Premont, and R.J. Lefkowitz, *Seven-transmembrane receptors.* Nat Rev Mol Cell Biol, 2002. **3**(9): p. 639-50.

69.   Rosenbaum, D.M., S.G. Rasmussen, and B.K. Kobilka, *The structure and function of G-protein-coupled receptors.* Nature, 2009. **459**(7245): p. 356-63.

70.   Farrens, D.L., et al., *Requirement of rigid-body motion of transmembrane helices for light activation of rhodopsin.* Science, 1996. **274**(5288): p. 768-70.

71.   Shapiro, D.A., et al., *Evidence for a model of agonist-induced activation of 5-hydroxytryptamine 2A serotonin receptors that involves the disruption of a strong ionic interaction between helices 3 and 6.* J Biol Chem, 2002. **277**(13): p. 11441-9.

72.   Ballesteros, J.A., et al., *Activation of the beta 2-adrenergic receptor involves disruption of an ionic lock between the cytoplasmic ends of transmembrane segments 3 and 6.* J Biol Chem, 2001. **276**(31): p. 29171-7.

73.   Han, S.J., et al., *Identification of an agonist-induced conformational change occurring adjacent to the ligand-binding pocket of the M(3) muscarinic acetylcholine receptor.* J Biol Chem, 2005. **280**(41): p. 34849-58.

74.   Wess, J., *G-protein-coupled receptors: molecular mechanisms involved in receptor activation and selectivity of G-protein recognition.* FASEB J, 1997. **11**(5): p. 346-54.

75.   Neves, S.R., P.T. Ram, and R. Iyengar, *G protein pathways.* Science, 2002. **296**(5573): p. 1636-9.

76.   Rockman, H.A., W.J. Koch, and R.J. Lefkowitz, *Seven-transmembrane-spanning receptors and heart function.* Nature, 2002. **415**(6868): p. 206-12.

77.   Tang, C.M. and P.A. Insel, *GPCR expression in the heart; "new" receptors in myocytes and fibroblasts.* Trends Cardiovasc Med, 2004. **14**(3): p. 94-9.

78.   Hunt, S.A., et al., *ACC/AHA 2005 Guideline Update for the Diagnosis and Management of Chronic Heart Failure in the Adult: a report of the American College of Cardiology/American Heart Association Task Force on Practice Guidelines (Writing Committee to Update the 2001 Guidelines for the Evaluation and Management of Heart Failure): developed in collaboration with the American College of Chest Physicians and the International Society for Heart and Lung Transplantation: endorsed by the Heart Rhythm Society.* Circulation, 2005. **112**(12): p. e154-235.

79.   Kaumann, A.J. and P. Molenaar, *Modulation of human cardiac function through 4 beta-adrenoceptor populations.* Naunyn Schmiedebergs Arch Pharmacol, 1997. **355**(6): p. 667-81.

80.   Christ, T., et al., *Human atrial beta(1L)-adrenoceptor but not beta(3)-adrenoceptor activation increases force and Ca(2+) current at physiological temperature.* Br J Pharmacol, 2011. **162**(4): p. 823-39.

81.   Fajardo, G., et al., *Deletion of the beta2-adrenergic receptor prevents the development of cardiomyopathy in mice.* J Mol Cell Cardiol, 2013. **63**: p. 155-64.

82.   Bristow, M.R., et al., *Beta 1- and beta 2-adrenergic receptor-mediated adenylate cyclase stimulation in nonfailing and failing human ventricular myocardium.* Mol Pharmacol, 1989. **35**(3): p. 295-303.

83.   Xiang, Y. and B.K. Kobilka, *Myocyte adrenoceptor signaling pathways.* Science, 2003. **300**(5625): p. 1530-2.

84.   Salazar, N.C., J. Chen, and H.A. Rockman, *Cardiac GPCRs: GPCR signaling in healthy and failing hearts.* Biochim Biophys Acta, 2007. **1768**(4): p. 1006-18.

85.   Gauthier, C., et al., *Functional beta3-adrenoceptor in the human heart.* J Clin Invest, 1996. **98**(2): p. 556-62.

86.   Kohout, T.A., et al., *Augmentation of cardiac contractility mediated by the human beta(3)-adrenergic receptor overexpressed in the hearts of transgenic mice.* Circulation, 2001. **104**(20): p. 2485-91.

87.   Nikolaev, V.O., et al., *Beta2-adrenergic receptor redistribution in heart failure changes cAMP compartmentation.* Science, 2010. **327**(5973): p. 1653-7.

88.   De Mello, W.C. and A.H. Danser, *Angiotensin II and the heart : on the intracrine renin-angiotensin system.* Hypertension, 2000. **35**(6): p. 1183-8.

89.   Touyz, R.M. and E.L. Schiffrin, *Signal transduction mechanisms mediating the physiological and pathophysiological actions of angiotensin II in vascular smooth muscle cells.* Pharmacol Rev, 2000. **52**(4): p. 639-72.

90. Simpson, P.C., et al., *Adrenergic hormones and control of cardiac myocyte growth.* Mol Cell Biochem, 1991. **104**(1-2): p. 35-43.

91. Hubbard, K.B. and J.R. Hepler, *Cell signalling diversity of the Gqalpha family of heterotrimeric G proteins.* Cell Signal, 2006. **18**(2): p. 135-50.

92. Meggs, L.G., et al., *Regulation of angiotensin II receptors on ventricular myocytes after myocardial infarction in rats.* Circ Res, 1993. **72**(6): p. 1149-62.

93. Suzuki, J., et al., *Rat angiotensin II (type 1A) receptor mRNA regulation and subtype expression in myocardial growth and hypertrophy.* Circ Res, 1993. **73**(3): p. 439-47.

94. Lambert, C., Y. Massillon, and S. Meloche, *Upregulation of cardiac angiotensin II AT1 receptors in congenital cardiomyopathic hamsters.* Circ Res, 1995. **77**(5): p. 1001-7.

95. Rogg, H., et al., *Angiotensin II-receptor subtypes in human atria and evidence for alterations in patients with cardiac dysfunction.* Eur Heart J, 1996. **17**(7): p. 1112-20.

96. Regitz-Zagrosek, V., et al., *Regulation, chamber localization, and subtype distribution of angiotensin II receptors in human hearts.* Circulation, 1995. **91**(5): p. 1461-71.

97. Wennerberg, K., K.L. Rossman, and C.J. Der, *The Ras superfamily at a glance.* J Cell Sci, 2005. **118**(Pt 5): p. 843-6.

98. Bourne, H.R., D.A. Sanders, and F. McCormick, *The GTPase superfamily: conserved structure and molecular mechanism.* Nature, 1991. **349**(6305): p. 117-27.

99. Haga, R.B. and A.J. Ridley, *Rho GTPases: Regulation and roles in cancer cell biology.* Small GTPases, 2016. **7**(4): p. 207-221.

100. Jaffe, A.B. and A. Hall, *Rho GTPases: biochemistry and biology.* Annu Rev Cell Dev Biol, 2005. **21**: p. 247-69.

101. Kjoller, L. and A. Hall, *Signaling to Rho GTPases.* Exp Cell Res, 1999. **253**(1): p. 166-79.

102. Sah, V.P., et al., *The role of Rho in G protein-coupled receptor signal transduction.* Annu Rev Pharmacol Toxicol, 2000. **40**: p. 459-89.

103. Van Aelst, L. and C. D'Souza-Schorey, *Rho GTPases and signaling networks.* Genes Dev, 1997. **11**(18): p. 2295-322.

104. Fukumoto, Y., et al., *Molecular cloning and characterization of a novel type of regulatory protein (GDI) for the rho proteins, ras p21-like small GTP-binding proteins.* Oncogene, 1990. **5**(9): p. 1321-8.

105. Isomura, M., et al., *Regulation of binding of rhoB p20 to membranes by its specific regulatory protein, GDP dissociation inhibitor.* Oncogene, 1991. **6**(1): p. 119-24.

106. Ridley, A.J. and A. Hall, *The small GTP-binding protein rho regulates the assembly of focal adhesions and actin stress fibers in response to growth factors.* Cell, 1992. **70**(3): p. 389-99.

107. Kristelly, R., G. Gao, and J.J. Tesmer, *Structural determinants of RhoA binding and nucleotide exchange in leukemia-associated Rho guanine-nucleotide exchange factor.* J Biol Chem, 2004. **279**(45): p. 47352-62.

108. Allal, C., et al., *RhoA prenylation is required for promotion of cell growth and transformation and cytoskeleton organization but not for induction of serum response element transcription.* J Biol Chem, 2000. **275**(40): p. 31001-8.

109. Hodge, R.G. and A.J. Ridley, *Regulating Rho GTPases and their regulators.* Nat Rev Mol Cell Biol, 2016. **17**(8): p. 496-510.

110. Backlund, P.S., Jr., *Post-translational processing of RhoA. Carboxyl methylation of the carboxyl-terminal prenylcysteine increases the half-life of Rhoa.* J Biol Chem, 1997. **272**(52): p. 33175-80.

111. Michaelson, D., et al., *Differential localization of Rho GTPases in live cells: regulation by hypervariable regions and RhoGDI binding.* J Cell Biol, 2001. **152**(1): p. 111-26.

112. Forget, M.A., et al., *Phosphorylation states of Cdc42 and RhoA regulate their interactions with Rho GDP dissociation inhibitor and their extraction from biological membranes.* Biochem J, 2002. **361**(Pt 2): p. 243-54.

113. Lang, P., et al., *Protein kinase A phosphorylation of RhoA mediates the morphological and functional effects of cyclic AMP in cytotoxic lymphocytes.* EMBO J, 1996. **15**(3): p. 510-9.

114. Takefuji, M., et al., *RhoGEF12 controls cardiac remodeling by integrating G protein- and integrin-dependent signaling cascades.* J Exp Med, 2013. **210**(4): p. 665-73.

115. Porchia, F., et al., *Endothelin-1 up-regulates p115RhoGEF in embryonic rat cardiomyocytes during the hypertrophic response.* J Recept Signal Transduct Res, 2008. **28**(3): p. 265-83.

116. Lutz, S., et al., *Structure of Galphaq-p63RhoGEF-RhoA complex reveals a pathway for the activation of RhoA by GPCRs.* Science, 2007. **318**(5858): p. 1923-7.

117. Aoki, H., S. Izumo, and J. Sadoshima, *Angiotensin II activates RhoA in cardiac myocytes: a critical role of RhoA in angiotensin II-induced premyofibril formation.* Circ Res, 1998. **82**(6): p. 666-76.

118. Sah, V.P., et al., *Rho is required for Galphaq and alpha1-adrenergic receptor signaling in cardiomyocytes. Dissociation of Ras and Rho pathways.* J Biol Chem, 1996. **271**(49): p. 31185-90.

119. Clerk, A., et al., *Regulation of mitogen-activated protein kinases in cardiac myocytes through the small G protein Rac1.* Mol Cell Biol, 2001. **21**(4): p. 1173-84.

120. Del Re, D.P., S. Miyamoto, and J.H. Brown, *RhoA/Rho kinase up-regulate Bax to activate a mitochondrial death pathway and induce cardiomyocyte apoptosis.* J Biol Chem, 2007. **282**(11): p. 8069-78.

121. Del Re, D.P., S. Miyamoto, and J.H. Brown, *Focal Adhesion Kinase as a RhoA-activable Signaling Scaffold Mediating Akt Activation and Cardiomyocyte Protection.* Journal of Biological Chemistry, 2008. **283**(51): p. 35622-35629.

122. Sah, V.P., et al., *Cardiac-specific overexpression of RhoA results in sinus and atrioventricular nodal dysfunction and contractile failure.* J Clin Invest, 1999. **103**(12): p. 1627-34.

123. Xiang, S.Y., et al., *RhoA protects the mouse heart against ischemia/reperfusion injury.* J Clin Invest, 2011. **121**(8): p. 3269-76.

124. Lauriol, J., et al., *RhoA signaling in cardiomyocytes protects against stress-induced heart failure but facilitates cardiac fibrosis.* Sci Signal, 2014. **7**(348): p. ra100.

125. Dong, M., et al., *Increased Rho kinase activity in congestive heart failure.* Eur J Heart Fail, 2012. **14**(9): p. 965-73.

126. Meller, N., S. Merlot, and C. Guda, *CZH proteins: a new family of Rho-GEFs.* J Cell Sci, 2005. **118**(Pt 21): p. 4937-46.

127. Fort, P. and A. Blangy, *The Evolutionary Landscape of Dbl-Like RhoGEF Families: Adapting Eukaryotic Cells to Environmental Signals.* Genome Biol Evol, 2017. **9**(6): p. 1471-1486.

128. Eva, A. and S.A. Aaronson, *Isolation of a new human oncogene from a diffuse B-cell lymphoma.* Nature, 1985. **316**(6025): p. 273-5.

129. Hart, M.J., et al., *Catalysis of guanine nucleotide exchange on the CDC42Hs protein by the dbl oncogene product.* Nature, 1991. **354**(6351): p. 311-4.

130. Hart, M.J., et al., *Cellular transformation and guanine nucleotide exchange activity are catalyzed by a common domain on the dbl oncogene product.* J Biol Chem, 1994. **269**(1): p. 62-5.

131. Lai, C.C., et al., *Influence of guanine nucleotides on complex formation between Ras and CDC25 proteins.* Mol Cell Biol, 1993. **13**(3): p. 1345-52.

132. Karnoub, A.E., et al., *Molecular basis for Rac1 recognition by guanine nucleotide exchange factors.* Nat Struct Biol, 2001. **8**(12): p. 1037-41.

133. Snyder, J.T., et al., *Structural basis for the selective activation of Rho GTPases by Dbl exchange factors.* Nat Struct Biol, 2002. **9**(6): p. 468-75.

134. Mayer, B.J., et al., *A putative modular domain present in diverse signaling proteins.* Cell, 1993. **73**(4): p. 629-30.

135. Liu, X., et al., *NMR structure and mutagenesis of the N-terminal Dbl homology domain of the nucleotide exchange factor Trio.* Cell, 1998. **95**(2): p. 269-77.

136. Aittaleb, M., et al., *Plasma membrane association of p63 Rho guanine nucleotide exchange factor (p63RhoGEF) is mediated by palmitoylation and is required for basal activity in cells.* J Biol Chem, 2011. **286**(39): p. 34448-56.

137. Shankaranarayanan, A., et al., *Galpha q allosterically activates and relieves autoinhibition of p63RhoGEF.* Cell Signal, 2010. **22**(7): p. 1114-23.

138. Snyder, J.T., et al., *Quantitative analysis of the effect of phosphoinositide interactions on the function of Dbl family proteins.* J Biol Chem, 2001. **276**(49): p. 45868-75.

139. Souchet, M., et al., *Human p63RhoGEF, a novel RhoA-specific guanine nucleotide exchange factor, is localized in cardiac sarcomere.* J Cell Sci, 2001. **115**(Pt 3): p. 629-40.

140. Bryan, B., et al., *GEFT, a Rho family guanine nucleotide exchange factor, regulates neurite outgrowth and dendritic spine formation.* J Biol Chem, 2004. **279**(44): p. 45824-32.

141. Lutz, S., et al., *p63RhoGEF and GEFT are Rho-specific guanine nucleotide exchange factors encoded by the same gene.* Naunyn Schmiedebergs Arch Pharmacol, 2004. **369**(5): p. 540-6.

142. Smith, T.K., et al., *Bves directly interacts with GEFT, and controls cell shape and movement through regulation of Rac1/Cdc42 activity.* Proc Natl Acad Sci U S A, 2008. **105**(24): p. 8298-303.

143. van Unen, J., et al., *Kinetics of recruitment and allosteric activation of ARHGEF25 isoforms by the heterotrimeric G-protein Galphaq.* Sci Rep, 2016. **6**: p. 36825.

144. Guo, X., et al., *A Rac/Cdc42-specific exchange factor, GEFT, induces cell proliferation, transformation, and migration.* J Biol Chem, 2003. **278**(15): p. 13207-15.

145. Rojas, R.J., et al., *Galphaq directly activates p63RhoGEF and Trio via a conserved extension of the Dbl homology-associated pleckstrin homology domain.* J Biol Chem, 2007. **282**(40): p. 29201-10.

146. Goedhart, J., et al., *Signaling efficiency of Galphaq through its effectors p63RhoGEF and GEFT depends on their subcellular location.* Sci Rep, 2013. **3**: p. 2284.

147. Hayashi, A., et al., *p63RhoGEF-mediated formation of a single polarized lamellipodium is required for chemotactic migration in breast carcinoma cells.* FEBS Lett, 2013. **587**(6): p. 698-705.

148. Siegert, P., et al., *Pasteurella multocida toxin prevents osteoblast differentiation by transactivation of the MAP-kinase cascade via the Galpha(q/11)--p63RhoGEF--RhoA axis.* PLoS Pathog, 2013. **9**(5): p. e1003385.

149. Momotani, K., et al., *p63RhoGEF couples Galpha(q/11)-mediated signaling to Ca2+ sensitization of vascular smooth muscle contractility.* Circ Res, 2011. **109**(9): p. 993-1002.

150. Wuertz, C.M., et al., *p63RhoGEF--a key mediator of angiotensin II-dependent signaling and processes in vascular smooth muscle cells.* FASEB J, 2010. **24**(12): p. 4865-76.

151. Ongherth, A., et al., *p63RhoGEF regulates auto- and paracrine signaling in cardiac fibroblasts.* J Mol Cell Cardiol, 2015. **88**: p. 39-54.

152. Calo, L.A., et al., *Increased level of p63RhoGEF and RhoA/Rho kinase activity in hypertensive patients.* J Hypertens, 2014. **32**(2): p. 331-8.

153. Ravarotto, V., et al., *The blocking of angiotensin II type 1 receptor and RhoA/Rho kinase activity in hypertensive patients: Effect of olmesartan medoxomil and implication with cardiovascular-renal remodeling.* J Renin Angiotensin Aldosterone Syst, 2015. **16**(4): p. 1245-50.

154. Lutz, S., et al., *The guanine nucleotide exchange factor p63RhoGEF, a specific link between Gq/11-coupled receptor signaling and RhoA.* J Biol Chem, 2005. **280**(12): p. 11134-9.

155. Borner, S., et al., *FRET measurements of intracellular cAMP concentrations and cAMP analog permeability in intact cells.* Nat Protoc, 2011. **6**(4): p. 427-38.

156. Pasqualin, C., et al., *Automatic quantitative analysis of t-tubule organization in cardiac myocytes using ImageJ.* Am J Physiol Cell Physiol, 2015. **308**(3): p. C237-45.

157. Luo, T., B. Chen, and X. Wang, *4-PBA prevents pressure overload-induced myocardial hypertrophy and interstitial fibrosis by attenuating endoplasmic reticulum stress.* Chem Biol Interact, 2015. **242**: p. 99-106.

158. Rumyantsev, P.P. and B.M. Carlson, *Growth and Hyperplasia of Cardiac Muscle Cells.* 1991: Harwood Academic Publishers.

159. Kimura, K., et al., *Regulation of myosin phosphatase by Rho and Rho-associated kinase (Rho-kinase).* Science, 1996. **273**(5272): p. 245-8.

160. Sakurada, S., et al., *Rho activation in excitatory agonist-stimulated vascular smooth muscle.* Am J Physiol Cell Physiol, 2001. **281**(2): p. C571-8.

161. Ocana-Morgner, C., C. Wahren, and R. Jessberger, *SWAP-70 regulates RhoA/RhoB-dependent MHCII surface localization in dendritic cells.* Blood, 2009. **113**(7): p. 1474-82.

162. King, J.R. and N. Kabbani, *Alpha 7 nicotinic receptor coupling to heterotrimeric G proteins modulates RhoA activation, cytoskeletal motility, and structural growth.* J Neurochem, 2016. **138**(4): p. 532-45.

163. Kuipers, D., et al., *Epithelial repair is a two-stage process driven first by dying cells and then by their neighbours.* J Cell Sci, 2014. **127**(Pt 6): p. 1229-41.

164. Bokoch, G.M., B.P. Bohl, and T.H. Chuang, *Guanine nucleotide exchange regulates membrane translocation of Rac/Rho GTP-binding proteins.* J Biol Chem, 1994. **269**(50): p. 31674-9.

165. van Unen, J., et al., *Plasma membrane restricted RhoGEF activity is sufficient for RhoA-mediated actin polymerization.* Sci Rep, 2015. **5**: p. 14693.

166. Szulcek, R., et al., *Localized RhoA GTPase activity regulates dynamics of endothelial monolayer integrity.* Cardiovasc Res, 2013. **99**(3): p. 471-82.

167. Bourmeyster, N., P. Boquet, and P.V. Vignais, *Role of bound GDP in the stability of the rho A-rho GDI complex purified from neutrophil cytosol.* Biochem Biophys Res Commun, 1994. **205**(1): p. 174-9.

168. Rosenkranz, S., *TGF-beta1 and angiotensin networking in cardiac remodeling.* Cardiovasc Res, 2004. **63**(3): p. 423-32.

169. O'Connell, T.D., et al., *Cardiac alpha1-adrenergic receptors: novel aspects of expression, signaling mechanisms, physiologic function, and clinical importance.* Pharmacol Rev, 2014. **66**(1): p. 308-33.

170. Mulder, P., V. Richard, and C. Thuillez, *Endothelin antagonism in experimental ischemic heart failure: hemodynamic, structural and neurohumoral effects.* Heart Fail Rev, 2001. **6**(4): p. 295-300.

171. Snabaitis, A.K., et al., *Regulation of the extracellular signal-regulated kinase pathway in adult myocardium: differential roles of G(q/11), Gi and G(12/13) proteins in signalling by alpha1-adrenergic, endothelin-1 and thrombin-sensitive protease-activated receptors.* Cell Signal, 2005. **17**(5): p. 655-64.

172. Markou, T. and A. Lazou, *Phosphorylation and activation of mitogen- and stress-activated protein kinase-1 in adult rat cardiac myocytes by G-protein-coupled receptor agonists requires both extracellular-signal-regulated kinase and p38 mitogen-activated protein kinase.* Biochem J, 2002. **365**(Pt 3): p. 757-63.

173. Samarel, A.M., *Costameres, focal adhesions, and cardiomyocyte mechanotransduction.* Am J Physiol Heart Circ Physiol, 2005. **289**(6): p. H2291-301.

174. Anastasi, G., et al., *Dystrophin-glycoprotein complex and vinculin-talin-integrin system in human adult cardiac muscle.* Int J Mol Med, 2009. **23**(2): p. 149-59.

175. Pardo, J.V., J.D. Siliciano, and S.W. Craig, *Vinculin is a component of an extensive network of myofibril-sarcolemma attachment regions in cardiac muscle fibers.* J Cell Biol, 1983. **97**(4): p. 1081-8.

176. Balycheva, M., et al., *Microdomain-specific localization of functional ion channels in cardiomyocytes: an emerging concept of local regulation and remodelling.* Biophys Rev, 2015. **7**(1): p. 43-62.

177. Zeidan, A., et al., *Leptin-induced cardiomyocyte hypertrophy involves selective caveolae and RhoA/ROCK-dependent p38 MAPK translocation to nuclei.* Cardiovasc Res, 2008. **77**(1): p. 64-72.

178. Savinova, O.V. and A.M. Gerdes, *Myocyte changes in heart failure.* Heart Fail Clin, 2012. **8**(1): p. 1-6.

179. Sprenger, J.U., et al., *In vivo model with targeted cAMP biosensor reveals changes in receptor-microdomain communication in cardiac disease.* Nat Commun, 2015. **6**: p. 6965.

180. Kaprielian, R.R., et al., *Distinct patterns of dystrophin organization in myocyte sarcolemma and transverse tubules of normal and diseased human myocardium.* Circulation, 2000. **101**(22): p. 2586-94.

181.   Zou, C., et al., *Simvastatin activates the PPARgamma-dependent pathway to prevent left ventricular hypertrophy associated with inhibition of RhoA signaling.* Tex Heart Inst J, 2013. **40**(2): p. 140-7.

182.   Ikeda, S., et al., *Crucial role of rho-kinase in pressure overload-induced right ventricular hypertrophy and dysfunction in mice.* Arterioscler Thromb Vasc Biol, 2014. **34**(6): p. 1260-71.

183.   Jatho, A., et al., *RhoA Ambivalently Controls Prominent Myofibroblast Characteritics by Involving Distinct Signaling Routes.* PLoS One, 2015. **10**(10): p. e0137519.

184.   Van Heugten, H.A., et al., *Homologous desensitization of the endothelin-1 receptor mediated phosphoinositide response in cultured neonatal rat cardiomyocytes.* J Mol Cell Cardiol, 1993. **25**(1): p. 41-52.

185.   Zhang, M., et al., *Protein kinase C modulation of cardiomyocyte angiotensin II and vasopressin receptor desensitization.* Hypertension, 1996. **27**(2): p. 269-75.

186.   Zhao, M., H.K. Hagler, and K.H. Muntz, *Regulation of alpha 1-, beta 1-, and beta 2-adrenergic receptors in rat heart by norepinephrine.* Am J Physiol, 1996. **271**(5 Pt 2): p. H1762-8.

187.   Souchet, M., et al., *Human p63RhoGEF, a novel RhoA-specific guanine nucleotide exchange factor, is localized in cardiac sarcomere.* J Cell Sci, 2002. **115**(Pt 3): p. 629-40.

188.   Salaun, C., J. Greaves, and L.H. Chamberlain, *The intracellular dynamic of protein palmitoylation.* J Cell Biol, 2010. **191**(7): p. 1229-38.

189.   Frank, D., et al., *Mice with cardiac-restricted overexpression of Myozap are sensitized to biomechanical stress and develop a protein-aggregate-associated cardiomyopathy.* J Mol Cell Cardiol, 2014. **72**: p. 196-207.

190.   Seeger, T.S., et al., *Myozap, a novel intercalated disc protein, activates serum response factor-dependent signaling and is required to maintain cardiac function in vivo.* Circ Res, 2010. **106**(5): p. 880-90.

191.   Levental, I., et al., *Palmitoylation regulates raft affinity for the majority of integral raft proteins.* Proc Natl Acad Sci U S A, 2010. **107**(51): p. 22050-4.

192.   Lewis, M.J. and H.R. Pelham, *Sequence of a second human KDEL receptor.* J Mol Biol, 1992. **226**(4): p. 913-6.

193.   Peter, F., P. Nguyen Van, and H.D. Soling, *Different sorting of Lys-Asp-Glu-Leu proteins in rat liver.* J Biol Chem, 1992. **267**(15): p. 10631-7.

194.   Scheel, A.A. and H.R. Pelham, *Identification of amino acids in the binding pocket of the human KDEL receptor.* J Biol Chem, 1998. **273**(4): p. 2467-72.

195.   Pulvirenti, T., et al., *A traffic-activated Golgi-based signalling circuit coordinates the secretory pathway.* Nat Cell Biol, 2008. **10**(8): p. 912-22.

196. Roti, E.C., et al., *Interaction with GM130 during HERG ion channel trafficking. Disruption by type 2 congenital long QT syndrome mutations. Human Ether-a-go-go-Related Gene.* J Biol Chem, 2002. **277**(49): p. 47779-85.

197. Ralston, E., Z. Lu, and T. Ploug, *The organization of the Golgi complex and microtubules in skeletal muscle is fiber type-dependent.* J Neurosci, 1999. **19**(24): p. 10694-705.

198. Lyon, A.M., V.G. Taylor, and J.J. Tesmer, *Strike a pose: Galphaq complexes at the membrane.* Trends Pharmacol Sci, 2014. **35**(1): p. 23-30.

199. Hahn, H.S., et al., *Protein kinase Calpha negatively regulates systolic and diastolic function in pathological hypertrophy.* Circ Res, 2003. **93**(11): p. 1111-9.

200. Unverferth, B.J., et al., *Differentiating characteristics of myocardial nuclei in cardiomyopathy.* Hum Pathol, 1983. **14**(11): p. 974-83.

201. Gregory, T., *Genome size evolution in animals. InThe Evolution of the Genome* Vol. 1. 2005, Elsevier Academic Press.

202. Henery, C.C. and M.H. Kaufman, *Relationship between cell size and nuclear volume in nucleated red blood cells of developmentally matched diploid and tetraploid mouse embryos.* J Exp Zool, 1992. **261**(4): p. 472-8.

203. Neumann, F.R. and P. Nurse, *Nuclear size control in fission yeast.* J Cell Biol, 2007. **179**(4): p. 593-600.

204. Anderson, D.J. and M.W. Hetzer, *Nuclear envelope formation by chromatin-mediated reorganization of the endoplasmic reticulum.* Nat Cell Biol, 2007. **9**(10): p. 1160-6.

205. Anderson, D.J. and M.W. Hetzer, *Reshaping of the endoplasmic reticulum limits the rate for nuclear envelope formation.* J Cell Biol, 2008. **182**(5): p. 911-24.

206. Schmidt, E.E. and U. Schibler, *Cell size regulation, a mechanism that controls cellular RNA accumulation: consequences on regulation of the ubiquitous transcription factors Oct1 and NF-Y and the liver-enriched transcription factor DBP.* J Cell Biol, 1995. **128**(4): p. 467-83.

207. Sasagawa, S., et al., *Downregulation of GSTK1 Is a Common Mechanism Underlying Hypertrophic Cardiomyopathy.* Front Pharmacol, 2016. **7**: p. 162.

208. Zilberman, Y., et al., *Involvement of the Rho-mDia1 pathway in the regulation of Golgi complex architecture and dynamics.* Mol Biol Cell, 2011. **22**(16): p. 2900-11.

209. Matas, O.B., et al., *Membrane trafficking at the ER/Golgi interface: functional implications of RhoA and Rac1.* Eur J Cell Biol, 2005. **84**(8): p. 699-707.

210. Giannotta, M., et al., *The KDEL receptor couples to Galphaq/11 to activate Src kinases and regulate transport through the Golgi.* EMBO J, 2012. **31**(13): p. 2869-81.

7. Own publication

Ongherth, A., S. Pasch, C. M. Wuertz, K. Nowak, N. Kittana, C. A. Weis, A. Jatho, C. Vettel, M.Tiburcy, K. Toischer, G. Hasenfuss, W. H. Zimmermann, T. Wieland and S. Lutz (2015). "p63RhoGEF regulates auto- and paracrine signaling in cardiac fibroblasts." <u>J Mol Cell Cardiol</u> **88**: 39-54.